Three-node flat shell finite elements based on the cubic linked interpolation and the assumed strain method

Grbac, Marin

Doctoral thesis / Disertacija

2022

Degree Grantor / Ustanova koja je dodijelila akademski / stručni stupanj: **University of Rijeka, Faculty of Civil Engineering / Sveučilište u Rijeci, Građevinski fakultet**

Permanent link / Trajna poveznica: https://urn.nsk.hr/urn:nbn:hr:157:354050

UNIVERSITY OF RIJEKA

FACULTY OF CIVIL ENGINEERING

Marin Grbac

THREE-NODE FLAT SHELL FINITE ELEMENTS BASED ON THE CUBIC LINKED INTERPOLATION AND THE ASSUMED STRAIN METHOD

DOCTORAL THESIS

Rijeka, 2022

UNIVERSITY OF RIJEKA

FACULTY OF CIVIL ENGINEERING

Marin Grbac

THREE-NODE FLAT SHELL FINITE ELEMENTS BASED ON THE CUBIC LINKED INTERPOLATION AND THE ASSUMED STRAIN METHOD

DOCTORAL THESIS

Supervisor: Assoc. Prof. Dragan Ribarić, PhD

Rijeka, 2022

Mentor rada: Izv. prof. dr. sc. Dragan Ribarić

Doktorski rad obranjen je dana 20.10.2022. na Građevinskom fakultetu Sveučilišta u Rijeci, pred povjerenstvom u sastavu:

1. Prof. dr. sc. Gordan Jelenić, Sveučilište u Rijeci, Građevinski fakultet, predsjednik
2. Izv. prof. dr. sc. Leo Škec, Sveučilište u Rijeci, Građevinski fakultet, član
3. Prof. dr. sc. Boštjan Brank, Univerza v Ljubljani, Fakulteta za gradbeništvo in geodezijo, vanjski član

"What we know is a drop, what we don't know is an ocean."

Isaac Newton

Acknowledgements

The findings presented in this thesis is the result of work within the research project IP-06-2016-4775: "Assumed Strain Method in Finite Elements for Layered Plates and Shells with Application on Layer Delamination Problem", in addition to the "Young Researchers' Career Development Project – Training New Doctoral Students" grant, both financially supported by the Croatian Science Foundation.

This thesis would not be feasible without these grants; hence, they are very much gratefully acknowledged.

I am also immensely grateful to all the faculty staff who contributed to the completion of my doctoral journey, especially to my supervisor Dragan, for his generous, pragmatic and composed demeanour.

Finally, I am truly thankful to my family and friends for sharing this odyssey with me, primarily Laura, for being there, always.

I dedicate this thesis to scientific curiosity;

one of the greatest traits of humankind.

Abstract

In this doctoral thesis, new three-node flat shell finite elements for general 3D linear-elastic analysis of shells with small deformations are developed. These flat shell finite elements are formed by joining two independent parts: out-of-plane Mindlin plate bending part and in-plane membrane part. The displacement-based approach with linked interpolation and the assumed strain method are employed for the development of new finite elements. Various effective finite elements have been developed in the process.

Mindlin plate bending finite elements presented here are based on the two-node Timoshenko beam finite element with problem-dependent cubic linked interpolation. This beam element is free of shear locking and is capable of returning the exact results for certain load cases, and has been successfully utilised for Mindlin plate elements in the literature. Without any additional treatment, plate elements developed in such way may still suffer from shear locking in thin limit cases. This locking is avoided here by following the assumed strain method.

Membrane finite elements presented here are utilising rotational (drilling) degrees of freedom which are linked to the displacement fields. Physically correct implementation of the rotational degrees of freedom is achieved by satisfying the classical theory of elasticity definition of rotation. This approach is particularly convenient when used for the in-plane membrane part in the shell finite element formulation.

All finite elements have been subjected to the so-called patch tests and tested on a variety of standard numerical examples, as well as compared with the finite elements used in the Finite Element Analysis Program (FEAP), in addition to other known finite elements from the literature.

Keywords: finite element method, flat shell finite elements, Mindlin plate elements, membrane elements with rotational degrees of freedom, linked interpolation, assumed strain method

Sažetak

U ovoj doktorskoj disertaciji razvijeni su novi tročvorni konačni elementi ravnih ljuski za opću 3D linearno-elastičnu analizu ljuski s malim deformacijama. Ovi konačni elementi ravnih ljuski formiraju se spajanjem dvaju neovisnih dijela: dijela od savijanja ploča Mindlinovog tipa (izvan ravnine) i membranskog dijela (unutar ravnine). Za razvoj novih konačnih elemenata korišten je pristup koji se temelji na pomacima uz primjenu vezane interpolacije te metoda usvojenih deformacija. U tom procesu razvijeni su razni učinkoviti konačni elementi.

Ovdje predstavljeni konačni elementi Mindlinovih ploča temelje se na dvočvornom Timošenkovom grednom konačnom elementu s kubnom vezanom interpolacijom koja je ovisna o problemu. Ovaj gredni element je slobodan od *shear locking*-a i sposoban je dati točne rezultate za određene slučajeve opterećenja, a uspješno je korišten za elemente Mindlinovih ploča u literaturi. Bez ikakvog dodatnog tretmana, tako razvijeni elementi ploča mogu i dalje patiti od *shear locking*-a u graničnim slučajevima tankih ploča. Ovdje se taj *locking* izbjegava slijedeći metodu usvojenih deformacija.

Ovdje predstavljeni membranski konačni elementi koriste rotacijske stupnjeve slobode koji su povezani s poljima pomaka. Fizički ispravna implementacija rotacijskih stupnjeva slobode postiže se zadovoljavanjem definicije rotacije prema klasičnoj teoriji elastičnosti. Ovaj pristup je osobito prikladan kada se koristi za membranski dio (unutar ravnine) u formulaciji konačnog elementa ljuske.

Svi konačni elementi podvrgnuti su takozvanim *patch test*-ovima i testirani su na raznim standardnim numeričkim primjerima, kao i uspoređeni s konačnim elementima koji se koriste u *Finite Element Analysis Program (FEAP)*-u, uz ostale poznate konačne elemente iz literature.

Ključne riječi: metoda konačnih elemenata, konačni elementi ravnih ljuski, Mindlinovi elementi ploča, membranski elementi s rotacijskim stupnjevima slobode, vezana interpolacija, metoda usvojenih deformacija

Contents

Chapter 1

Introduction

Plates, shells and membranes are load-bearing structural elements whose one dimension (thickness) is much smaller compared to the other two dimensions. Plates are flat and they primarily carry forces and moments acting normal to its middle surface, while shells are generally curved in shape and they carry forces and moments acting both normal and tangential to its middle surface. Plates can be regarded as a special case of flat shells in which in-plane forces and moments are usually very small, and are therefore neglected, as is the in-plane stiffness for that matter. Additionally, membranes can be regarded as shells with no out-of-plane stiffness. In engineering practice, membranes are usually considered as thin structural elements designed specifically to carry in-plane forces only.

Since the thickness is much smaller than the other two dimensions, plates, shells and membranes do not need to be analysed as 3D bodies, moreover, that would be quite impractical. In order to rationalise non 3D analyses, various theories have been developed in which governing differential equations are formulated with respect to the middle surface of these elements. Solutions of those governing differential equations can only be obtained for a limited number of boundary and load conditions. Hence, numerous practical problems cannot be solved by classical methods as they generally do not provide a solution, unlike numerical methods.

Today, with the wide availability of computers and their ever increasing computational power, numerical methods are of significant importance as they represent a powerful tool for solving many different problems in areas of mathematics. One numerical method in particular, which traces its roots back to the early 1960s, has nowadays established its dominance in the engineering practice, and that is the finite element method.

The finite element method is a procedure which yields numerical solution of differential

equations governing a mathematical model that describes a physical problem. Core concept of the method lies in the discretisation of the mathematical model. The model is divided into smaller parts (finite elements) which are interconnected at discrete points (nodes) that contain unknown parameters of the problem. This process is called mesh generation in a finite element analysis. A finite element is defined by a function (or functions) that approximate an unknown solution within its domain in terms of unknown nodal parameters. A set of algebraic equations are obtained for each finite element, which are then assembled into a larger system of equations that make up the entire discretised model. A finite element solution is found by minimising the error of approximation via calculus of variations.

Clearly, the solution accuracy depends on a discretisation of the model. By introducing simple approximations in a finite element formulation, solutions of acceptable accuracies are generally obtained on a finely discretised model, i.e., the denser the finite element mesh is, the more accurate solution is obtained. However, dense finite element meshes translate into a very large system of algebraic equations that need to be solved.

For practical problems, a number of these equations can easily reach many thousands, or even millions, and a solution is desired relatively quickly in most cases. This leads to a certain compromise in terms of balancing the mathematical description of a physical problem and the discretisation fineness of the model. In order to optimise the finite element analysis, in many cases it is advantageous to improve the approximations within the finite element formulation. This particular approach has attracted attention of many researchers to date, and it is one of the main objectives of this thesis.

A finite element analysis of plates, shells and membranes translate into finding a solution in terms of displacements (and rotations), which are now unknown nodal parameters of the discretised model. Functions within the finite elements that approximate the unknown solution, i.e., displacement (and rotational) field(s), are called interpolations and they are usually polynomials. Finite elements are typically of triangular or quadrilateral shape, and they can include additional nodes inside its domain. A finite element solution is found via the variational principle of minimum total potential energy.

Only linear-elastic theories with small deformations are considered within the scope of this thesis. For plates, there are two widely accepted and used theories: Kirchhoff (Kirchhoff-Love) plate theory, also known as the classical plate theory, and Mindlin plate theory, also known as the first-order shear deformation plate theory. These theories also cover out-of-plane mechanics

of flat shells. In-plane mechanics of flat shells and membranes are described by the classical theory of plane elasticity.

Kirchhoff plate theory is based on an assumption that cross sections remain straight and normal to the middle surface after deformation. This means that the cross section rotations are equal to the derivatives of the transverse displacements, which is accurate only for the thin plate cases. As the plate thickness to span ratio increases, the error of such assumption rapidly increases as well. This is due to the disregarded shear strains which are getting more and more pronounced as the thickness to span ratio increases. Mindlin plate theory recognises these shear strains which makes the theory applicable to moderately thick plate cases as well. As a consequence, the cross section rotations are now treated as unknown parameters, just like the transverse displacements.

Plate finite elements based on Kirchhoff plate theory need to satisfy the C^1 continuity, i.e., interpolations for transverse displacements between adjacent finite elements need to be continuous in their first derivatives (slope continuity). Such requirement is necessary in order to evaluate the surface integrals that define the finite element stiffness, and in which a strain definition is associated with second derivatives of the transverse displacements. If those interpolations are only C^0 continuous, integrated terms may become infinite. This results in many difficulties regarding the development of Kirchhoff plate finite elements.

On the other hand, plate finite elements based on Mindlin plate theory only need to satisfy the C^0 continuity because strain definitions are associated with first derivatives of transverse displacements and rotations only. This makes the development of Mindlin plate finite elements much easier and less limiting. However, Mindlin plate finite elements are generally susceptible to the so-called shear locking which occurs when the plate thickness to span ratio approaches zero (thin limit cases).

The shear locking is a phenomenon that is characterised by an unrealistically large shear strains, and consequently, an inaccurate solution which suggests that the plate is much stiffer than it actually is. To eliminate, or at least to reduce the shear locking, many different methods have been successfully utilised. One of the methods that has been proven effective is an assumed strain method introduced by Hughes and Tezduyar [1] and MacNeal [2], and another one is a linked interpolation approach originally suggested by Xu [3], while the term itself was introduced by Zienkiewicz *et al.* in Refs. [4,5]. Both of these approaches are utilised here in order to develop new Mindlin plate finite elements.

Classical theory of elasticity is well established and accepted for more than a century. According to the theory, there are two orthogonal displacement fields in plane elasticity problems which describe the in-plane flat shell and membrane kinematics. A simple and reliable finite element for plane elasticity problems has been found in the early days of the finite element method. However, it has also been found that it is not very effective in terms of accuracy for general cases, and as a result of that, dense finite element meshes are required. Over the years, improvements have been proposed, many of which introduce rotations as additional unknown parameters, which are often referred to as drilling rotations or drilling degrees of freedom. Even though such approach is not actually consistent with the theory, it has proven to be advantageous in the finite element application.

New flat shell finite elements are formed here by joining out-of-plane Mindlin plate bending part and in-plane membrane part, i.e., Mindlin plate and membrane finite elements. For instance, by joining a Kirchhoff plate element and a conventional plane elasticity element, a shell element with three unknown parameters per node is obtained. These parameters are displacements in all three orthogonal directions of 3D space. Should a Mindlin plate element being joined instead, two additional unknown parameters, i.e., two orthogonal rotations, would be added on top of the previous three. This would make for a shell element with five unknown parameters per node.

Since a rigid body has six degrees of freedom in 3D space, three orthogonal displacements and three orthogonal rotations, an additional rotational degree of freedom would naturally complete the mathematical description of a general 3D shell problem, and that is the drilling rotation from the membrane finite element formulation. A shell finite element with all six degrees of freedom provides two key advantages over a five degrees of freedom element: a global stiffness matrix singularity is always avoided and fully compatible connections between shell and other types of finite elements are accomplished if drilling rotations represent actual nodal rotations in the finite element formulation.

New finite elements presented here are of triangular shape with nodes being at the vertices only. Since three non-collinear points (nodes) uniquely define a flat plane, these finite elements are flat by default. Curved problems can be adequately represented by a model made up of smaller flat finite elements, which is an additional approximation in a finite element analysis. With the finite element mesh refinement, such approximation becomes more accurate. Additionally, triangular elements are generally preferred since quadrilaterals are be prone to potential warping issues.

Additional information and explanations regarding this topic so far can be found in greater detail in Refs. [6–13].

A substantial overview of Mindlin plate finite elements development up to 2015 was given by Cen and Shang [14]. The authors have presented many different approaches and methods used throughout the history of Mindlin plate finite elements development in order to eliminate (or at least, to reduce) the shear locking and improve the element performance, such as: (selective) reduced integration [15], discrete Kirchhoff theory [16], various assumed strain concepts [1,2,17], linked interpolation [3–5], hybrid and mixed formulations, etc.

Even though the shear locking can be eliminated on Timoshenko beam finite elements by using the linked interpolation, it has been found that the same approach cannot ensure the same for Mindlin plate finite elements on its own. For this, one may refer to the work presented by Ribarić and Jelenić [18, 19] in which the authors made a comprehensive study of linked interpolation approach for lowest and higher-order quadrilateral and triangular Mindlin plate finite elements by following a displacement-based approach. Regardless, various effective three-node Mindlin plate finite elements using linked interpolation have been presented where improvements were sought in terms of utilising additional approaches and methods in order to eliminate the shear locking and improve the element performance.

Auricchio and Taylor [20] followed a mixed formulation approach, where quadratic linked interpolation is used, and in which rotational fields are enriched with internal degrees of freedom in order to match the so-called count conditions. In addition, shear strains are assumed constant and are interpolated independently. The element in question is the default three-node plate finite element used by the Finite Element Analysis Program (FEAP).

Soh *et al.* [21] applied constant shear strain expression of the two-node Timoshenko beam finite element with problem-dependent cubic linked interpolation along the each of the plate element side. Rotational fields are obtained by generalising this beam element's interpolation for rotations. Chen and Cheung [22] re-constituted shear strains obtained from the same Timoshenko beam element interpolations in discrete points of the plate element, while the rotational fields are obtained in the same manner as in Ref. [21]. Huang *et al.* [23] also used the same Timoshenko beam element interpolations to develop a hybrid displacement function finite element.

For plane elasticity problems, Turner *et al.* [24] formulated the first isoparametric three-node finite element known today as the CST (Constant Strain Triangle) element. Due to its simplicity and reliability, the CST element is still widely employed today, even though its performance is

generally not on an desirable level. In order to improve its performance, many researches resorted to introducing rotations as additional unknown parameters. Although that is not consistent with the theory since rotations are dependent on displacements, it is not actually against the finite element concept. Anyhow, difficulties were encountered in the early attempts of such approach. One of the main difficulties is linking nodal rotations to the element side displacements, which is very well explained and illustrated in Ref. [25]. In contrast, this is not a problem for beam or plate finite elements.

First successful realisation of introducing rotations as additional unknown parameters was presented independently by Allman [26] for plane elasticity problems, and by Carpenter *et al.* [27] for general shell problems. The authors introduced rotations with the quadratic interpolations of the displacement fields in a way known today as the linked interpolation. However, these finite elements possess the so-called spurious zero-energy mode, which is an undesirable finite element phenomenon. Additionally, the rotational parameters are not representing true rotations at the nodes of the discretised model. Allman has solved both of these issues later in Ref. [28] by adding a specific cubic level of interpolation to the element formulation. However, that addition has unfortunately lowered the element performance.

Boutagouga [29] recently made a substantial overview of membrane finite elements with rotational degrees of freedom. The author has presented many different approaches and methods used throughout the history of membrane finite element development in order to improve the performance of elements which utilise rotational degrees of freedom, such as: incompatible modes method [30], the so-called free formulation [25], strain-based approach [31], hybrid and mixed formulations, etc.

Various membrane finite elements with drilling rotations have been developed in a way that the rotations in the element formulation are not actually true rotations at nodes of the discretised model, but parameters of rotational nature that enrich displacement fields in a way that increases the element performance, e.g., membrane finite elements presented in Refs. [26,32,33]. Since the rotational field on its own has no contribution to the strain energy, those rotational parameters do not necessarily assume the values of true nodal rotations, but values which would make the strain energy provided by the displacement fields, minimal.

However, it is convenient to use a membrane finite element with true rotational degrees of freedom in finite element analyses, especially if such element is the in-plane part of the shell finite element formulation. In addition to advantages mentioned previously for general 3D shell

problems, such element has an inherent ability to carry in-plane moments correctly. Additional convenience is having values of true rotations at nodes of the discretised model, so if required, it is not necessary to compute them from displacements as they are given by the finite element solution directly. Some membrane finite elements with true rotational degrees of freedom of interest are presented in Refs. [28,34–37].

Although many effective three-node membrane finite elements with drilling rotations have been developed so far, no such element has been found capable of achieving the exact response for an arbitrary pure bending problem. This is likely due to the difficulties of linking nodal rotations to the element side, as mentioned previously. In contrast, lowest-order linked interpolation beam and plate finite elements have such capacity. More to the point, such element would be of a major importance in the finite element analyses [35]; hence, a considerable attention is given to that in this thesis.

Regarding the thesis itself, an introduction to the theory is given in Chapter 2 where Mindlin plate theory and classical theory of plane elasticity are briefly covered, in addition to the basics of the finite element procedure. The development and validation of new finite elements is presented in Chapters 3-5. Mindlin plate finite elements are based on the two-node Timoshenko beam finite element with problem-dependent cubic linked interpolation. The shear locking phenomenon is avoided by following the assumed strain method. Membrane finite elements with rotational degrees of freedom are developed in a way that the rotational parameters are true rotations, i.e., classical theory of elasticity definition of rotation is fully satisfied. Additionally, certain strain assumptions are made within the element domain in order to improve the performance of one of the elements, and as for the other, appropriate displacement interpolations for accomplishing exact response for certain pure bending cases are assumed. Flat shell finite elements are then formed by joining Mindlin plate and membrane finite elements. All developed finite elements are subjected to the so-called patch tests and tested on a variety of standard numerical examples, as well as compared with the finite elements used in the Finite Element Analysis Program (FEAP), in addition to other known finite elements from the literature. Finally, the thesis is concluded in Chapter 6 which summarises the presented work and findings.

Chapter 2

Theory

2.1 Mindlin plate theory

Mindlin plate theory is applicable to both thin and moderately thick plate cases since it recognises shear deformations, unlike Kirchhoff plate theory. Both of these theories share the following assumptions:

- the material is homogeneous, isotropic and linear elastic,
- the plate deformations are small,
- the plate is flat in its undeformed state,
- the middle plane of the plate remains unstrained as the plate deforms,
- the plate cross sections remain plane as the plate deforms, and
- the normal stress σ_z perpendicular to the middle plane of the plate is negligible.

The major difference between these two theories is that Mindlin plate theory dismisses the Kirchhoff assumption that the cross sections remain normal to the middle plane of the plate after deformation. This means that the cross section rotations are not equal to the derivatives of the transverse displacements, and that is due to the shear strains. For thin plate cases, the Kirchhoff assumption is accurate enough since these shear strains are very small and practically negligible.

A deformed plate configuration according to Mindlin plate theory is described for the Cartesian coordinate system in terms of the following middle plane parameters: transversal displacements $w(x, y)$ and two global section rotations $\theta_x(x, y)$ and $\theta_y(x, y)$, as shown in Fig. 2.1. The

displacement field inside the entire plate domain is, in respect to the middle plane ($z = 0$), assumed as

$$u(x, y, z) = z\theta_y(x, y), \qquad v(x, y, z) = -z\theta_x(x, y) \qquad \text{and} \qquad w(x, y, z) = w(x, y)\,, \tag{2.1}$$

where u, v and w are displacements in the x, y and z direction, respectively.

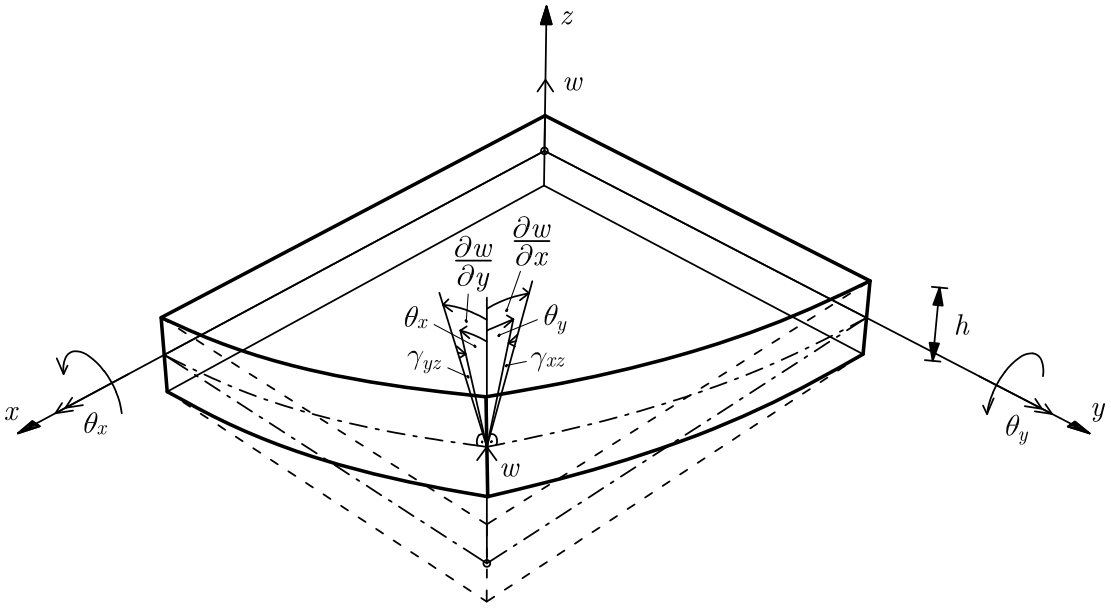

Figure 2.1: Mindlin plate after deformation

Shear strains (γ_{xz}, γ_{yz}) and curvatures (κ_x, κ_y, κ_{xy}) can be expressed via the kinematic equations as

$$\begin{Bmatrix} \gamma_{xz} \\ \gamma_{yz} \end{Bmatrix} = \begin{Bmatrix} \dfrac{\partial w}{\partial x} + \theta_y \\ \dfrac{\partial w}{\partial y} - \theta_x \end{Bmatrix} \tag{2.2}$$

and

$$\begin{Bmatrix} \kappa_x \\ \kappa_y \\ \kappa_{xy} \end{Bmatrix} = \begin{Bmatrix} \dfrac{\partial \theta_y}{\partial x} \\ -\dfrac{\partial \theta_x}{\partial y} \\ \dfrac{\partial \theta_y}{\partial y} - \dfrac{\partial \theta_x}{\partial x} \end{Bmatrix}. \tag{2.3}$$

Moments (M_x, M_y, M_{xy}) and shear stress resultants (S_x, S_y) can be expressed via the constitutive equations as

$$\begin{Bmatrix} M_x \\ M_y \\ M_{xy} \end{Bmatrix} = D \begin{bmatrix} 1 & \nu & 0 \\ \nu & 1 & 0 \\ 0 & 0 & \dfrac{1-\nu}{2} \end{bmatrix} \begin{Bmatrix} \kappa_x \\ \kappa_y \\ \kappa_{xy} \end{Bmatrix} = \mathbf{D_b} \begin{Bmatrix} \kappa_x \\ \kappa_y \\ \kappa_{xy} \end{Bmatrix}, \tag{2.4}$$

where

$$D = \frac{E\,h^3}{12\,(1-\nu^2)}\,, \tag{2.5}$$

and

$$\begin{Bmatrix} S_x \\ S_y \end{Bmatrix} = G\,k\,h \begin{bmatrix} 1 & 0 \\ 0 & 1 \end{bmatrix} \begin{Bmatrix} \gamma_{xz} \\ \gamma_{yz} \end{Bmatrix} = \mathbf{D_s} \begin{Bmatrix} \gamma_{xz} \\ \gamma_{yz} \end{Bmatrix}. \tag{2.6}$$

In the equations above, E is Young's modulus, h is the plate thickness, ν is Poisson's ratio, G is the shear modulus and k is the shear correction factor.

Equilibrium equations of the differential plate element can be written in terms of moments and shear stress resultants as

$$\begin{gathered} \frac{\partial M_x}{\partial x} + \frac{\partial M_{xy}}{\partial y} = S_x\,, \\ \frac{\partial M_{xy}}{\partial x} + \frac{\partial M_y}{\partial y} = S_y \\ \text{and} \\ \frac{\partial S_x}{\partial x} + \frac{\partial S_y}{\partial y} = -q(x,y)\,, \end{gathered} \tag{2.7}$$

where q is the distributed loading which is assumed to act perpendicular to the middle plane of the plate. These equations can be rewritten in terms of displacements and rotations as

$$\begin{gathered} \frac{D}{2}\left[(1-\nu)\,\nabla^2\,\theta_y + (1+\nu)\,\frac{\partial}{\partial x}\left(\frac{\partial \theta_y}{\partial x} - \frac{\partial \theta_x}{\partial y}\right)\right] - G\,k\,h\left(\frac{\partial w}{\partial x} + \theta_y\right) = 0\,, \\ -\frac{D}{2}\left[(1-\nu)\,\nabla^2\,\theta_x - (1+\nu)\,\frac{\partial}{\partial y}\left(\frac{\partial \theta_y}{\partial x} - \frac{\partial \theta_x}{\partial y}\right)\right] - G\,k\,h\left(\frac{\partial w}{\partial y} - \theta_x\right) = 0 \\ \text{and} \\ G\,k\,h\left[\nabla^2\,w + \left(\frac{\partial \theta_y}{\partial x} - \frac{\partial \theta_x}{\partial y}\right)\right] + q = 0\,, \end{gathered} \tag{2.8}$$

where ∇^2 is the two-dimensional Laplace operator.

2.2 Classical theory of plane elasticity

Classical theory of plane elasticity describes mechanics of flat bodies whose one dimension is either very small or very large in comparison to the other two dimensions. Consequently, there are two general types of problems describing each, plane stress and plane strain, respectively. A deformed body configuration can be described for the Cartesian coordinate system in terms of two orthogonal displacement fields: $u(x, y)$ in the x direction and $v(x, y)$ in the y direction, as shown in Fig. 2.2. Additionally, strains are assumed to be small.

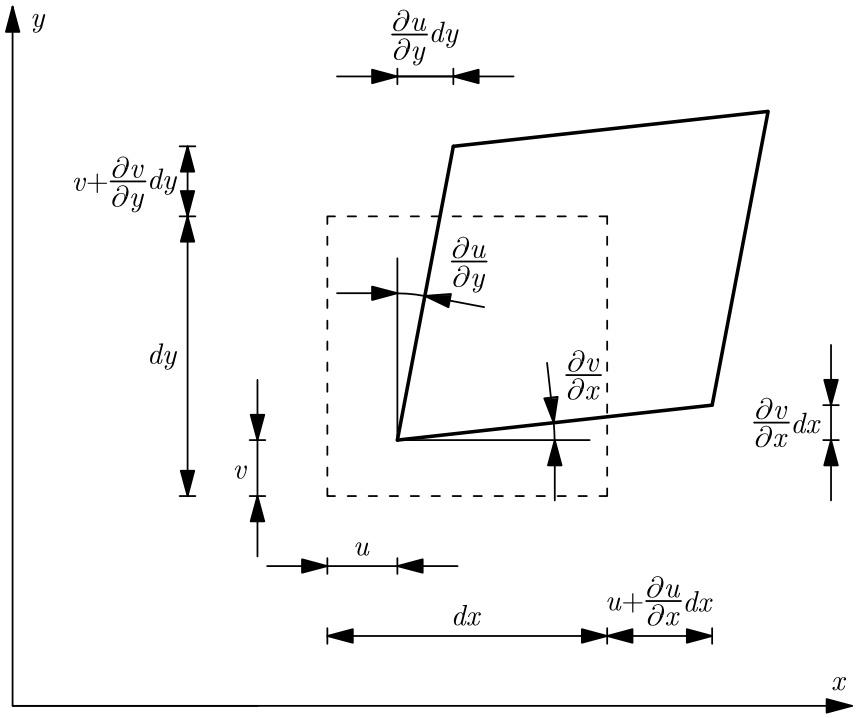

Figure 2.2: Differential 2D element after displacement and deformation

Normal strains (ε_x, ε_y) and shear strain (γ_{xy}) can be expressed via the kinematic equations as

$$\begin{Bmatrix} \varepsilon_x \\ \varepsilon_y \\ \gamma_{xy} \end{Bmatrix} = \begin{Bmatrix} \dfrac{\partial u}{\partial x} \\ \dfrac{\partial v}{\partial y} \\ \dfrac{\partial v}{\partial x} + \dfrac{\partial u}{\partial y} \end{Bmatrix}. \tag{2.9}$$

A plane stress state is considered here only due to the scope of this thesis. In such state, stresses directed perpendicular to the x-y plane (σ_z, τ_{xz}, τ_{yz}) are assumed to be zero, i.e.,

$$\sigma_z = \tau_{xz} = \tau_{yz} = 0\,, \tag{2.10}$$

where z is the direction perpendicular to the x-y plane. Normal stresses (σ_x, σ_y) and shear stress (τ_{xy}) can be expressed via the constitutive equations for a homogeneous, isotropic and linear elastic material as

$$\begin{Bmatrix} \sigma_x \\ \sigma_y \\ \tau_{xy} \end{Bmatrix} = \frac{E}{1-\nu^2} \begin{bmatrix} 1 & \nu & 0 \\ \nu & 1 & 0 \\ 0 & 0 & \dfrac{1-\nu}{2} \end{bmatrix} \begin{Bmatrix} \varepsilon_x \\ \varepsilon_y \\ \gamma_{xy} \end{Bmatrix} = \mathbf{D_m} \begin{Bmatrix} \varepsilon_x \\ \varepsilon_y \\ \gamma_{xy} \end{Bmatrix}. \tag{2.11}$$

Additionally, it follows that the strains directed perpendicular to the x-y plane (ε_z, γ_{xz}, γ_{yz}) are

$$\begin{Bmatrix} \varepsilon_z \\ \gamma_{xz} \\ \gamma_{yz} \end{Bmatrix} = \begin{Bmatrix} -\dfrac{\nu}{E}(\sigma_x + \sigma_y) \\ 0 \\ 0 \end{Bmatrix}. \tag{2.12}$$

Equilibrium equations of the differential 2D element can be written in terms of stresses as

$$\begin{gathered} \frac{\partial \sigma_x}{\partial x} + \frac{\partial \tau_{xy}}{\partial y} + X = 0 \\ \text{and} \\ \frac{\partial \tau_{xy}}{\partial x} + \frac{\partial \sigma_y}{\partial y} + Y = 0\,, \end{gathered} \tag{2.13}$$

where X and Y are the body forces per unit volume in the x and y direction, respectively. These equations can be rewritten in terms of displacements as

$$\begin{gathered} \frac{1}{2}\frac{E}{1-\nu^2}\left[(1-\nu)\nabla^2 u + (1+\nu)\frac{\partial}{\partial x}\left(\frac{\partial u}{\partial x} + \frac{\partial v}{\partial y}\right)\right] + X = 0 \\ \text{and} \\ \frac{1}{2}\frac{E}{1-\nu^2}\left[(1-\nu)\nabla^2 v + (1+\nu)\frac{\partial}{\partial y}\left(\frac{\partial u}{\partial x} + \frac{\partial v}{\partial y}\right)\right] + Y = 0\,. \end{gathered} \tag{2.14}$$

2.3 The finite element procedure

Instead of finding the strong form solutions of the partial differential equations, which are for practical boundary value problems usually non-existent, a weak (integral) form is obtained by following the principle of virtual work. A weak solution is found via the variational principle of minimum total potential energy.

The total potential energy, written as a functional Π, can be expressed as

$$\Pi = U + W \tag{2.15}$$

where U is the strain energy of the system and W is the potential energy of the external loads. Equilibrium is ensured if the total potential energy is stationary, i.e.,

$$\delta\Pi = \delta(U + W) = 0\,. \tag{2.16}$$

If u is set as an unknown displacement function that represents the solution of the problem, the total potential energy of the problem is stationary for arbitrary variations of the displacements δu. With the approximation of the displacement function, the total potential energy of the problem can be rewritten as

$$\Pi = \frac{1}{2}\tilde{\mathbf{u}}^{\mathrm{T}}\mathbf{K}\tilde{\mathbf{u}} - \tilde{\mathbf{u}}^{\mathrm{T}}\mathbf{f}\,, \tag{2.17}$$

where $\tilde{\mathbf{u}}$ are the approximated unknown displacements, $\mathbf{K}$ is the stiffness matrix and $\mathbf{f}$ is the load vector. Finite element equations can be obtained now for a finite number (n) of $\tilde{\mathbf{u}}$ parameters by making the Π stationary for all $\delta\tilde{\mathbf{u}}$ as

$$\frac{\partial\Pi}{\partial\tilde{\mathbf{u}}} = \left\{\begin{array}{c} \dfrac{\partial\Pi}{\partial\tilde{u}_1} \\ \dfrac{\partial\Pi}{\partial\tilde{u}_2} \\ \vdots \\ \dfrac{\partial\Pi}{\partial\tilde{u}_n} \end{array}\right\} = \mathbf{K}\tilde{\mathbf{u}} - \mathbf{f} = 0\,. \tag{2.18}$$

A stable equilibrium in which the total potential energy is at its minimum is achieved if $\mathbf{K}$ is a positive-definite matrix, which is the case for linear elastic problems. Additionally, $\mathbf{K}$ is also symmetric ($\mathbf{K} = \mathbf{K}^{\mathrm{T}}$).

With the discretisation of the problem domain on finite elements, the displacement function

approximation is assumed for each finite element rather than for the entire domain. Consequently, each finite element has its own stiffness matrix $\mathbf{K}^e$, which can be written in a general form as

$$\mathbf{K}^e = \int_{\Omega_e} \mathbf{B}^{\mathrm{T}} \mathbf{D} \mathbf{B} \, d\Omega \,, \tag{2.19}$$

where $\mathbf{B}$ is the strain-displacement matrix and $\mathbf{D}$ is the elasticity matrix. Element stiffness matrices are then assembled into a larger matrix which represents the global stiffness matrix of the entire problem ($\mathbf{K}$) by summing the coefficients that relate to the same displacements.

By rewriting Eq. (2.18) as

$$\mathbf{K}\tilde{\mathbf{u}} = \mathbf{f} \,, \tag{2.20}$$

a finite element solution can be obtained in terms of the unknown displacements $\tilde{\mathbf{u}}$ as

$$\tilde{\mathbf{u}} = \mathbf{K}^{-1}\mathbf{f} \tag{2.21}$$

after inserting the displacement boundary conditions. However, in practice the stiffness matrix $\mathbf{K}$ is not inverted, but rather Eq. (2.20) is solved by a direct or iterative method.

Chapter 3

Mindlin plate finite elements

3.1 Two-node Timoshenko beam finite element with problem-dependent cubic linked interpolation

Mindlin plate finite elements presented in this chapter are based on the two-node Timoshenko beam finite element with the problem-dependent cubic linked interpolation. Basis for such an approach is the close kinematic relation between Mindlin plate theory and Timoshenko beam theory, since Mindlin plate theory may be regarded as a generalisation of Timoshenko beam theory to two-dimensional problems.

Interpolations for transverse displacements (w) and rotations (θ) for the two-node Timoshenko beam finite element with the problem-dependent cubic linked interpolation are derived by satisfying the differential equations of the Timoshenko beam, and can be written using the natural coordinate $\xi \in [-1, 1]$ as

$$\begin{aligned} w = & \frac{w_1 + w_2}{2} - \xi \frac{w_1 - w_2}{2} \\ & - (1 - \xi^2) \frac{L}{4} \frac{\theta_1 - \theta_2}{2} \\ & - \xi (1 - \xi^2) \frac{L}{4} \left(\frac{w_1 - w_2}{L} - \frac{\theta_1 + \theta_2}{2} \right) \frac{1}{1 + \dfrac{12\,E\,I}{L^2\,G\,k\,A}} \end{aligned} \tag{3.1}$$

and

$$\begin{aligned} \theta = & \frac{\theta_1 + \theta_2}{2} - \xi \frac{\theta_1 - \theta_2}{2} \\ & + (1 - \xi^2) \frac{3}{2} \left(\frac{w_1 - w_2}{L} - \frac{\theta_1 + \theta_2}{2} \right) \frac{1}{1 + \dfrac{12\,E\,I}{L^2\,G\,k\,A}} \,. \end{aligned} \tag{3.2}$$

In these equations, L is the element length, I the second moment of area and A the area of cross section. Complete derivation of these equations can be found in Ref. [38].

Following the kinematic equation $\gamma = (dw/dx) + \theta$, where the dx is the differential segment of the beam, shear strain (γ) is obtained as constant throughout the element, and can be expressed as

$$\gamma = -\left(\frac{w_1 - w_2}{L} - \frac{\theta_1 + \theta_2}{2}\right) \frac{1}{1 + \dfrac{12\,E\,I}{L^2\,G\,k\,A}}\,. \tag{3.3}$$

The term *cubic linked interpolation* refers to the cubic polynomial interpolation order of the transverse displacements, while the interpolation order of the rotations is one order lower (quadratic). In addition, interpolations are linked, i.e., the higher-order polynomial terms in the interpolation for the transverse displacements include the nodal rotations and vice versa. As for the term *problem-dependent*, it refers to the dependence of the interpolations on the geometric and the material properties of the beam [39].

This beam finite element is free of shear locking and is capable of returning the exact results for certain load cases [12]. Additionally, it has been successfully utilised for Mindlin plate finite elements in the literature [21–23, 40–42].

3.2 Displacement-based approach

Following the displacement-based approach is the classical procedure used in the finite element development. In such procedure, a displacement function is interpolated throughout the finite element domain as a starting point. Strain-displacement matrices $\mathbf{B}$ that are used to form the finite element stiffness matrix $\mathbf{K}^e$ [Eq. (2.19)] after integration are derived from the displacement function by following the kinematic equations [Eq. (2.2)].

Mindlin plate finite elements have three independent displacement[1] fields: transverse displacement field (w) and two orthogonal rotational fields (θ_x, θ_y). Consequently, Mindlin plate finite elements have three degrees of freedom (or three unknown parameters) per node. A three-node Mindlin plate finite element with its nodal degrees of freedom is shown in Fig. 3.1.

An arbitrary point inside the three-node finite element domain can be defined with area coordinates ξ_1, ξ_2 and ξ_3, as shown in Fig. 3.2, where a_i and b_i are the element side projections, L_i the element side lengths, A_i areas defined by the point inside the element and the element sides ($i = 1, 2, 3$), while A is the total area of the element.

[1] The term displacement here is meant in its wider sense.

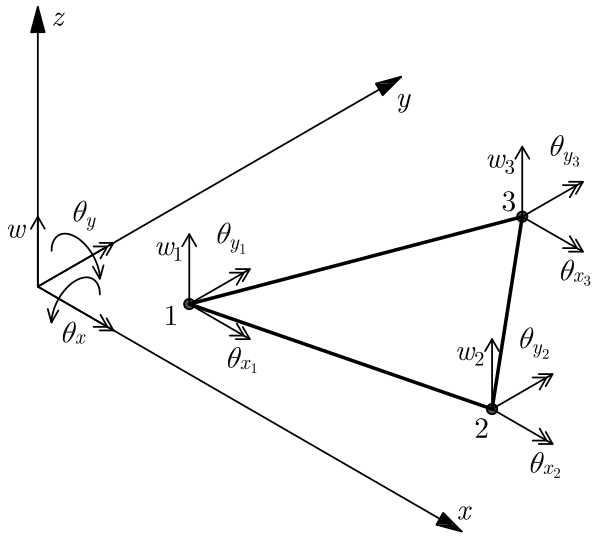

Figure 3.1: Degrees of freedom of a three-node Mindlin plate finite element

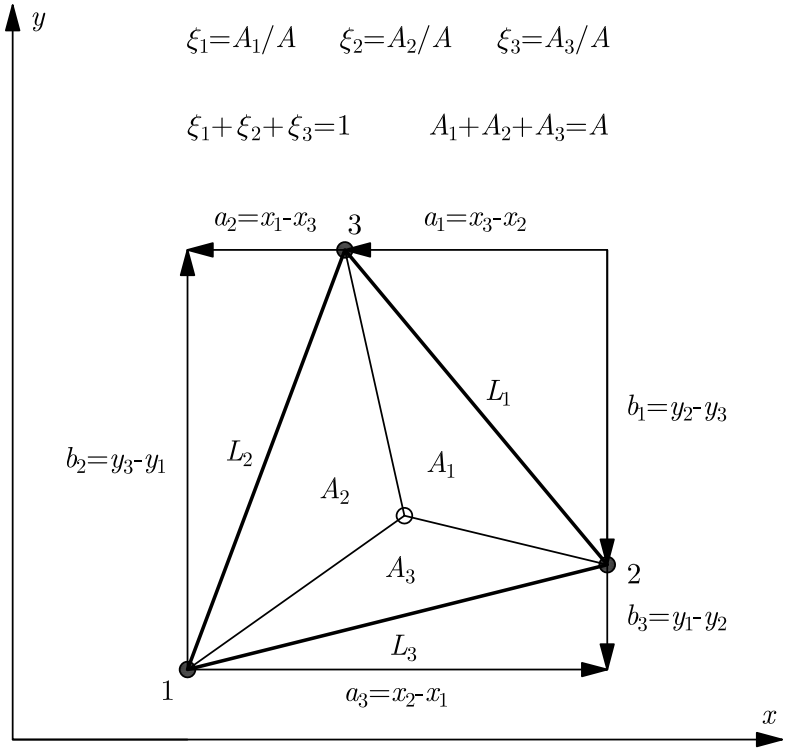

Figure 3.2: A three-node finite element geometry and area coordinates

Interpolations for the transverse displacement field and the rotational fields are derived here for the new three-node Mindlin plate finite element by generalising the Timoshenko beam finite element described in the previous section (Sec. 3.1), and can be written as

$$\begin{aligned} w = {} & \xi_1\, w_1 + \xi_2\, w_2 + \xi_3\, w_3 \\ & + \xi_1\, \xi_2\, c_{qw_3} + \xi_2\, \xi_3\, c_{qw_1} + \xi_3\, \xi_1\, c_{qw_2} \\ & + (\xi_1 - \xi_2)\, \xi_1\, \xi_2\, c_{cw_3} + (\xi_2 - \xi_3)\, \xi_2\, \xi_3\, c_{cw_1} + (\xi_3 - \xi_1)\, \xi_3\, \xi_1\, c_{cw_2} + \xi_1\, \xi_2\, \xi_3\, c_{bw}\,, \end{aligned} \tag{3.4}$$

$$\begin{aligned} \theta_x = {} & \xi_1\, \theta_{x_1} + \xi_2\, \theta_{x_2} + \xi_3\, \theta_{x_3} \\ & + \xi_1\, \xi_2\, c_{q\theta_{x3}} + \xi_2\, \xi_3\, c_{q\theta_{x1}} + \xi_3\, \xi_1\, c_{q\theta_{x2}} \end{aligned} \tag{3.5}$$

and

$$\begin{aligned} \theta_y = {} & \xi_1\, \theta_{y_1} + \xi_2\, \theta_{y_2} + \xi_3\, \theta_{y_3} \\ & + \xi_1\, \xi_2\, c_{q\theta_{y3}} + \xi_2\, \xi_3\, c_{q\theta_{y1}} + \xi_3\, \xi_1\, c_{q\theta_{y2}}\,, \end{aligned} \tag{3.6}$$

where

$$c_{qw_i} = -\frac{\theta_{x_j} - \theta_{x_k}}{2}\, b_i - \frac{\theta_{y_j} - \theta_{y_k}}{2}\, a_i \tag{3.7}$$

are the quadratic polynomial coefficients in the transverse displacement field and

$$c_{cw_i} = c_i\, m_i \tag{3.8}$$

are the cubic polynomial coefficients in the transverse displacement field, with

$$c_i = w_j - w_k - \frac{\theta_{x_j} + \theta_{x_k}}{2}\, b_i - \frac{\theta_{y_j} + \theta_{y_k}}{2}\, a_i \tag{3.9}$$

and the problem-dependent parameters

$$m_i = \frac{1}{1 + \dfrac{2\,h^2}{{L_i}^2\, k\, (1 - \nu)}}\,. \tag{3.10}$$

The quadratic polynomial coefficients in the rotational fields are also dependent on c_{cw_i} and can be expressed as

$$c_{q\theta_{x\,i}} = 6\, c_{cw_i}\, \frac{b_i}{{L_i}^2} \tag{3.11}$$

and

$$c_{q\theta_{y_i}} = 6\, c_{cw_i}\, \frac{a_i}{{L_i}^2}\,. \tag{3.12}$$

In these equations, indices i, j and k are cyclic permutations of the node numbers and also the element side numbers taken anticlockwise, as shown in Fig. 3.2.

An internal (bubble) degree of freedom (c_{bw}) is added in the transverse displacement field [Eq. (3.4)] for the polynomial completeness of the cubic interpolation (ten cubic terms in the Pascal triangle). Its function is maximum at the element centroid, while zero on the element edges. It is thus statically condensed in the final assembly of the element stiffness matrix.

Since these interpolations are derived by generalising the two-node beam element interpolations, conformity is fulfilled as common sides of adjacent plate elements have the same nodal and geometric parameters involved in the interpolations.

Ribarić presented two four-node Mindlin plate finite elements named Q4-U3 and Q4-U3R5 in Ref. [38] by following the same approach. Before that, Ribarić and Jelenić presented a three-node Mindlin plate finite element with quadratic linked interpolation named T3-U2 in Ref. [19], which can be regarded as a lower-order polynomial version of the element presented in this section. Accordingly, the new element is named T3-U3.

It shall be noted that by following the kinematic equations [Eq. (2.2)], the resulting shear strain fields (γ_{xz}, γ_{yz}) are obtained as quadratic polynomials, whereas for the Timoshenko beam finite element, the shear strain is constant [Eq. (3.3)].

3.3 Assumed strain method

In contrast to the classical displacement-based approach, strains in the assumed strain method are not derived from displacement interpolations by following the kinematic equations. Generally, there are partial or complete kinematic inconsistencies between strains and displacement interpolations. Moreover, displacement interpolations are in some finite element formulations completely disregarded. It is the concept of the assumed strain method to abandon displacement interpolations in favour of strain interpolations, as it has been proven to be effective in development of new high performing finite elements.

By following a displacement-based approach, shear strains for Mindlin plate finite elements are generally obtained from kinematic equations as higher-order polynomials, contrary to that obtained from equilibrium equations. The shear locking phenomenon is postulated to be the

result of such inconsistency. With the shear strain interpolations that are assumed as lower-order polynomials, mostly as zero-order (constant) or first-order (linear) polynomials, the shear locking is reduced, or even eliminated. Displacement-based Mindlin plate finite elements with reduced integration of shear strain terms have been proven to be superior in performance and less susceptible to the shear locking than those fully integrated.

Given the advantages of the assumed strain method, shear strain interpolations are now assumed directly by generalising the alongside shear strain expression [Eq. (3.3)] of the Timoshenko beam finite element described in Sec. 3.1. Shear strains for each plate element side (γ_i) can be derived by generalising this shear strain expression as

$$\gamma_i = -c_i \, \frac{1 - m_i}{L_i} \, . \tag{3.13}$$

These shear strains can be represented as rotation vectors with perpendicular direction and with constant magnitude throughout their respective element sides, as shown in Fig. 3.3. Since c_i involve only the nodal and geometric parameters of the corresponding element side, the shear strains γ_i are conforming between two adjacent elements sharing the same side.

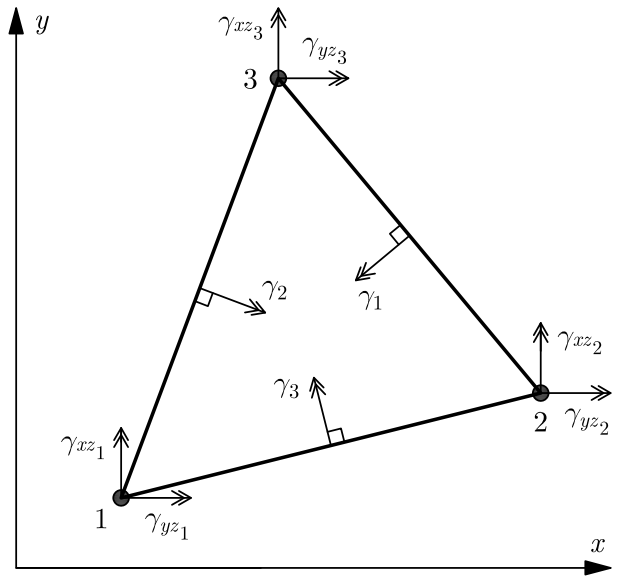

Figure 3.3: Rotation vector representation of the shear strains

With the alongside shear strains γ_i joining at the element nodes (Fig. 3.3), it follows that the global nodal shear strains can be uniquely expressed as

$$\gamma_{xz_i} = \frac{\gamma_k \, L_k \, b_j - \gamma_j \, L_j \, b_k}{2 \, A} \tag{3.14}$$

and

$$\gamma_{yz_i} = \frac{\gamma_k\, L_k\, a_j - \gamma_j\, L_j\, a_k}{2\, A}\,. \tag{3.15}$$

Consequently, the shear strain fields can be assumed linear throughout the element as

$$\gamma_{xz} = \xi_1\, \gamma_{xz_1} + \xi_2\, \gamma_{xz_2} + \xi_3\, \gamma_{xz_3} \tag{3.16}$$

and

$$\gamma_{yz} = \xi_1\, \gamma_{yz_1} + \xi_2\, \gamma_{yz_2} + \xi_3\, \gamma_{yz_3}\,. \tag{3.17}$$

Such approach for obtaining the shear strain fields has already been taken by Soh *et al.* [21]. Additionally, the authors derived the rotational fields in the same way previously shown for the T3-U3 element.

One interesting point is that if the problem-dependent parameters m_i are disregarded from Eq. (3.13), the resulting shear strain fields would be exactly the same as those obtained from the T3-U2 element.

A transverse displacement field of a cubic polynomial order can be derived next in a way that the kinematic equations [Eq. (2.2)] are satisfied, which is not typical for the assumed strain concept. For that, it is sufficient to check the kinematic equations at the element nodes. Since the kinematic equations are checked at the element nodes, the rotational fields only involve their nodal parameters (rotations). The resulting transverse displacement field can be written as

$$\begin{aligned} w = {} & \xi_1\, w_1 + \xi_2\, w_2 + \xi_3\, w_3 \\ & + \xi_1\, \xi_2\, c_{qw_3} + \xi_2\, \xi_3\, c_{qw_1} + \xi_3\, \xi_1\, c_{qw_2} \\ & + (\xi_1 - \xi_2)\, \xi_1\, \xi_2\, c_{cw_3} + (\xi_2 - \xi_3)\, \xi_2\, \xi_3\, c_{cw_1} + (\xi_3 - \xi_1)\, \xi_3\, \xi_1\, c_{cw_2} \end{aligned} \tag{3.18}$$

and it is exactly the same as that for the T3-U3 element [Eq. (3.4)], apart from the bubble term c_{bw} which, like its first derivatives, has no effect at the element nodes.

By taking a step further in such approach, rotational fields of a quadratic polynomial order can be derived in the same way by checking the kinematic equations [Eq. (2.2)] in the element side midpoints. With that, the resulting rotational fields follow as

$$\begin{aligned} \theta_x = {} & \xi_1\, \theta_{x_1} + \xi_2\, \theta_{x_2} + \xi_3\, \theta_{x_3} \\ & + \xi_1\, \xi_2\, c_{q\theta_{x_3}} + \xi_2\, \xi_3\, c_{q\theta_{x_1}} + \xi_3\, \xi_1\, c_{q\theta_{x_2}} \end{aligned} \tag{3.19}$$

and

$$\begin{aligned}\theta_y = {} & \xi_1\,\theta_{y_1} + \xi_2\,\theta_{y_2} + \xi_3\,\theta_{y_3} \\ & + \xi_1\,\xi_2\,c_{q\theta_{y_3}} + \xi_2\,\xi_3\,c_{q\theta_{y_1}} + \xi_3\,\xi_1\,c_{q\theta_{y_2}}\,,\end{aligned} \tag{3.20}$$

where

$$c_{q\theta_{x_i}} = \frac{3\,c_{cw_i}\,(a_j - a_k) - (c_{cw_j} - c_{cw_k})\,a_i}{2\,A} \tag{3.21}$$

and

$$c_{q\theta_{y_i}} = -\frac{3\,c_{cw_i}\,(b_j - b_k) - (c_{cw_j} - c_{cw_k})\,b_i}{2\,A}\,. \tag{3.22}$$

This completes a finite element formulation that has a full kinematic consistency, and accordingly, the new finite element is named T3-LSC (Triangular element with 3 nodes, Linear Shear strain fields and a kinematically Consistent formulation).

The approach presented here in which a full kinematic consistency is established is not common to the assumed strain method. As a result of that, shear part of the stiffness matrix for the T3-LSC element can be formed either directly by using the shear strain expressions (3.16) and (3.17) or by using a classical procedure where shear strain fields are obtained from kinematic equations [Eq. (2.2)]. The latter allows for an addition of the internal degree of freedom c_{bw} in the transverse displacement field [Eq. (3.18)], which would fulfil the polynomial completeness of the cubic interpolation. It is interesting to note that during the numerical investigation, it was found that the addition of c_{bw} has no effect on the results. Also, complete kinematic consistency would hold with the addition of c_{bw} if the quadratic coefficients in the rotational fields become

$$c_{q\theta_{x_i}} = \frac{3\,c_{cw_i}\,(a_j - a_k) - (c_{cw_j} - c_{cw_k})\,a_i + c_{bw}\,a_i}{2\,A} \tag{3.23}$$

and

$$c_{q\theta_{y_i}} = -\frac{3\,c_{cw_i}\,(b_j - b_k) - (c_{cw_j} - c_{cw_k})\,b_i + c_{bw}\,b_i}{2\,A}\,. \tag{3.24}$$

However, convergence issues arise in such case with the static condensation of c_{bw} in the final assembly of the element stiffness matrix.

In contrast to the approach taken to derive the rotational fields for the T3-LSC element, the following quadratic polynomial coefficients in the rotational fields are considered additionally:

$$c_{q\theta_{x_i}} = p\,\frac{c_{cw_i}\,(a_j - a_k) - (c_{cw_j} - c_{cw_k})\,a_i}{2\,A} \tag{3.25}$$

and

$$c_{q\theta_{y_i}} = -p\,\frac{c_{cw_i}\,(b_j - b_k) - (c_{cw_j} - c_{cw_k})\,b_i}{2\,A}\,, \tag{3.26}$$

where p is an arbitrary value. These coefficients have a special property which makes them vanish if a reduced numerical integration (1 point Gauss quadrature) is carried out for the bending part of the stiffness matrix, effectively reducing the interpolations of the rotational fields to a linear level. Such a particular feature possibly account for the passing of the patch test regardless of the element size, and consequently, for the good convergence properties, as shown later in Section 3.5. Clearly, full numerical integration (3 point Gauss quadrature) for the bending part of the stiffness matrix is adopted for a new finite element formulation, in addition to the optimal value for p ($p = 4$), which is chosen as such based on the effectiveness observed in all benchmark problems. Lower values of p result in softer response, whereas higher values result in stiffer response. Additionally, influence of p diminishes with finite element mesh refinement. Since these quadratic polynomial coefficients in the rotational fields are kinematically independent to the rest of the finite element formulation, the new finite element is named T3-LSI (Triangular element with 3 nodes, Linear Shear strain fields and Independent rotational fields).

The quadratic polynomial coefficients $c_{q\theta_{x_i}}$ and $c_{q\theta_{y_i}}$, which are related to each finite element side, involve all nodal and geometric parameters of the corresponding element. This results in nonconforming rotational fields for both T3-LSC and T3-LSI elements.

3.4 Stiffness matrix and uniform load vector

Shear strains [Eq. (2.2)] and curvatures [Eq. (2.3)] can be re-written in the following form:

$$\boldsymbol{\gamma} = \mathbf{B_s}\,\mathbf{u_p} \tag{3.27}$$

and

$$\boldsymbol{\kappa} = \mathbf{B_b}\,\mathbf{u_p}\,, \tag{3.28}$$

where $\mathbf{B_s}$ and $\mathbf{B_b}$ are strain-displacement matrices and

$$\mathbf{u_p} = \left\{ w_1 \quad \theta_{x_1} \quad \theta_{y_1} \quad w_2 \quad \theta_{x_2} \quad \theta_{y_2} \quad w_3 \quad \theta_{x_3} \quad \theta_{y_3} \right\}^{\mathrm{T}} \tag{3.29}$$

is a vector of unknown nodal degrees of freedom.

The finite element stiffness matrix is then formed with two independent contributions, the shear energy part, and the bending energy part, by integrating over the element domain as

$$\mathbf{K_p}^e = \mathbf{K_s}^e + \mathbf{K_b}^e = \int_{A_e} \mathbf{B_s}^{\mathbf{T}} \mathbf{D_s} \mathbf{B_s} \, dA + \int_{A_e} \mathbf{B_b}^{\mathbf{T}} \mathbf{D_b} \mathbf{B_b} \, dA \,. \tag{3.30}$$

Shear part of the stiffness matrix for the presented assumed strain finite elements is formed quickly since their shear strain fields are defined directly. Consequently, this adds to the computational efficiency of these elements.

If a plate is subjected to a uniformly distributed load, integration of the transverse displacement interpolation has to be carried out in order to determine the element load vector ($\mathbf{f}^e$). In such case, the element load vector can be obtained as

$$\mathbf{f}^e = \int_{A_e} q \, w \, dA \,, \tag{3.31}$$

where q is the constant load intensity. In that regard, the uniform load vector for the T3-U3 element is obtained by integrating the transverse displacement field expression from (3.4), in contrast to the one from (3.18) for the T3-LSC and T3-LSI elements. Given the linked form of the elements' transverse displacement fields, the resulting load vectors consist not only of nodal forces, but also of nodal moments. Additionally, contribution of the cubic part in the transverse displacement field to the element load vector calculated for the uniformly distributed load are, apart from the term related to a bubble shape (c_{bw}), equal to zero due to their antisymmetric shapes.

3.5 Numerical examples

In this section, the presented elements T3-U3, T3-LSC and T3-LSI are analysed on a variety of standard benchmark examples, and the results are compared to other relevant elements from the literature: T3-2LIM by Auricchio and Taylor [20], ARS-T9 by Soh *et al.* [21], RDKTM by Chen and Cheung [22] and HDF-P3-7β by Huang *et al.* [23]. The presented elements, in addition to

the ARS-T9 element, have been incorporated into the Finite Element Analysis Program (FEAP) [43] in which all numerical examples have been performed. That allowed for a comprehensive comparison with the T3-2LIM element which is the default three-node plate finite element in FEAP. The results of the RDKTM and HDF-P3-7β elements are taken from the original papers [22, 23]. The HDF-P3-7β element results are in the original paper given normalised to the reference solutions, and they are recalculated here for comparative purposes.

All elements used in the comparison have some similarities and equalities in the approach and the formulation, e.g., the linked interpolation concept is common to all elements. The ARS-T9 and RDKTM elements have the same interpolations for the rotational fields, whereas the ARS-T9, T3-LSC and T3-LSI elements have the same interpolations for the shear strain fields. The results from the numerical examples indicate that the performance of ARS-T9 and RDKTM elements is almost identical. Additionally, these two elements perform basically the same as the DKT element (Discrete Kirchhoff Triangle [16]) for very thin plate cases.

3.5.1 Patch test

First numerical example is a patch test for a constant bending state. Functions for the transverse displacements and the rotations are taken from Ref. [44] as:

$$\begin{gathered} w = (1 + x + 2\,y + x^2 + x\,y + y^2)/2\,, \\ \theta_x = (2 + x + 2\,y)/2 \\ \text{and} \\ \theta_y = -(1 + 2\,x + y)/2\,. \end{gathered} \tag{3.32}$$

The patch test model is defined with the arbitrary mesh shown in Fig. 3.4 where the transverse displacements and the rotations are given in the external nodes (1, 2, 7 and 8) and checked in the internal nodes (3, 4, 5 and 6). The plate properties are $E = 10^5$, $\nu = 0.25$, $k = 5/6$, with h being taken as 0.01 for thin and 1.0 for thick plate case. The expected moments are $M_x = M_y = -11111.\dot{1}\,h^3$ and $M_{xy} = -3333.\dot{3}\,h^3$ and they are constant over the entire patch domain, in addition to the shear stress resultants which are equal to zero.

The presented elements T3-U3 and T3-LSI pass the patch test as the exact transverse displacements and rotations are obtained in the internal nodes, as shown in Table 3.1. Additionally, exact moments and zero shear stress resultants are obtained in the integration points. The T3-

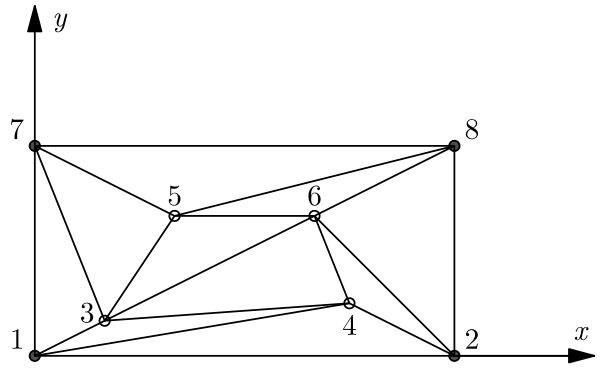

Node	x	y
1	0.00	0.00
2	0.24	0.00
3	0.04	0.02
4	0.18	0.03
5	0.08	0.08
6	0.16	0.08
7	0.00	0.12
8	0.24	0.12

Figure 3.4: Patch test mesh

LSC element does not pass the patch test on the finite element mesh defined in Fig. 3.4. However, as the mesh gets denser, convergence to the exact results is achieved, and when the size of the elements become infinitesimal, the patch test is passed. If the exact transverse displacements and the rotations are given in all nodes, the T3-LSC element would yield the exact stress resultants regardless of the element size.

The presented elements have a correct rank as only three eigenvalues corresponding to the rigid body modes, are equal to zero, i.e., the presented elements have no spurious zero-energy modes. Table 3.2 shows eigenvalues only for the element enclosed by nodes 3, 4 and 6.

Table 3.1: Constant bending patch test results

		T3-LSC			T3-U3 / T3-LSI / Exact		
Node	h	w	θ_x	θ_y	w	θ_x	θ_y
3	0.01	5.4133E-01	1.0361E+00	-5.4889E-01	5.4140E-01	1.0400E+00	-5.5000E-01
	1.0	5.4049E-01	1.0402E+00	-5.4958E-01			
4	0.01	6.3913E-01	1.1144E+00	-6.9372E-01	6.3935E-01	1.1200E+00	-6.9500E-01
	1.0	6.3942E-01	1.1199E+00	-6.9451E-01			
5	0.01	6.2917E-01	1.1191E+00	-6.1664E-01	6.2960E-01	1.1200E+00	-6.2000E-01
	1.0	6.2818E-01	1.1199E+00	-6.1954E-01			
6	0.01	6.8204E-01	1.1613E+00	-7.0424E-01	6.8240E-01	1.1600E+00	-7.0000E-01
	1.0	6.8143E-01	1.1598E+00	-6.9978E-01			
		Strain energy			Strain energy		
	0.01	3.4933E-04			3.6800E-04		
	1.0	3.6768E+02			3.6800E+02		

Table 3.2: Eigenvalues of the plate element enclosed by nodes 3, 4 and 6

Element	h	1 7	2 8	3 9	4	5	6
T3-U3	0.01	3.0725E+02 2.4237E-14	2.7743E+00 -9.1873E-15	7.1032E-02 -1.1065E-16	2.0395E-02	3.1793E-03	1.9423E-03
	1.0	8.4174E+04 -5.8926E-12	2.2612E+04 -3.1127E-12	9.9242E+03 2.6762E-12	9.3431E+03	2.4533E+03	1.0015E+01
T3-LSC	0.01	4.6604E+01 -8.8324E-15	1.7071E+01 -1.3018E-15	1.2358E-02 2.1963E-17	9.6023E-03	2.4758E-03	2.3728E-03
	1.0	8.3835E+04 -8.4570E-12	2.3139E+04 2.6067E-12	9.8859E+03 -1.8174E-12	9.3813E+03	2.4557E+03	9.9760E+00
T3-LSI	0.01	7.6439E+01 3.4831E-15	4.7577E+00 -3.0647E-15	2.4922E-02 1.5401E-17	2.2603E-02	2.5753E-03	2.4565E-03
	1.0	8.3945E+04 -3.5293E-12	2.2604E+04 2.8738E-12	1.0014E+04 -2.0269E-12	9.4072E+03	2.4561E+03	1.0025E+01

3.5.2 Square plate

Uniformly loaded square plate with the loading intensity $q = 1$ and the plate properties being $E = 10.92$, $\nu = 0.3$ and $k = 5/6$ is analysed next. Different span to thickness ratios are considered in order to check very thin to thick plate cases. In addition, two different mesh types A and B are analysed. Due to the orthogonal symmetry of the problem, only quarter of the square plate model is analysed, as shown in Fig. 3.5. The results are given numerically in Tables 3.3-3.8, and graphically in Figs. 3.6-3.9.

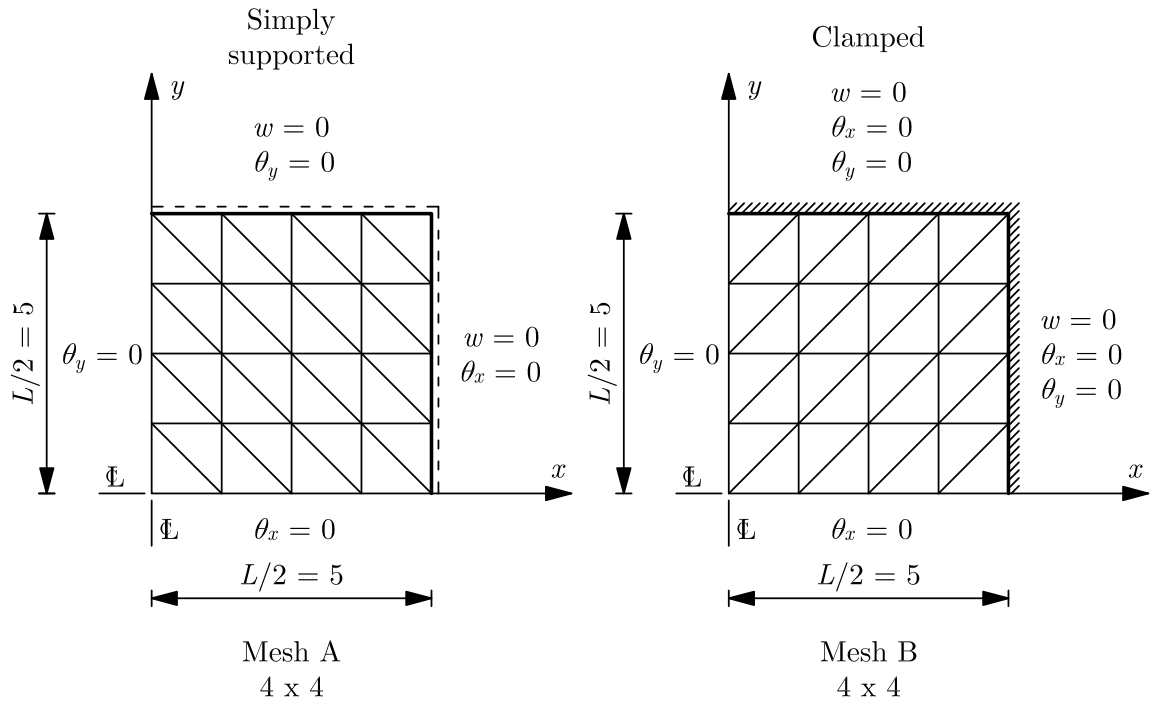

Figure 3.5: Square plate models

The T3-U3 element exhibits shear locking behaviour in this numerical example on coarse meshes. Interestingly, the shear locking is not pronounced so much on Mesh A when the boundary conditions are simply supported. With the finite element mesh refinement, the shear locking behaviour fades rapidly. On the other hand, the T3-LSC element does not yield accurate moments on very dense meshes when the plate is very thin, even though it is convergent in terms of the displacement values. Other than that, the presented elements perform well, with the T3-LSI element among the best performing.

Table 3.3: Normalised central displacement $w/(10^{-2}\,q\,L^4/D)$ of the uniformly loaded simply supported square plate (Mesh A)

			$L/h = 1000$		
Mesh	T3-2LIM	ARS-T9	T3-U3	T3-LSC	T3-LSI
2 x 2	0.39910	0.36756	0.32571	0.46002	0.40253
4 x 4	0.40452	0.39726	0.32995	0.42434	0.40521
8 x 8	0.40585	0.40406	0.36455	0.41253	0.40595
16 x 16	0.40614	0.40570	0.39979	0.40860	0.40616
32 x 32	0.40621	0.40610	0.40576	0.40720	0.40622
64 x 64	0.40623	0.40620	0.40620	0.40664	0.40623
Ref. [4]			0.40624		
			$L/h = 100$		
Mesh	T3-2LIM	ARS-T9	T3-U3	T3-LSC	T3-LSI
2 x 2	0.39930	0.36773	0.34054	0.46015	0.40272
4 x 4	0.40473	0.39743	0.39069	0.42445	0.40543
8 x 8	0.40606	0.40424	0.40503	0.41255	0.40618
16 x 16	0.40635	0.40588	0.40634	0.40849	0.40639
32 x 32	0.40642	0.40630	0.40643	0.40702	0.40644
64 x 64	0.40644	0.40641	0.40644	0.40657	0.40644
Ref. [4]			0.40644		
			$L/h = 10$		
Mesh	T3-2LIM	ARS-T9	T3-U3	T3-LSC	T3-LSI
2 x 2	0.41836	0.38452	0.41743	0.47466	0.42098
4 x 4	0.42502	0.41649	0.42494	0.44157	0.42576
8 x 8	0.42667	0.42446	0.42650	0.43123	0.42686
16 x 16	0.42712	0.42656	0.42706	0.42836	0.42716
32 x 32	0.42724	0.42710	0.42722	0.42758	0.42725
64 x 64	0.42727	0.42724	0.42727	0.42736	0.42728
Ref. [4]			0.42728		
			$L/h = 5$		
Mesh	T3-2LIM	ARS-T9	T3-U3	T3-LSC	T3-LSI
2 x 2	0.47286	0.43704	0.47102	0.52500	0.47490
4 x 4	0.48534	0.47641	0.48460	0.50107	0.48598
8 x 8	0.48896	0.48672	0.48871	0.49343	0.48914
16 x 16	0.49002	0.48946	0.48995	0.49126	0.49006
32 x 32	0.49032	0.49018	0.49030	0.49066	0.49033
64 x 64	0.49040	0.49037	0.49039	0.49050	0.49040
Ref. [21]			0.4906		

Table 3.4: Normalised central displacement $w/(10^{-2}\,q\,L^4/D)$ of the uniformly loaded simply supported square plate (Mesh B)

$L/h = 1000$						
Mesh	T3-2LIM	ARS-T9	HDF-P3-7β	T3-U3	T3-LSC	T3-LSI
2 x 2	0.38412	0.40559	0.40120	0.00405	0.42772	0.39536
4 x 4	0.40114	0.40649	0.40518	0.06342	0.41225	0.40320
8 x 8	0.40503	0.40637	0.40600	0.29303	0.40868	0.40545
16 x 16	0.40594	0.40628	0.40620	0.39577	0.40743	0.40604
32 x 32	0.40616	0.40625		0.40554	0.40685	0.40619
64 x 64	0.40622	0.40624		0.40619	0.40654	0.40623
Ref. [4]	0.40624					
$L/h = 100$						
Mesh	T3-2LIM	ARS-T9	RDKTM	T3-U3	T3-LSC	T3-LSI
2 x 2	0.38436	0.40577	0.4058	0.19722	0.42787	0.39559
4 x 4	0.40137	0.40665	0.4069	0.37981	0.41234	0.40343
8 x 8	0.40524	0.40653	0.4065	0.40454	0.40866	0.40569
16 x 16	0.40615	0.40645		0.40629	0.40728	0.40627
32 x 32	0.40637	0.40643		0.40641	0.40665	0.40641
64 x 64	0.40643	0.40644		0.40643	0.40646	0.40644
Ref. [4]	0.40644					
$L/h = 10$						
Mesh	T3-2LIM	ARS-T9	HDF-P3-7β	T3-U3	T3-LSC	T3-LSI
2 x 2	0.40786	0.42551	0.42361	0.42010	0.44500	0.41846
4 x 4	0.42293	0.42641	0.42604	0.42538	0.42948	0.42525
8 x 8	0.42627	0.42699	0.42690	0.42667	0.42718	0.42681
16 x 16	0.42704	0.42721	0.42719	0.42712	0.42711	0.42717
32 x 32	0.42723	0.42727		0.42725	0.42721	0.42726
64 x 64	0.42727	0.42728		0.42728	0.42726	0.42728
Ref. [4]	0.42728					
$L/h = 5$						
Mesh	T3-2LIM	ARS-T9	RDKTM	T3-U3	T3-LSC	T3-LSI
2 x 2	0.47582	0.49018	0.4902	0.48613	0.50654	0.48580
4 x 4	0.48752	0.49045	0.4904	0.48918	0.49261	0.48978
8 x 8	0.48989	0.49057	0.4906	0.49021	0.49058	0.49042
16 x 16	0.49034	0.49050		0.49042	0.49038	0.49047
32 x 32	0.49042	0.49046		0.49044	0.49040	0.49045
64 x 64	0.49043	0.49044		0.49043	0.49042	0.49044
Ref. [21]	0.4906					

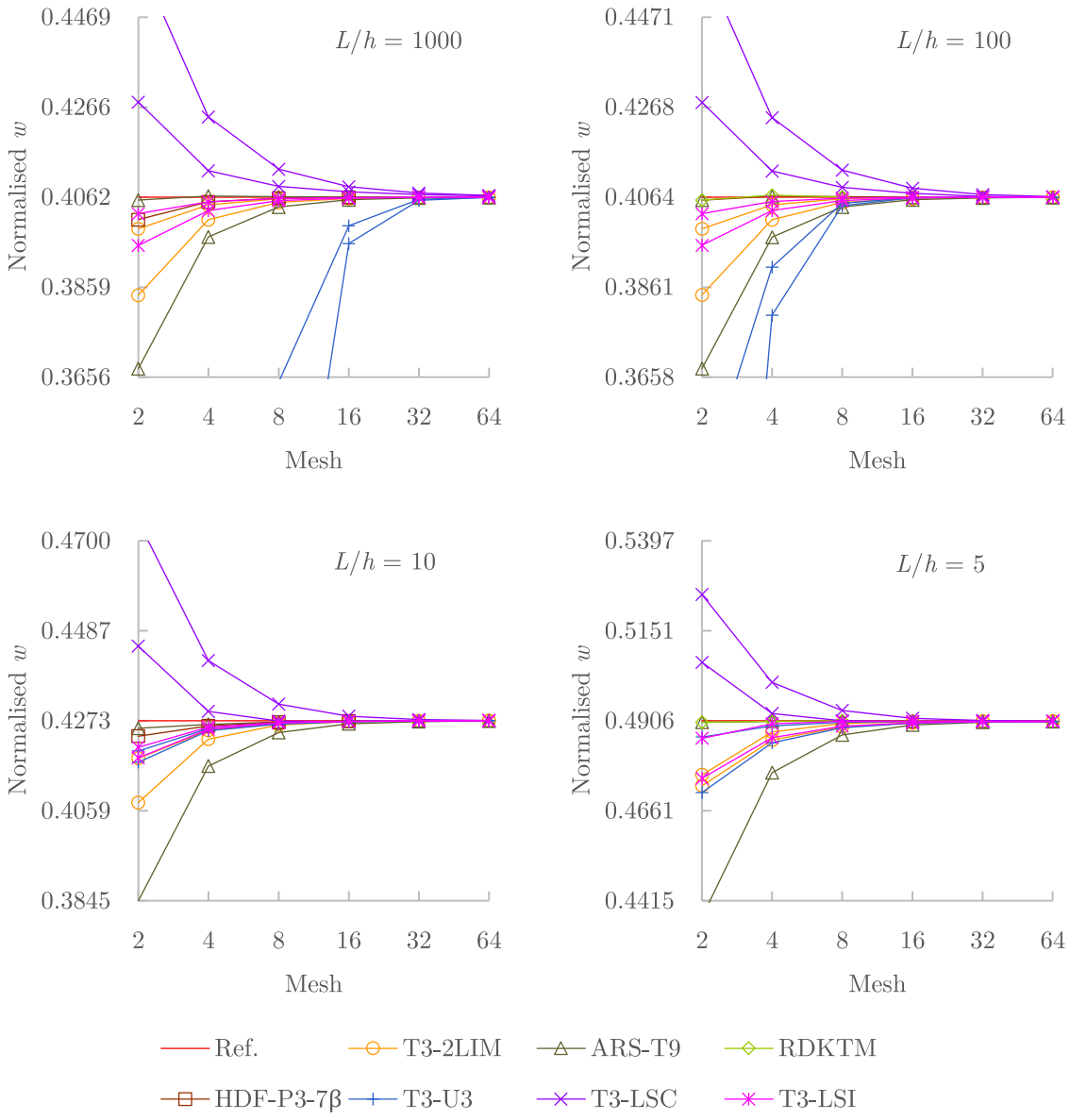

Figure 3.6: Normalised central displacement $w/(10^{-2}\,q\,L^4/D)$ of the uniformly loaded simply supported square plate (Mesh A and B)

Table 3.5: Normalised central moment $M/(10^{-2}\,q\,L^2)$ of the uniformly loaded simply supported square plate obtained in Gauss point that is closest to the centre of the plate (Mesh A and B)

$L/h = 1000$										
	T3-2LIM		ARS-T9		T3-U3		T3-LSC		T3-LSI	
Mesh	A	B	A	B	A	B	A	B	A	B
2 x 2	4.486	4.354	4.385	4.495	3.075	0.058	5.536	4.679	4.657	4.425
4 x 4	4.721	4.692	4.706	4.734	2.781	0.821	5.380	4.809	4.732	4.723
8 x 8	4.775	4.763	4.771	4.774	3.549	4.036	5.323	4.867	4.767	4.779
16 x 16	4.786	4.782	4.785	4.784	4.531	4.879	5.306	4.890	4.782	4.788
32 x 32	4.788	4.787	4.788	4.787	4.764	4.799	5.297	4.899	4.786	4.789
64 x 64	4.789	4.788	4.788	4.788	4.787	4.789	5.271	4.900	4.788	4.789
Ref. [4]	4.78863									
$L/h = 100$										
	T3-2LIM		ARS-T9		T3-U3		T3-LSC		T3-LSI	
Mesh	A	B	A	B	A	B	A	B	A	B
2 x 2	4.487	4.354	4.384	4.496	3.422	2.698	5.532	4.679	4.659	4.424
4 x 4	4.722	4.692	4.705	4.735	4.417	4.689	5.367	4.808	4.735	4.722
8 x 8	4.776	4.763	4.769	4.775	4.763	4.770	5.272	4.863	4.770	4.777
16 x 16	4.787	4.781	4.784	4.786	4.794	4.783	5.144	4.878	4.785	4.786
32 x 32	4.789	4.786	4.787	4.789	4.792	4.788	4.950	4.872	4.789	4.787
64 x 64	4.789	4.788	4.788	4.789	4.790	4.789	4.823	4.847	4.789	4.788
Ref. [4]	4.78863									
$L/h = 10$										
	T3-2LIM		ARS-T9		T3-U3		T3-LSC		T3-LSI	
Mesh	A	B	A	B	A	B	A	B	A	B
2 x 2	4.528	4.338	4.341	4.598	4.929	4.826	5.287	4.683	4.751	4.403
4 x 4	4.748	4.675	4.676	4.799	4.903	4.847	4.975	4.801	4.814	4.705
8 x 8	4.786	4.753	4.757	4.802	4.831	4.807	4.829	4.816	4.807	4.769
16 x 16	4.789	4.778	4.780	4.794	4.802	4.793	4.796	4.801	4.795	4.784
32 x 32	4.789	4.786	4.786	4.790	4.793	4.790	4.790	4.792	4.791	4.788
64 x 64	4.789	4.788	4.788	4.789	4.790	4.789	4.789	4.790	4.789	4.788
Ref. [4]	4.78863									
$L/h = 5$										
	T3-2LIM		ARS-T9		T3-U3		T3-LSC		T3-LSI	
Mesh	A	B	A	B	A	B	A	B	A	B
2 x 2	4.554	4.314	4.289	4.747	5.068	5.108	5.052	4.716	4.855	4.429
4 x 4	4.757	4.661	4.664	4.834	4.925	4.889	4.877	4.788	4.845	4.719
8 x 8	4.788	4.750	4.756	4.807	4.835	4.814	4.812	4.791	4.811	4.774
16 x 16	4.790	4.777	4.780	4.794	4.803	4.795	4.795	4.789	4.796	4.785
32 x 32	4.789	4.786	4.786	4.790	4.793	4.790	4.790	4.788	4.791	4.788
64 x 64	4.789	4.788	4.788	4.789	4.790	4.789	4.789	4.789	4.789	4.788
Ref.	-									

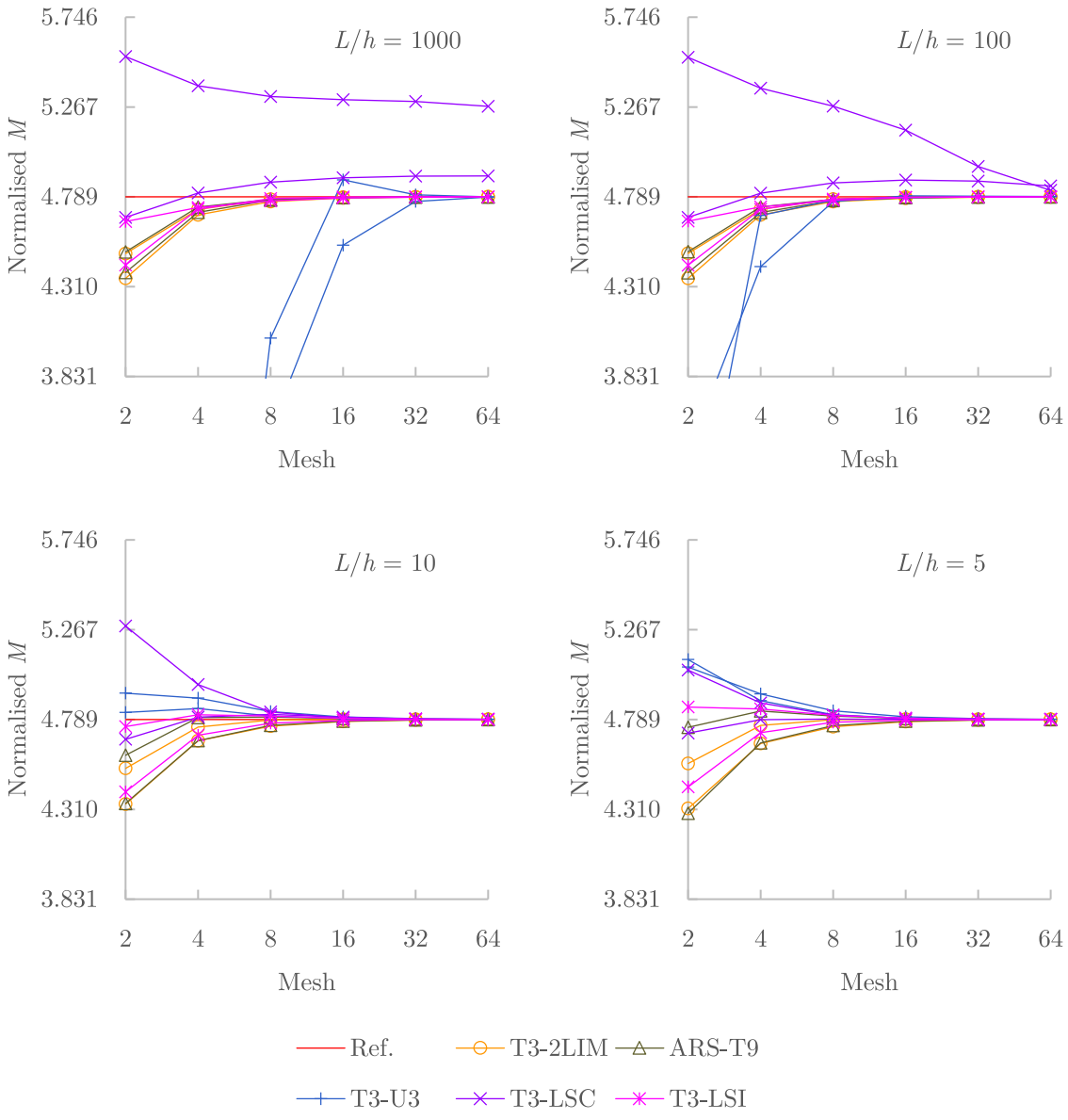

Figure 3.7: Normalised central moment $M/(10^{-2}\,q\,L^2)$ of the uniformly loaded simply supported square plate obtained in Gauss point that is closest to the centre of the plate (Mesh A and B)

Table 3.6: Normalised central displacement $w/(10^{-2}\,q\,L^4/D)$ of the uniformly loaded clamped square plate (Mesh A)

			$L/h = 1000$		
Mesh	T3-2LIM	ARS-T9	T3-U3	T3-LSC	T3-LSI
2 x 2	0.10537	0.12145	0.00067	0.13656	0.11289
4 x 4	0.12073	0.12578	0.01113	0.13267	0.12309
8 x 8	0.12504	0.12636	0.07556	0.12883	0.12566
16 x 16	0.12616	0.12649	0.12060	0.12740	0.12632
32 x 32	0.12644	0.12652	0.12607	0.12688	0.12648
64 x 64	0.12651	0.12653	0.12649	0.12668	0.12652
Ref. [4]			0.12653		
			$L/h = 100$		
Mesh	T3-2LIM	ARS-T9	T3-U3	T3-LSC	T3-LSI
2 x 2	0.10556	0.12162	0.04102	0.13671	0.11306
4 x 4	0.12098	0.12599	0.10897	0.13286	0.12332
8 x 8	0.12530	0.12658	0.12455	0.12900	0.12590
16 x 16	0.12641	0.12672	0.12643	0.12754	0.12656
32 x 32	0.12669	0.12676	0.12670	0.12700	0.12673
64 x 64	0.12676	0.12678	0.12676	0.12683	0.12677
Ref. [4]			0.12653		
			$L/h = 10$		
Mesh	T3-2LIM	ARS-T9	T3-U3	T3-LSC	T3-LSI
2 x 2	0.12451	0.13924	0.12313	0.15256	0.13012
4 x 4	0.14355	0.14730	0.14350	0.15335	0.14495
8 x 8	0.14862	0.14951	0.14848	0.15143	0.14895
16 x 16	0.14998	0.15020	0.14993	0.15075	0.15006
32 x 32	0.15034	0.15039	0.15032	0.15055	0.15036
64 x 64	0.15043	0.15044	0.15043	0.15049	0.15044
Ref. [4]			0.1499		
			$L/h = 5$		
Mesh	T3-2LIM	ARS-T9	T3-U3	T3-LSC	T3-LSI
2 x 2	0.17933	0.19312	0.17656	0.20422	0.18282
4 x 4	0.20665	0.21007	0.20585	0.21528	0.20754
8 x 8	0.21435	0.21520	0.21410	0.21688	0.21458
16 x 16	0.21645	0.21666	0.21638	0.21715	0.21650
32 x 32	0.21702	0.21706	0.21700	0.21721	0.21702
64 x 64	0.21716	0.21718	0.21716	0.21722	0.21717
Ref. [21]			0.2167		

Table 3.7: Normalised central displacement $w/(10^{-2}\,q\,L^4/D)$ of the uniformly loaded clamped square plate (Mesh B)

$L/h = 1000$						
Mesh	T3-2LIM	ARS-T9	HDF-P3-7β	T3-U3	T3-LSC	T3-LSI
2 x 2	0.12241	0.15474	0.12249	0.00067	0.14807	0.12920
4 x 4	0.12511	0.13474	0.12545	0.01219	0.13215	0.12632
8 x 8	0.12619	0.12866	0.12637	0.07947	0.12817	0.12640
16 x 16	0.12645	0.12707	0.12653	0.12171	0.12712	0.12650
32 x 32	0.12652	0.12667		0.12620	0.12678	0.12653
64 x 64	0.12653	0.12657		0.12651	0.12664	0.12653
Ref. [4]	0.12653					
$L/h = 100$						
Mesh	T3-2LIM	ARS-T9	RDKTM	T3-U3	T3-LSC	T3-LSI
2 x 2	0.12268	0.15496	0.1550	0.04215	0.14830	0.12947
4 x 4	0.12540	0.13497	0.1350	0.11210	0.13238	0.12661
8 x 8	0.12646	0.12888	0.1289	0.12550	0.12837	0.12670
16 x 16	0.12671	0.12730		0.12668	0.12727	0.12678
32 x 32	0.12677	0.12691		0.12676	0.12690	0.12679
64 x 64	0.12678	0.12681		0.12677	0.12680	0.12679
Ref. [4]	0.12653					
$L/h = 10$						
Mesh	T3-2LIM	ARS-T9	HDF-P3-7β	T3-U3	T3-LSC	T3-LSI
2 x 2	0.14815	0.17658	0.14945	0.14676	0.17119	0.15530
4 x 4	0.15010	0.15753	0.15018	0.14938	0.15550	0.15191
8 x 8	0.15037	0.15213	0.15015	0.14988	0.15149	0.15081
16 x 16	0.15044	0.15087	0.15036	0.15028	0.15066	0.15054
32 x 32	0.15046	0.15056		0.15042	0.15050	0.15048
64 x 64	0.15046	0.15049		0.15045	0.15047	0.15047
Ref. [4]	0.1499					
$L/h = 5$						
Mesh	T3-2LIM	ARS-T9	RDKTM	T3-U3	T3-LSC	T3-LSI
2 x 2	0.21831	0.24226	0.2423	0.21519	0.23993	0.22669
4 x 4	0.21820	0.22428	0.2243	0.21634	0.22313	0.22014
8 x 8	0.21761	0.21910	0.2191	0.21696	0.21860	0.21804
16 x 16	0.21735	0.21772		0.21718	0.21754	0.21746
32 x 32	0.21726	0.21735		0.21722	0.21730	0.21729
64 x 64	0.21723	0.21726		0.21722	0.21723	0.21724
Ref. [21]	0.2167					

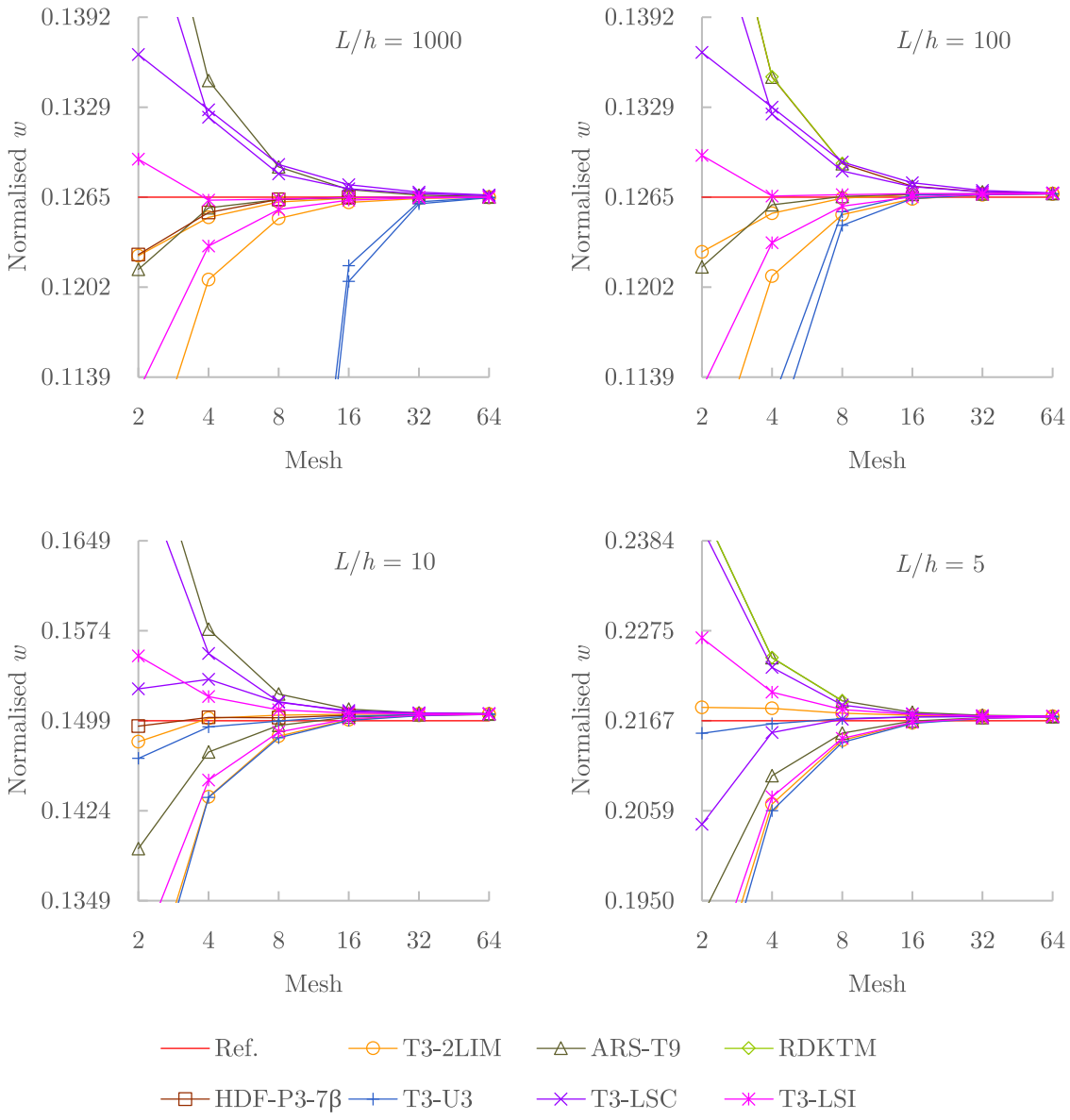

Figure 3.8: Normalised central displacement $w/(10^{-2}\,q\,L^4/D)$ of the uniformly loaded clamped square plate (Mesh A and B)

Table 3.8: Normalised central moment $M/(10^{-2}\,q\,L^2)$ of the uniformly loaded clamped square plate obtained in Gauss point that is closest to the centre of the plate (Mesh A and B)

$L/h = 1000$										
	T3-2LIM		ARS-T9		T3-U3		T3-LSC		T3-LSI	
Mesh	A	B	A	B	A	B	A	B	A	B
2 x 2	1.737	1.906	2.021	2.381	0.013	0.015	2.328	2.282	2.018	2.076
4 x 4	2.152	2.209	2.234	2.356	0.182	0.244	2.537	2.303	2.208	2.250
8 x 8	2.255	2.273	2.274	2.311	1.192	1.626	2.535	2.327	2.263	2.286
16 x 16	2.282	2.286	2.286	2.296	2.091	2.339	2.534	2.337	2.282	2.291
32 x 32	2.288	2.289	2.289	2.292	2.270	2.299	2.532	2.342	2.288	2.291
64 x 64	2.290	2.290	2.290	2.291	2.289	2.291	2.521	2.343	2.290	2.291
Ref. [4]	2.2905									
$L/h = 100$										
	T3-2LIM		ARS-T9		T3-U3		T3-LSC		T3-LSI	
Mesh	A	B	A	B	A	B	A	B	A	B
2 x 2	1.737	1.906	2.020	2.382	0.818	0.952	2.325	2.283	2.019	2.076
4 x 4	2.153	2.210	2.233	2.358	1.947	2.259	2.531	2.303	2.209	2.250
8 x 8	2.256	2.273	2.273	2.313	2.252	2.294	2.511	2.326	2.265	2.285
16 x 16	2.282	2.286	2.285	2.298	2.290	2.291	2.457	2.333	2.284	2.291
32 x 32	2.289	2.290	2.289	2.294	2.292	2.292	2.367	2.331	2.290	2.291
64 x 64	2.290	2.291	2.290	2.292	2.291	2.291	2.307	2.319	2.291	2.291
Ref. [4]	2.2905									
$L/h = 10$										
	T3-2LIM		ARS-T9		T3-U3		T3-LSC		T3-LSI	
Mesh	A	B	A	B	A	B	A	B	A	B
2 x 2	1.725	1.933	1.964	2.448	2.110	2.563	2.178	2.351	2.035	2.137
4 x 4	2.180	2.234	2.213	2.453	2.330	2.428	2.340	2.345	2.262	2.308
8 x 8	2.286	2.297	2.287	2.368	2.333	2.357	2.322	2.339	2.310	2.324
16 x 16	2.312	2.314	2.310	2.335	2.325	2.331	2.318	2.328	2.318	2.322
32 x 32	2.318	2.318	2.317	2.324	2.322	2.323	2.319	2.322	2.320	2.321
64 x 64	2.319	2.320	2.319	2.321	2.320	2.321	2.320	2.321	2.320	2.320
Ref. [4]	2.31									
$L/h = 5$										
	T3-2LIM		ARS-T9		T3-U3		T3-LSC		T3-LSI	
Mesh	A	B	A	B	A	B	A	B	A	B
2 x 2	1.709	1.922	1.914	2.564	2.206	2.740	2.035	2.487	2.054	2.246
4 x 4	2.193	2.264	2.213	2.518	2.360	2.521	2.287	2.416	2.286	2.379
8 x 8	2.317	2.333	2.315	2.411	2.365	2.409	2.339	2.372	2.341	2.370
16 x 16	2.347	2.351	2.345	2.373	2.360	2.371	2.352	2.361	2.353	2.362
32 x 32	2.355	2.356	2.354	2.362	2.358	2.361	2.356	2.358	2.356	2.359
64 x 64	2.357	2.357	2.356	2.359	2.358	2.358	2.357	2.358	2.357	2.358
Ref.	-									

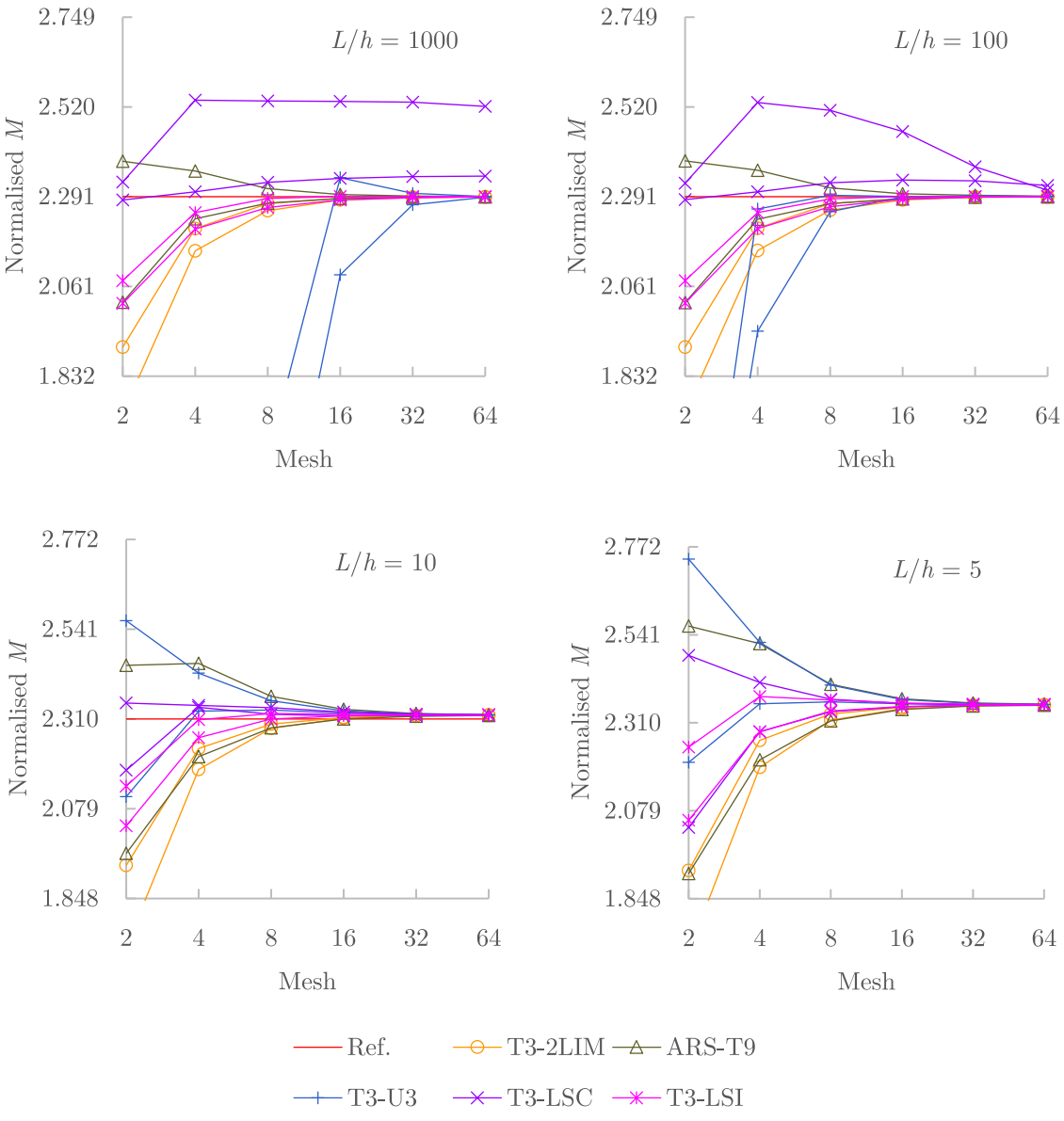

Figure 3.9: Normalised central moment $M/(10^{-2}\,q\,L^2)$ of the uniformly loaded clamped square plate obtained in Gauss point that is closest to the centre of the plate (Mesh A and B)

3.5.3 Circular plate

Uniformly loaded circular plate is analysed with the same loading intensity ($q = 1$) and the same plate properties ($E = 10.92$, $\nu = 0.3$ and $k = 5/6$). Different span to thickness ratios are also considered in order to check thin to thick plate cases. Similarly, due to the axisymmetric nature of the problem, only quarter of the circular plate model is analysed, as shown in Fig. 3.10.

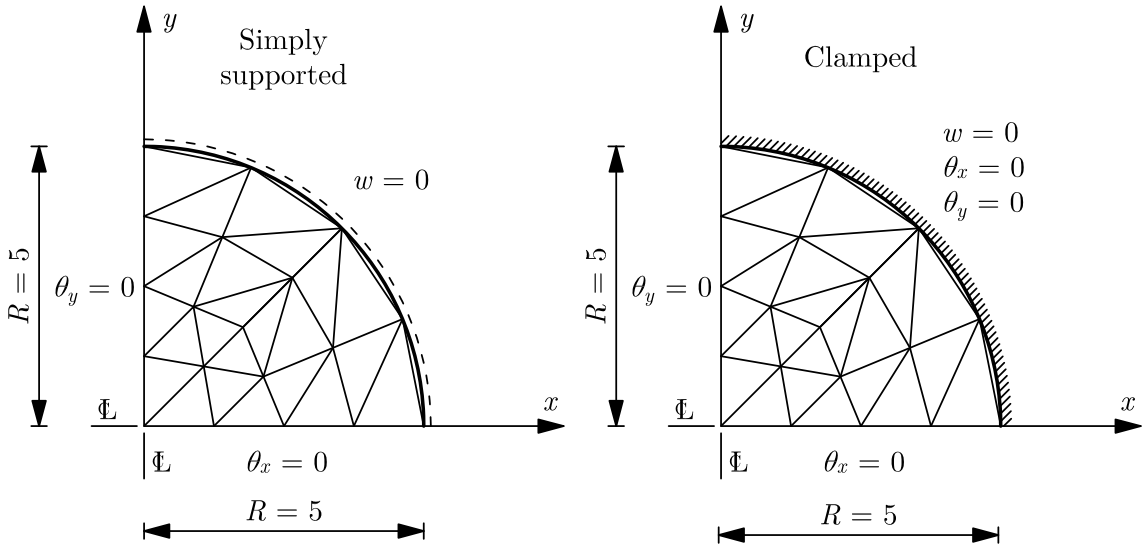

Number of elements
24

Figure 3.10: Circular plate models

The results from this benchmark problem, given numerically in Tables 3.9-3.12 and graphically in Figs. 3.11-3.14, indicate that the T3-U3 and T3-LSI elements perform better when the boundary conditions are simply supported, whereas the T3-LSC element performs better when the boundary conditions are clamped. The T3-LSI element exhibits very good ability to capture moments in all cases.

Table 3.9: Central displacement w of the uniformly loaded simply supported circular plate

$R/h = 50$							
Num. of elem.	T3-2LIM	ARS-T9	RDKTM	HDF-P3-7β	T3-U3	T3-LSC	T3-LSI
6	40847	37849	37849	40955	37120	46783	41492
24	40066	39397	39394	40127	39148	42295	40316
96	39888	39729	39730	39908	39786	40652	39961
Ref. [5]				39832			
$R/h = 5$							
Num. of elem.	T3-2LIM	ARS-T9	RDKTM	HDF-P3-7β	T3-U3	T3-LSC	T3-LSI
6	42.541	39.463	39.463	42.568	42.256	47.837	42.953
24	41.827	41.091	41.089	41.840	41.798	43.400	41.997
96	41.658	41.472	41.473	41.657	41.641	41.983	41.707
Ref. [5]				41.599			

Table 3.10: Central moment M of the uniformly loaded simply supported circular plate obtained in Gauss point that is closest to the centre of the plate

$R/h = 50$					
Num. of elem.	T3-2LIM	ARS-T9	T3-U3	T3-LSC	T3-LSI
6	4.777	4.667	4.479	5.312	5.423
24	5.051	5.096	5.032	5.337	5.180
96	5.133	5.147	5.165	5.278	5.162
Ref. [5]			5.156		
$R/h = 5$					
Num. of elem.	T3-2LIM	ARS-T9	T3-U3	T3-LSC	T3-LSI
6	4.773	4.803	5.433	5.400	5.341
24	5.048	5.120	5.289	5.246	5.204
96	5.130	5.162	5.208	5.208	5.173
Ref. [5]			5.156		

Table 3.11: Central displacement w of the uniformly loaded clamped circular plate

$R/h = 50$						
Num. of elem.	T3-2LIM	ARS-T9	RDKTM	T3-U3	T3-LSC	T3-LSI
6	7712.9	10307	10307	4137.9	8572.4	8290.7
24	9234.7	9994.8	9982.4	8128.2	9630.8	9482.6
96	9644.2	9847.8	9851.7	9534.0	9778.2	9717.2
Ref. [5]			9783.5			
$R/h = 5$						
Num. of elem.	T3-2LIM	ARS-T9	RDKTM	T3-U3	T3-LSC	T3-LSI
6	9.4647	11.921	11.921	9.2888	9.9984	9.7403
24	11.006	11.702	11.687	10.990	11.258	11.169
96	11.415	11.594	11.598	11.399	11.472	11.464
Ref. [5]			11.551			

Table 3.12: Central moment M of the uniformly loaded clamped circular plate obtained in Gauss point that is closest to the centre of the plate

$R/h = 50$					
Num. of elem.	T3-2LIM	ARS-T9	T3-U3	T3-LSC	T3-LSI
6	1.317	1.814	1.054	1.872	2.099
24	1.841	2.038	1.861	1.916	1.975
96	1.987	2.039	2.021	2.032	2.017
Ref. [5]			2.031		
$R/h = 5$					
Num. of elem.	T3-2LIM	ARS-T9	T3-U3	T3-LSC	T3-LSI
6	1.342	1.950	2.016	1.967	2.000
24	1.842	2.064	2.087	1.912	2.003
96	1.985	2.054	2.064	2.018	2.028
Ref. [5]			2.031		

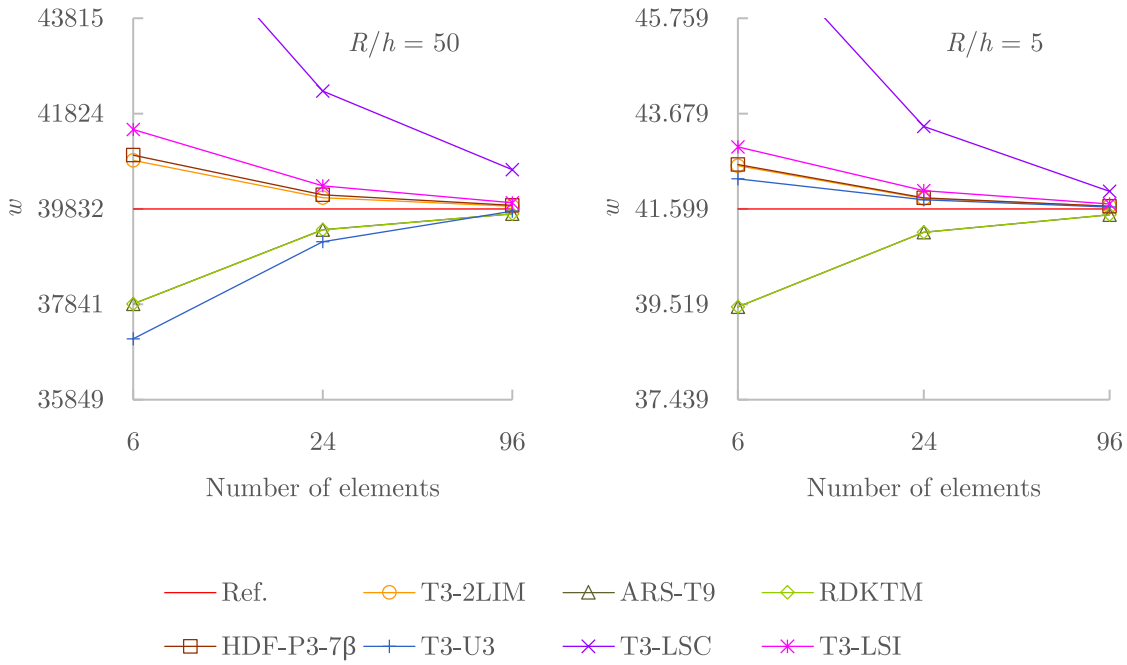

Figure 3.11: Central displacement w of the uniformly loaded simply supported circular plate

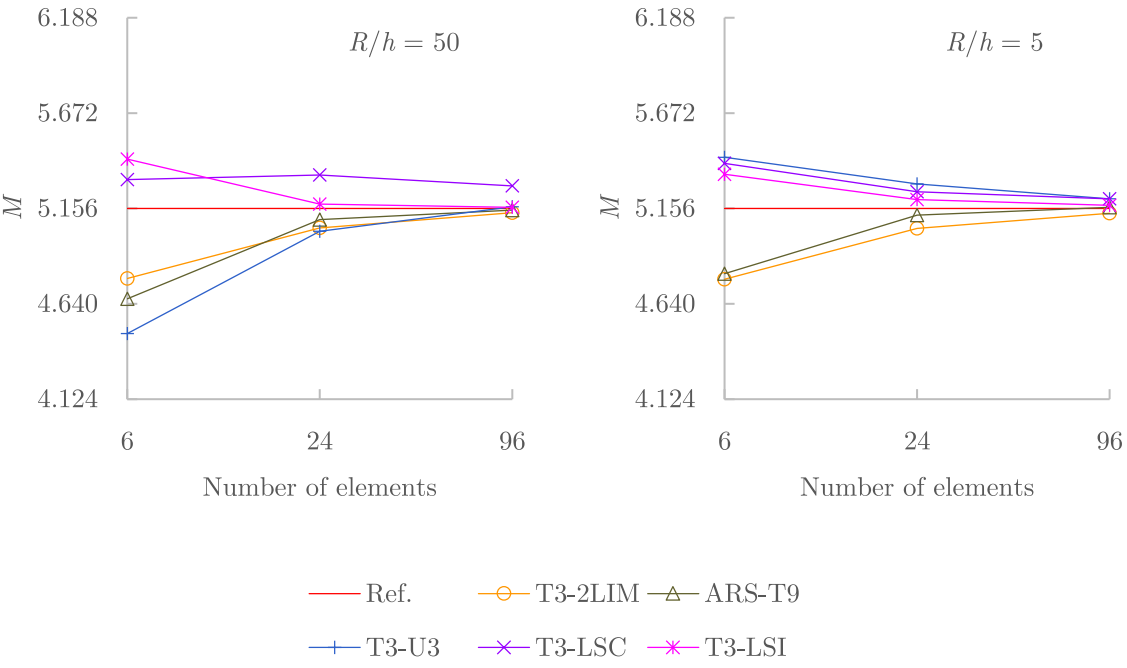

Figure 3.12: Central moment M of the uniformly loaded simply supported circular plate obtained in Gauss point that is closest to the centre of the plate

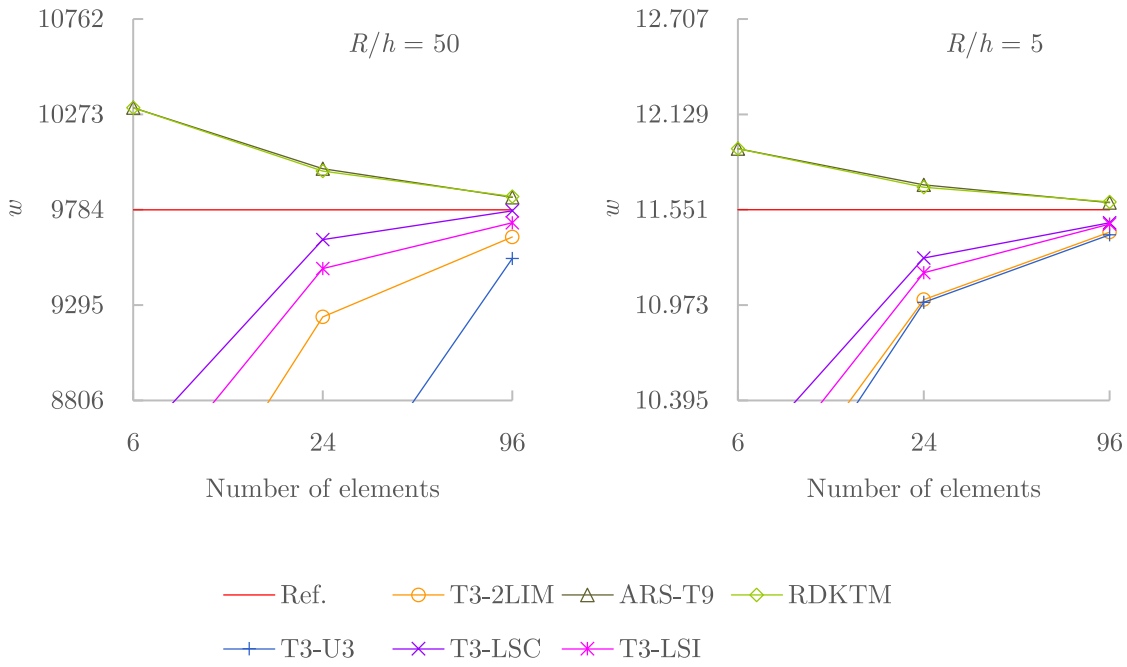

Figure 3.13: Central displacement w of the uniformly loaded clamped circular plate

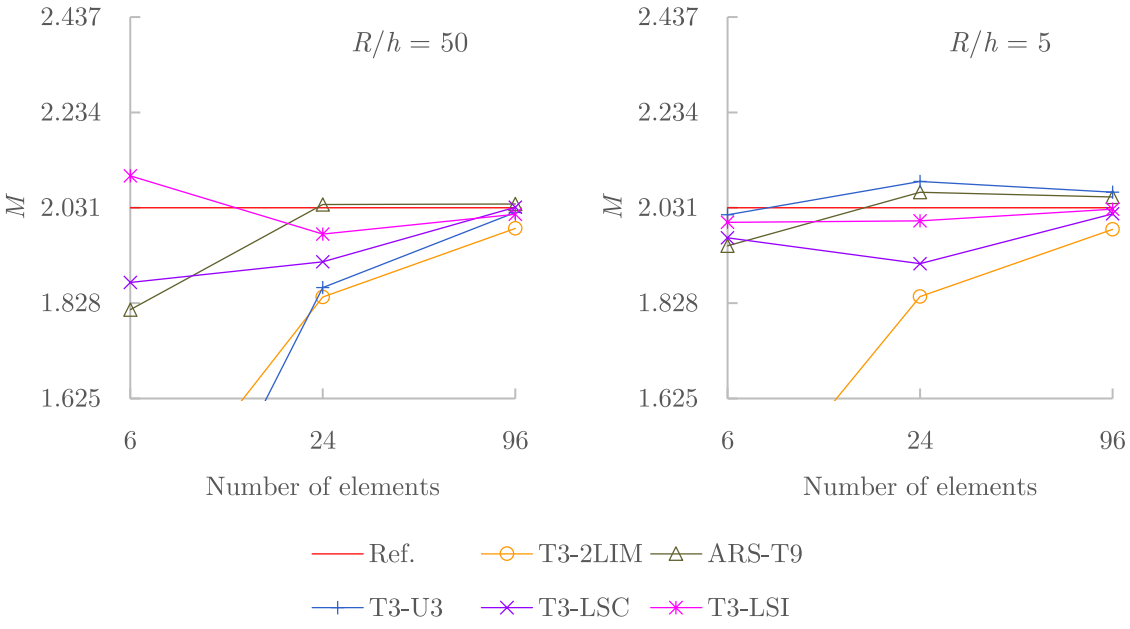

Figure 3.14: Central moment M of the uniformly loaded clamped circular plate obtained in Gauss point that is closest to the centre of the plate

3.5.4 Razzaque's skew plate

Razzaque's skew plate [45] is another frequently analysed benchmark problem, shaped as a parallelogram with an angle of 60° and two opposite edges as simply supported, as shown in Fig. 3.15. Like the previous problems, it is uniformly loaded ($q = 1$) and has the same plate properties ($E = 10.92$, $\nu = 0.3$ and $k = 5/6$). However, the whole plate is now discretised.

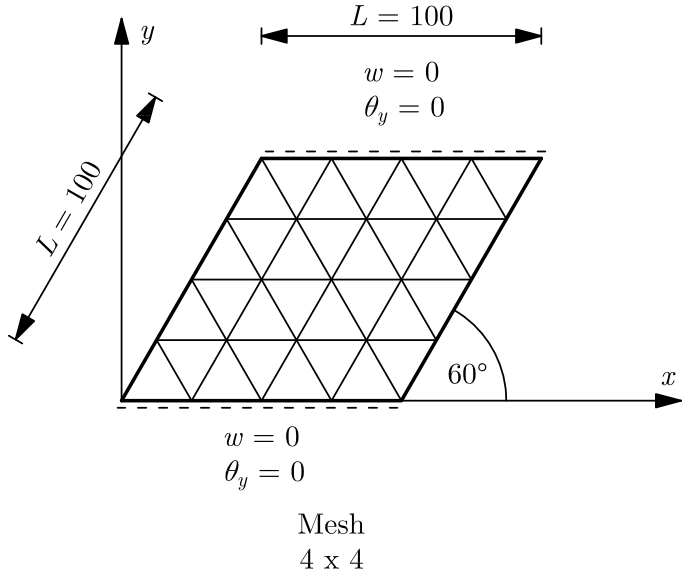

Figure 3.15: Razzaque's skew plate model

The presented elements T3-LSC and T3-LSI perform quite well in this numerical example, as it can be observed in Tables 3.13-3.14 or in Figs. 3.16-3.17. It is interesting to note that the T3-U3 element does not show its susceptibility to the shear locking phenomenon on this very thin plate example.

Table 3.13: Normalised central displacement $w/(10^{-2}\, q\, L^4/D)$ of the uniformly loaded Razzaque's skew plate

$L/h = 1000$							
Mesh	T3-2LIM	ARS-T9	RDKTM	HDF-P3-7β	T3-U3	T3-LSC	T3-LSI
2 x 2	0.78308	0.63823		0.71902	0.58594	0.84652	0.80436
4 x 4	0.79452	0.75095	0.7527	0.77353	0.69535	0.80311	0.79439
8 x 8	0.79434	0.78006	0.7822	0.78648	0.75635	0.79361	0.79351
16 x 16	0.79316	0.78805		0.78981	0.78587	0.79172	0.79281
32 x 32	0.79222	0.79020			0.78999	0.79127	0.79211
64 x 64	0.79166	0.79079			0.79077	0.79113	0.79164
Ref. [45]				0.7945			

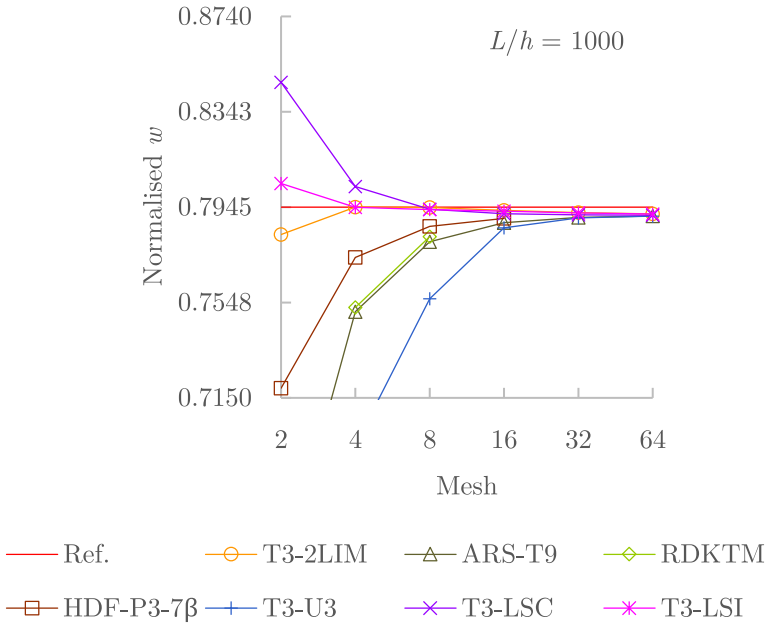

Figure 3.16: Normalised central displacement $w/(10^{-2}\,q\,L^4/D)$ of the uniformly loaded Razzaque's skew plate

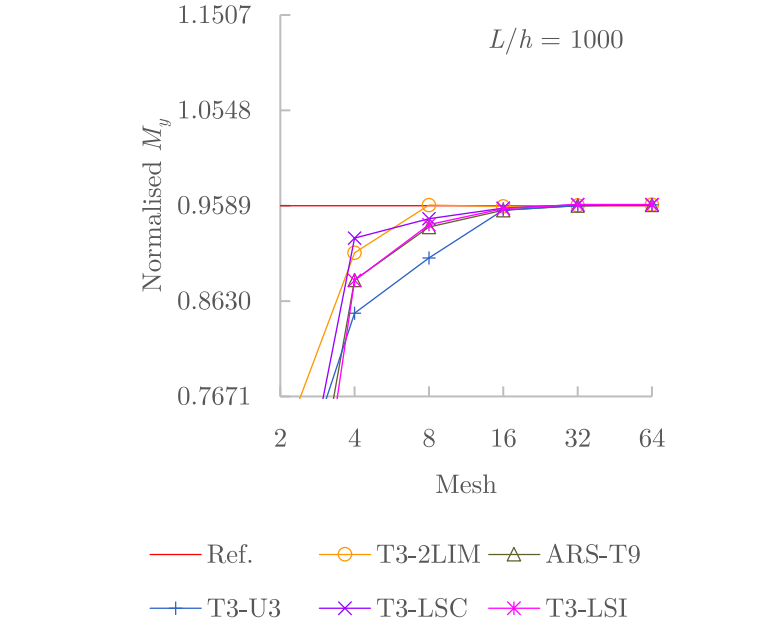

Figure 3.17: Normalised moment $M_y/(10^{-1}\,q\,L^2)$ of the uniformly loaded Razzaque's skew plate obtained in Gauss point that is closest to the centre of the plate

Table 3.14: Normalised moment $M_y/(10^{-1}\,q\,L^2)$ of the uniformly loaded Razzaque's skew plate obtained in Gauss point that is closest to the centre of the plate

$L/h = 1000$					
Mesh	T3-2LIM	ARS-T9	T3-U3	T3-LSC	T3-LSI
2 x 2	0.7129	0.4636	0.6249	0.5468	0.3771
4 x 4	0.9116	0.8842	0.8508	0.9263	0.8839
8 x 8	0.9595	0.9375	0.9064	0.9459	0.9399
16 x 16	0.9583	0.9544	0.9545	0.9565	0.9560
32 x 32	0.9592	0.9590	0.9589	0.9600	0.9602
64 x 64	0.9600	0.9596	0.9598	0.9598	0.9601
Ref. [45]			0.9589		

3.5.5 Morley's skew plate

Another skew plate example known as the Morley's skew plate [46], is analysed as well. It has a rather small acute angle of only 30° and it is simply supported on all edges, as shown in Fig. 3.18. Like the Razzaque's skew plate, it is modelled as a whole plate and like in all previous examples, it is uniformly loaded ($q = 1$) and has the same plate properties ($E = 10.92$, $\nu = 0.3$ and $k = 5/6$).

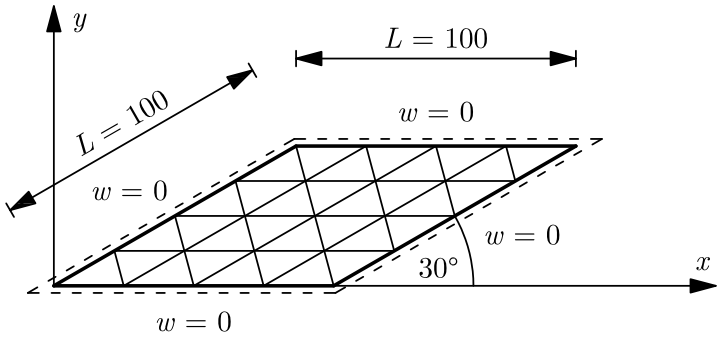

Mesh
4 x 4

Figure 3.18: Morley's skew plate model

Due to the nature of the problem, theoretically infinite principal moments occur in the obtuse corners of the plate, one having a positive and the other having a negative sign. Such unique property is quite demanding for the finite element verification. Tables 3.15-3.16 or Figs. 3.19-3.20 show that all elements, except the T3-U3 element, have fairly similar performance. They all have a softer response on coarse meshes, including the T3-U3 element even for the very thin plate case. This behaviour is likely due to the high skewness and the inability of the correct model description with such coarse meshes. Nevertheless, the T3-LSI element exhibits very good ability to capture moments overall.

Table 3.15: Normalised central displacement $w/(10^{-3}\,q\,L^4/D)$ of the uniformly loaded Morley's skew plate

$L/h = 1000$							
Mesh	T3-2LIM	ARS-T9	RDKTM	HDF-P3-7β	T3-U3	T3-LSC	T3-LSI
2 x 2	0.63508	0.62584		0.59050	0.43048	0.86650	0.73202
4 x 4	0.45724	0.45272	0.453	0.45300	0.38897	0.46813	0.47486
8 x 8	0.42922	0.42421	0.424	0.42220	0.37806	0.42991	0.43439
16 x 16	0.42188	0.41929	0.419	0.41718	0.39228	0.41981	0.42380
32 x 32	0.41816	0.41658	0.417		0.40262	0.41604	0.41911
64 x 64	0.41572	0.41459			0.40788	0.41394	0.41629
Ref. [4]				0.408			
$L/h = 100$							
Mesh	T3-2LIM	ARS-T9	RDKTM	HDF-P3-7β	T3-U3	T3-LSC	T3-LSI
2 x 2	0.63591	0.62671			0.44345	0.86732	0.73292
4 x 4	0.45819	0.45366	0.454		0.42591	0.46898	0.47582
8 x 8	0.43037	0.42525	0.425		0.41537	0.43084	0.43550
16 x 16	0.42382	0.42071	0.421		0.41634	0.42117	0.42551
32 x 32	0.42183	0.41921	0.419		0.41756	0.41863	0.42232
64 x 64	0.42218	0.42022			0.41945	0.41945	0.42215
Ref. [4]				0.423			

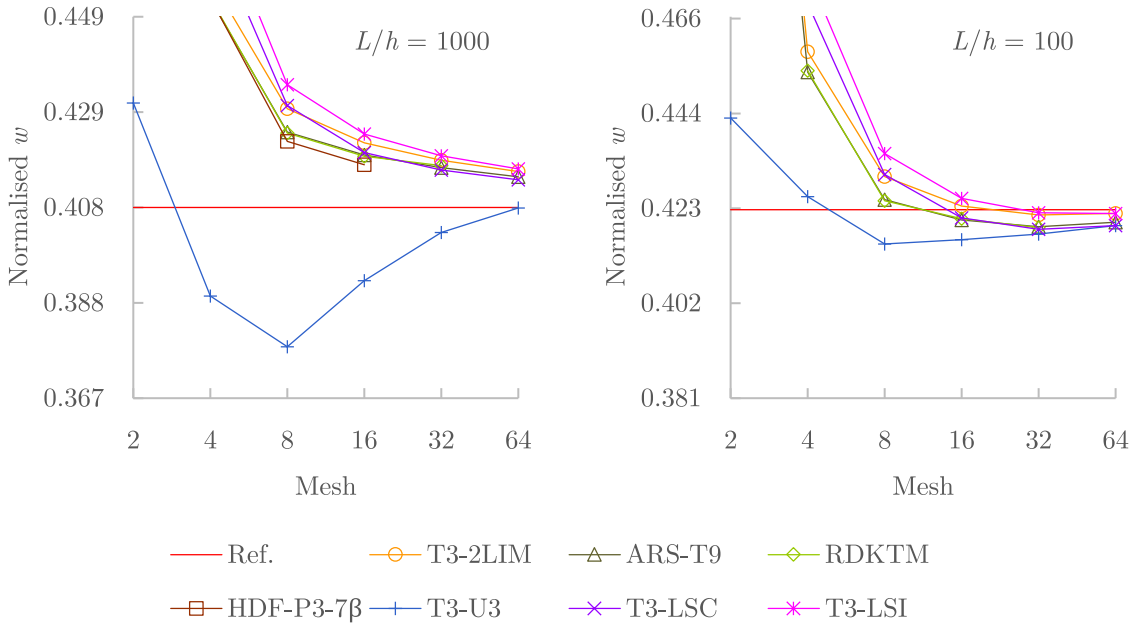

Figure 3.19: Normalised central displacement $w/(10^{-3}\,q\,L^4/D)$ of the uniformly loaded Morley's skew plate

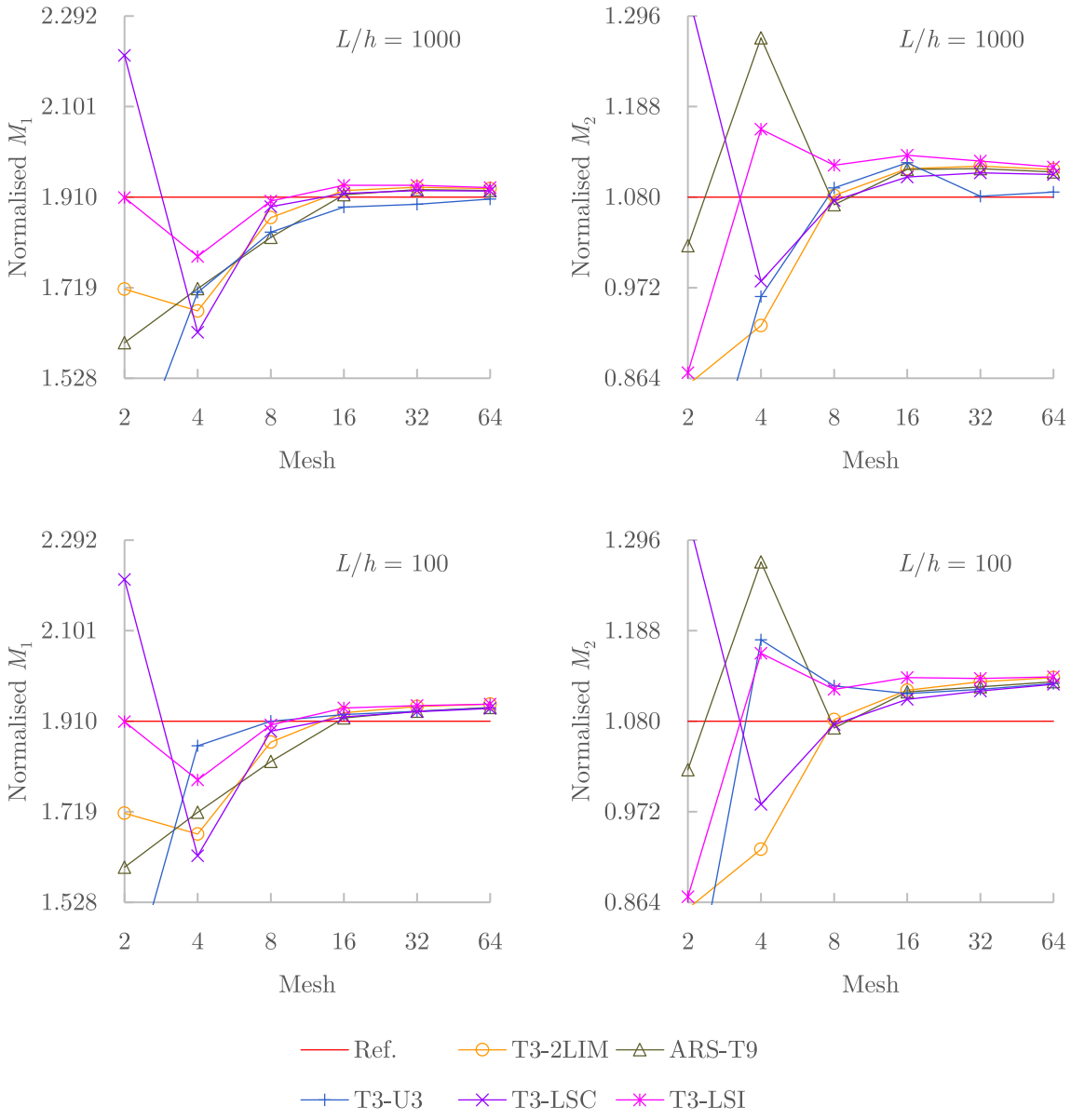

Figure 3.20: Normalised principal moments $M_{1,2}/(10^{-2}\,q\,L^2)$ of the uniformly loaded Morley's skew plate obtained in Gauss point that is closest to the centre of the plate

Table 3.16: Normalised principal moments $M_{1,2}/(10^{-2}\,q\,L^2)$ of the uniformly loaded Morley's skew plate obtained in Gauss point that is closest to the centre of the plate

$L/h = 1000$										
	T3-2LIM		ARS-T9		T3-U3		T3-LSC		T3-LSI	
Mesh	M_1	M_2	M_1	M_2	M_1	M_2	M_1	M_2	M_1	M_2
2 x 2	1.716	0.856	1.603	1.022	1.301	0.655	2.209	1.324	1.909	0.871
4 x 4	1.670	0.927	1.717	1.270	1.709	0.962	1.625	0.980	1.785	1.161
8 x 8	1.867	1.082	1.825	1.071	1.836	1.091	1.890	1.076	1.902	1.118
16 x 16	1.924	1.114	1.915	1.113	1.889	1.121	1.918	1.104	1.935	1.130
32 x 32	1.931	1.117	1.926	1.114	1.895	1.081	1.924	1.109	1.935	1.123
64 x 64	1.928	1.113	1.924	1.110	1.906	1.086	1.923	1.107	1.930	1.116
Ref. [4]	1.91 / 1.08									
$L/h = 100$										
	T3-2LIM		ARS-T9		T3-U3		T3-LSC		T3-LSI	
Mesh	M_1	M_2	M_1	M_2	M_1	M_2	M_1	M_2	M_1	M_2
2 x 2	1.716	0.856	1.602	1.022	1.309	0.708	2.209	1.324	1.909	0.871
4 x 4	1.672	0.927	1.718	1.270	1.858	1.177	1.626	0.981	1.786	1.161
8 x 8	1.866	1.082	1.825	1.072	1.910	1.122	1.889	1.076	1.902	1.118
16 x 16	1.928	1.117	1.917	1.115	1.924	1.113	1.919	1.106	1.938	1.132
32 x 32	1.941	1.127	1.931	1.121	1.931	1.118	1.930	1.116	1.943	1.131
64 x 64	1.946	1.132	1.939	1.127	1.938	1.125	1.937	1.124	1.946	1.133
Ref. [4]	1.91 / 1.08									

3.6 Conclusions

Three new three-node Mindlin plate finite elements T3-U3, T3-LSC and T3-LSI are presented, all based on the two-node Timoshenko beam finite element with problem-dependent cubic linked interpolation. The T3-U3 element is developed using a classical finite element displacement-based procedure by interpolating transverse displacement field and rotational fields, which are obtained by generalising the Timoshenko beam element interpolations. The T3-LSC and T3-LSI elements are developed by generalising the constant shear strain expression of the Timoshenko beam element along each of the element side, which results in linear shear strain fields in global coordinate directions. For the T3-LSC element, the rotational fields are derived in a way that the whole finite element formulation is kinematically consistent in every point inside the finite element domain, whereas for the T3-LSI element, the rotational fields are interpolated independently, i.e., the rotational fields are kinematically independent to the rest of the finite element formulation, and they are assumed in a way that should increase the element's convergence properties, in addition to its performance.

The T3-U3 and T3-LSI elements pass the patch test for the constant bending state regardless of the element size, so that the convergence towards a solution can be reliably expected in all cases. That is also the case with the T3-LSC element, which passes the constant bending patch test only when the size of the elements become infinitesimal, even though the element formulation

itself is capable of providing the exact stress resultants regardless of the element size. However, the very thin square plate problems have shown that the T3-LSC element does not yield accurate moments on very dense meshes, even though it is convergent in terms of the displacement values. Notwithstanding, the results from the other plate problems show its good convergence properties for both displacement and moment values.

The T3-U3 element has shown its susceptibility to the shear locking phenomenon, especially on very thin square plate problems with coarse meshes, but interestingly, not really on other plate problems. Its shear locking behaviour rapidly fades away with the finite element mesh refinement. The performance of the T3-U3 element improves as the plate gets thicker. For thick plate cases, the T3-U3 element is very effective and among the best performing. In contrast to the T3-LSC and T3-LSI elements, it is not as computationally efficient due to the static condensation procedure of the internal degree of freedom and its higher-order shear strain terms which require higher-order numerical integration.

On the other hand, the T3-LSC and T3-LSI elements are completely free of shear locking, which makes them suitable for the analysis of very thin to thick plate cases. More to the point, the T3-LSC element is exhibiting softer response in most (very) thin plate problems. Performance of these two elements is not changing much with different thickness to span ratios, i.e., whether the plate is (very) thin or thick. Additionally, they are computationally efficient due to their direct shear strain fields definitions.

Among the presented elements, the T3-LSI appears to be *the best* for practical application as it has not shown any weaknesses in the benchmark problems and because it is: capable of passing the constant bending patch test regardless of the element size, shear locking free, computationally efficient, high performing and effective in all cases.

The T3-U3 and T3-LSC elements are also usable for practical application, but with some caution. The T3-U3 element should be avoided on (very) thin plate problems with coarse meshes due to its susceptibility to the shear locking phenomenon. The T3-LSC element does not always yield accurate moments when the plate is (very) thin. This is possibly connected to its inability to pass the constant bending patch test regardless of the element size. Other than that, these elements perform well and can also be reliably used in all moderately thick to thick plate cases nonetheless.

As it can be deduced from the numerical results, the performance of the presented finite elements is comparable to the other existing finite elements used in the comparison, which is

somewhat expected as there are similarities in the approach and the formulation. The T3-LSI element has all the necessary requirements to be considered as a strong candidate for a default plate finite element inside a finite element analysis software. With respect to the T3-2LIM element from FEAP, the T3-LSI element has a simpler formulation and is computationally more efficient. Performance wise, these elements are quite similar overall and one does not have an apparent advantage over the other.

The presented finite elements are considered later in Chapter 5 to make the out-of-plane Mindlin plate bending part in a flat shell finite element formulation.

Chapter 4

Membrane finite elements with rotational degrees of freedom

4.1 Rotational degrees of freedom

A three-node membrane finite element with its nodal degrees of freedom, including the rotational ones commonly referred to as drilling rotations, is shown in Fig. 4.1. According to the classical theory of plane elasticity, rotations are not independent of displacements. By considering a differential element after translation and rotation in its plane, as shown in Fig. 4.2, rotation of the element can be obtained as

$$\theta_z = \frac{\partial v}{\partial x} = -\frac{\partial u}{\partial y}\,. \tag{4.1}$$

Consequently, rotation of a single point inside a deformable 2D body follows by averaging as

$$\theta_z(x,y) = \frac{1}{2}\left(\frac{\partial v}{\partial x} - \frac{\partial u}{\partial y}\right). \tag{4.2}$$

Thus, introduction of rotations as additional degrees of freedom in a finite element formulation conflicts the theory. However, it does not conflict the finite element concept, moreover, it has proven to be advantageous in the finite element application. Furthermore, the rotational degrees of freedom do not even need to be or represent real rotations. In such case, the finite element application is limited to plane elasticity problems and moment loads are not allowed. However, higher element performance is generally attained, e.g., the elements presented in Refs. [26,32,33], possibly due to the lack of constraints that are linked to those rotational degrees of freedom [e.g. Eq. (4.2)].

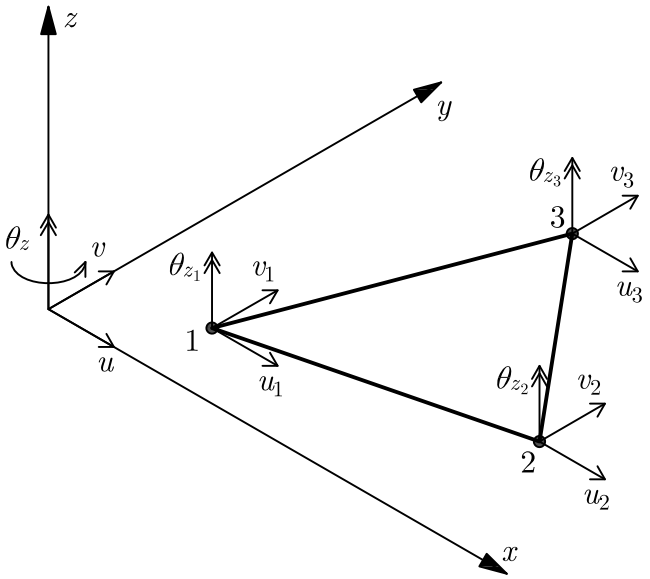

Figure 4.1: Degrees of freedom of a three-node membrane plate finite element with drilling rotations

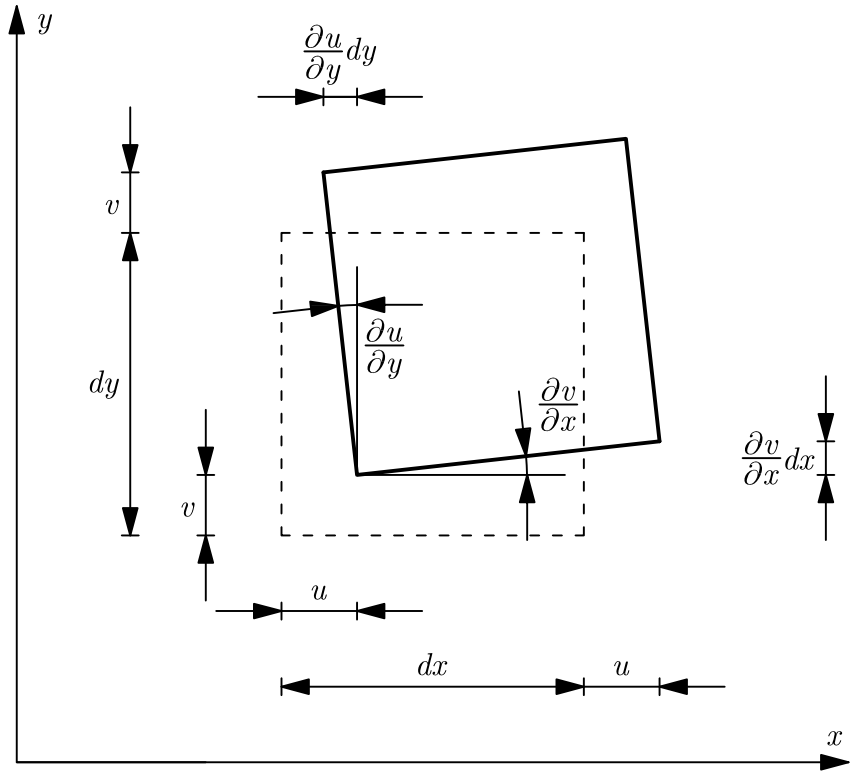

Figure 4.2: Differential 2D element after translation and rotation

As mentioned previously in Chapter 1, membrane finite elements with true rotations possess some significant advantages over the ones that do not. Essentially, the only practical advantage of not having true rotations as rotational degrees of freedom in a finite element formulation is a potential increase in efficiency. With that, new membrane finite elements are developed here with the rotational degrees of freedom being true rotations.

4.2 Displacement interpolations with true rotations

The displacement fields (u and v) for the new elements are quadratic polynomials and can be written as

$$\begin{aligned} u = {} & \xi_1\, u_1 + \xi_2\, u_2 + \xi_3\, u_3 \\ & + \xi_1\, \xi_2\, c_{qu_3} + \xi_2\, \xi_3\, c_{qu_1} + \xi_3\, \xi_1\, c_{qu_2} \end{aligned} \tag{4.3}$$

and

$$\begin{aligned} v = {} & \xi_1\, v_1 + \xi_2\, v_2 + \xi_3\, v_3 \\ & + \xi_1\, \xi_2\, c_{qv_3} + \xi_2\, \xi_3\, c_{qv_1} + \xi_3\, \xi_1\, c_{qv_2}\,, \end{aligned} \tag{4.4}$$

where c_{qu_i} and c_{qv_i} are the quadratic polynomial coefficients which include nodal rotations (*linked interpolation*), and are determined later in the Sections 4.3 and 4.4. The true rotational field (θ_z) can be derived now by following Eq. (4.2) as

$$\begin{aligned} \theta_z = \theta_{z_e} + \frac{1}{4\,A}[& (\xi_2\, b_1 + \xi_1\, b_2)\, c_{qv_3} + (\xi_3\, b_2 + \xi_2\, b_3)\, c_{qv_1} + (\xi_1\, b_3 + \xi_3\, b_1)\, c_{qv_2} \\ & - (\xi_2\, a_1 + \xi_1\, a_2)\, c_{qu_3} - (\xi_3\, a_2 + \xi_2\, a_3)\, c_{qu_1} - (\xi_1\, a_3 + \xi_3\, a_1)\, c_{qu_2}] \end{aligned} \tag{4.5}$$

in which

$$\theta_{z_e} = \frac{1}{4\,A}(v_1\, b_1 + v_2\, b_2 + v_3\, b_3 - u_1\, a_1 - u_2\, a_2 - u_3\, a_3) \tag{4.6}$$

is the element rotation. Since the rotational field follows as a linear polynomial, it can also be written in terms of its nodal parameters (rotations) as

$$\theta_z = \xi_1\, \theta_{z_1} + \xi_2\, \theta_{z_2} + \xi_3\, \theta_{z_3}\,. \tag{4.7}$$

With Eqs. (4.5) and (4.7) being equivalent, the relation between c_{qu_i} and c_{qv_i}, and nodal displacements and rotations can be established, e.g., at the element nodes, which yields the following

three equations:

$$\theta_{z_1} = \theta_{z_e} + \frac{1}{4\,A}(c_{qv_3}\,b_2 + c_{qv_2}\,b_3 - c_{qu_3}\,a_2 - c_{qu_2}\,a_3)\,, \tag{4.8}$$

$$\theta_{z_2} = \theta_{z_e} + \frac{1}{4\,A}(c_{qv_1}\,b_3 + c_{qv_3}\,b_1 - c_{qu_1}\,a_3 - c_{qu_3}\,a_1) \tag{4.9}$$

and

$$\theta_{z_3} = \theta_{z_e} + \frac{1}{4\,A}(c_{qv_2}\,b_1 + c_{qv_1}\,b_2 - c_{qu_2}\,a_1 - c_{qu_1}\,a_2)\,. \tag{4.10}$$

This provides three out of six equations used in the next section from which c_{qu_i} and c_{qv_i} are obtained, and ultimately secures that the displacement interpolations satisfy Eq. (4.2) in every point inside the element domain, which in turn ensures that the finite element analysis always yields true rotations[1]. The other three equations are determined by adopting certain strain assumptions, as described in the following section.

4.3 Assumed strain method

With the displacement fields assumed as quadratic polynomials [Eqs. (4.3) and (4.4)], strains can be derived by following Eq. (2.9) as

$$\begin{aligned}\varepsilon_x = \frac{1}{2\,A}[&u_1\,b_1 + u_2\,b_2 + u_3\,b_3 \\ &+ (\xi_2\,b_1 + \xi_1\,b_2)\,c_{qu_3} + (\xi_3\,b_2 + \xi_2\,b_3)\,c_{qu_1} + (\xi_1\,b_3 + \xi_3\,b_1)\,c_{qu_2}]\,,\end{aligned} \tag{4.11}$$

$$\begin{aligned}\varepsilon_y = \frac{1}{2\,A}[&v_1\,a_1 + v_2\,a_2 + v_3\,a_3 \\ &+ (\xi_2\,a_1 + \xi_1\,a_2)\,c_{qv_3} + (\xi_3\,a_2 + \xi_2\,a_3)\,c_{qv_1} + (\xi_1\,a_3 + \xi_3\,a_1)\,c_{qv_2}]\end{aligned} \tag{4.12}$$

and

$$\begin{aligned}\gamma_{xy} = \frac{1}{2\,A}[&v_1\,b_1 + v_2\,b_2 + v_3\,b_3 + u_1\,a_1 + u_2\,a_2 + u_3\,a_3 \\ &+ (\xi_2\,b_1 + \xi_1\,b_2)\,c_{qv_3} + (\xi_3\,b_2 + \xi_2\,b_3)\,c_{qv_1} + (\xi_1\,b_3 + \xi_3\,b_1)\,c_{qv_2} \\ &+ (\xi_2\,a_1 + \xi_1\,a_2)\,c_{qu_3} + (\xi_3\,a_2 + \xi_2\,a_3)\,c_{qu_1} + (\xi_1\,a_3 + \xi_3\,a_1)\,c_{qu_2}]\,.\end{aligned} \tag{4.13}$$

[1] Eq. (4.2) does not need to be satisfied in the entire element domain for the finite element analysis to yield true rotations. E.g., the finite element analysis also yields true rotations for the element presented by Allman in Ref. [28], in which Eq. (4.2) is satisfied only at the element nodes.

Strains in the element centroid ($\xi_1 = \xi_2 = \xi_3 = 1/3$) follow as

$$\varepsilon_{x_C} = \frac{1}{2\,A}\left(u_1\,b_1 + u_2\,b_2 + u_3\,b_3 - \frac{1}{3}\,c_{x_C}\right), \tag{4.14}$$

$$\varepsilon_{y_C} = \frac{1}{2\,A}\left(v_1\,a_1 + v_2\,a_2 + v_3\,a_3 - \frac{1}{3}\,c_{y_C}\right) \tag{4.15}$$

and

$$\gamma_{xy_C} = \frac{1}{2\,A}\left(v_1\,b_1 + v_2\,b_2 + v_3\,b_3 + u_1\,a_1 + u_2\,a_2 + u_3\,a_3 - \frac{1}{3}\,c_{xy_C}\right), \tag{4.16}$$

where

$$c_{x_C} = c_{qu_1}b_1 + c_{qu_2}b_2 + c_{qu_3}b_3\,, \tag{4.17}$$

$$c_{y_C} = c_{qv_1}a_1 + c_{qv_2}a_2 + c_{qv_3}a_3 \tag{4.18}$$

and

$$c_{xy_C} = c_{qv_1}b_1 + c_{qv_2}b_2 + c_{qv_3}b_3 + c_{qu_1}a_1 + c_{qu_2}a_2 + c_{qu_3}a_3\,. \tag{4.19}$$

The element presented by Allman in Ref. [26] has the following quadratic coefficients in the displacement fields:

$$c_{qu_i} = \frac{\theta_{z_j} - \theta_{z_k}}{2}\,b_i \tag{4.20}$$

and

$$c_{qv_i} = \frac{\theta_{z_j} - \theta_{z_k}}{2}\,a_i\,, \tag{4.21}$$

which is the standard *linked interpolation* form, and yields c_{x_C}, c_{y_C} and c_{xy_C} as

$$\begin{aligned} c_{x_C} &= c_{qu_1}b_1 + c_{qu_2}b_2 + c_{qu_3}b_3 \\ &= p\left(\frac{\theta_{z_2} - \theta_{z_3}}{2}\,{b_1}^2 + \frac{\theta_{z_3} - \theta_{z_1}}{2}\,{b_2}^2 + \frac{\theta_{z_1} - \theta_{z_2}}{2}\,{b_3}^2\right), \end{aligned} \tag{4.22}$$

$$\begin{aligned} c_{y_C} &= c_{qv_1}a_1 + c_{qv_2}a_2 + c_{qv_3}a_3 \\ &= p\left(\frac{\theta_{z_2} - \theta_{z_3}}{2}\,{a_1}^2 + \frac{\theta_{z_3} - \theta_{z_1}}{2}\,{a_2}^2 + \frac{\theta_{z_1} - \theta_{z_2}}{2}\,{a_3}^2\right) \end{aligned} \tag{4.23}$$

and

$$\begin{aligned} c_{xy_C} &= c_{qv_1}b_1 + c_{qv_2}b_2 + c_{qv_3}b_3 + c_{qu_1}a_1 + c_{qu_2}a_2 + c_{qu_3}a_3 \\ &= p\left[(\theta_{z_2} - \theta_{z_3})\,a_1\,b_1 + (\theta_{z_3} - \theta_{z_1})\,a_2\,b_2 + (\theta_{z_1} - \theta_{z_2})\,a_3\,b_3\right], \end{aligned} \tag{4.24}$$

in which $p = 1$. Given the element good performance, these equations are assumed for the new element as the other three equations from which c_{qu_i} and c_{qv_i} are obtained. Thus, by solving Eqs. (4.8)-(4.10) and (4.22)-(4.24) for c_{qu_i} and c_{qv_i}, the quadratic coefficients for the new element are obtained as

$$c_{qu_i} = (\theta_{z_j} - \theta_{z_k})\, b_i - (\theta_{z_i} - \theta_{z_e})\,(b_j - b_k) - \frac{1}{2}\, p\,[\theta_{z_k}\, b_j - \theta_{z_j}\, b_k - \theta_{z_i}(b_j - b_k)] \tag{4.25}$$

and

$$c_{qv_i} = (\theta_{z_j} - \theta_{z_k})\, a_i - (\theta_{z_i} - \theta_{z_e})\,(a_j - a_k) - \frac{1}{2}\, p\,[\theta_{z_k}\, a_j - \theta_{z_j}\, a_k - \theta_{z_i}(a_j - a_k)]\,. \tag{4.26}$$

Additionally, the value of p is adjusted for efficiency to the optimal value of $1.\dot{3}$ ($p = 4/3$). Lower or higher values of p result in a stiffer response, and the influence of p diminishes with the finite element mesh refinement.

Even though a displacement form is obtained for the new finite element presented here, it is named ACST (Assumed Centroidal Strain Triangle) since it is based on strain assumptions given in the element centroid.

4.4 Pure bending element

A three-node membrane finite element capable of achieving the exact response for an arbitrary pure bending problem is sought in this section. The motivation lies in the fact that such element would be of a major importance in the finite element analyses, and that it has not been found to date.

For an arbitrary pure bending state, the displacement fields are quadratic polynomials, and the rotational field follows as a linear polynomial, as assumed previously [Eqs. (4.3), (4.4) and (4.7)]. Appropriate quadratic coefficients in the displacement fields have been found as

$$c_{qu_i} = -\kappa_x\, b_i\, a_i + \kappa_y\, \frac{{b_i}^2 + \nu\, {a_i}^2}{2} \tag{4.27}$$

and

$$c_{qv_i} = \kappa_y\, a_i\, b_i - \kappa_x\, \frac{{a_i}^2 + \nu\, {b_i}^2}{2}\,, \tag{4.28}$$

where

$$\kappa_x = \frac{\partial \theta_z}{\partial x} = \frac{1}{2\,A}(\theta_{z_1}\,b_1 + \theta_{z_2}\,b_2 + \theta_{z_3}\,b_3) \tag{4.29}$$

and

$$\kappa_y = \frac{\partial \theta_z}{\partial y} = \frac{1}{2\,A}(\theta_{z_1}\,a_1 + \theta_{z_2}\,a_2 + \theta_{z_3}\,a_3) \tag{4.30}$$

are the element in-plane curvatures[2]. With that, an element capable of achieving the exact response for pure bending problems in which the principal axes coincide with the x and y axes only is obtained. On the other hand, its displacement interpolations do not satisfy Eq. (4.2), hence, values of true rotations are not to be expected in the finite element solution. By modifying c_{qu_i} and c_{qv_i} as

$$c_{qu_i} = -\kappa_x\,b_i\,a_i + \kappa_y\,\frac{{b_i}^2 + \nu\,{a_i}^2}{2} + o\,(b_j - b_k) \tag{4.31}$$

and

$$c_{qv_i} = \kappa_y\,a_i\,b_i - \kappa_x\,\frac{{a_i}^2 + \nu\,{b_i}^2}{2} + o\,(a_j - a_k)\,, \tag{4.32}$$

where

$$\begin{aligned} o = \theta_{z_e} &- \frac{\theta_{z_1} + \theta_{z_2} + \theta_{z_3}}{3} \\ &- \frac{1}{24\,A}[\kappa_x\,(b_1\,a_2\,a_3 + b_2\,a_3\,a_1 + b_3\,a_1\,a_2 - 3\,\nu\,b_1\,b_2\,b_3) \\ &\qquad + \kappa_y\,(a_1\,b_2\,b_3 + a_2\,b_3\,b_1 + a_3\,b_1\,b_2 - 3\,\nu\,a_1\,a_2\,a_3)]\,, \end{aligned} \tag{4.33}$$

Eq. (4.2) is now satisfied in every point inside the element domain[3], i.e., the finite element analysis will always yield true nodal rotations. Moreover, the introduction of o also ensures that the element is free of spurious zero-energy mode in all cases. Additionally, the element's pure bending capability is retained, and the element is thus named PBCT (Pure Bending Capable Triangle).

The displacement fields for both ACST and PBCT elements are nonconforming since the quadratic coefficients c_{qu_i} and c_{qv_i}, which are related to each finite element side, involve all nodal and geometric parameters of the corresponding element.

[2]Not in relation with the out-of-plane curvatures from Eq. (2.3).
[3]As are Eqs. (4.8)-(4.10).

4.5 Stiffness matrix

Strains [Eq. (2.9)] can be re-written as

$$\boldsymbol{\varepsilon} = \mathbf{B_m}\,\mathbf{u_m}\,, \tag{4.34}$$

in which $\mathbf{B_m}$ is a strain-displacement matrix and

$$\mathbf{u_m} = \left\{ u_1 \quad v_1 \quad \theta_{z_1} \quad u_2 \quad v_2 \quad \theta_{z_2} \quad u_3 \quad v_3 \quad \theta_{z_3} \right\}^{\mathrm{T}} \tag{4.35}$$

is a vector of unknown nodal degrees of freedom.

The finite element stiffness matrix is formed by considering the strain energy contribution and integrating over the element domain as

$$\mathbf{K_m}^e = \int_{A_e} \mathbf{B_m}^{\mathbf{T}}\,\mathbf{D_m}\,\mathbf{B_m}\,t\,dA\,, \tag{4.36}$$

where t is the element thickness.

4.6 Numerical examples

In this section, the presented elements ACST and PBCT are analysed on a variety of standard benchmark problems, and the results are compared to the elements presented by Allman in Refs. [26,28] and to the CST element [24]. These elements have been incorporated into FEAP, in which all numerical examples were performed.

4.6.1 Patch test

First numerical example is a patch test for a constant strain state. Functions for the displacement fields are given as

$$\begin{gathered} u = 0.008\,x + 0.004\,y \\ \text{and} \\ v = 0.003\,x + 0.006\,y. \end{gathered} \tag{4.37}$$

The rotational field follows as

$$\theta_z = \frac{1}{2}\left(\frac{\partial v}{\partial x} - \frac{\partial u}{\partial y}\right) = -0.0005\,. \tag{4.38}$$

The patch test model is defined with the arbitrary mesh shown in Fig. 4.3, which is identical to Fig. 3.4, but is reproduced here for clarity. The displacements and the rotations are given in the external nodes (1, 2, 7 and 8) and checked in the internal nodes (3, 4, 5 and 6). The plate properties are $E = 1500.0$, $\nu = 0.25$ and $t = 1.0$. The expected strains are $\varepsilon_x = 0.006$, $\varepsilon_y = 0.008$ and $\gamma_{xy} = 0.007$, and they are constant over the entire patch domain.

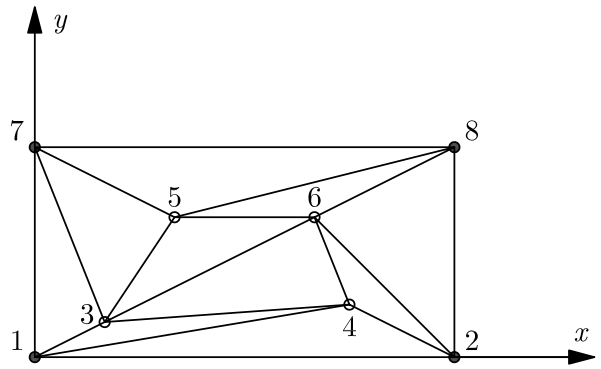

Node	x	y
1	0.00	0.00
2	0.24	0.00
3	0.04	0.02
4	0.18	0.03
5	0.08	0.08
6	0.16	0.08
7	0.00	0.12
8	0.24	0.12

Figure 4.3: Patch test mesh

The presented element ACST passes the patch test as the exact displacements and rotations are obtained in the internal nodes, as shown in Table 4.1, in addition to the exact strains which are obtained in the integration points. The PBCT element does not pass the patch test on the finite element mesh defined in Fig. 4.3. However, as the mesh gets denser, convergence to the exact results is achieved, and when the size of the elements become infinitesimal, the patch test is passed. If the exact transverse displacements and the rotations are given in all nodes, the PBCT element would yield the exact strains regardless of the element size.

The presented elements have a correct rank as only three eigenvalues corresponding to the rigid body modes, are equal to zero, i.e., the presented elements have no spurious zero-energy modes. Table 4.2 shows eigenvalues only for the element enclosed by nodes 3, 4 and 6.

Table 4.1: Constant strain patch test results

	PBCT			ACST / Exact		
Node	u	v	θ_z	u	v	θ_z
3	3.7884E-04	2.5700E-04	-1.0294E-03	4.0000E-04	2.4000E-04	-5.0000E-04
4	1.5941E-03	7.2706E-04	8.7722E-04	1.5600E-03	7.2000E-04	-5.0000E-04
5	9.3982E-04	6.7799E-04	1.3506E-03	9.6000E-04	7.2000E-04	-5.0000E-04
6	1.5967E-03	9.7845E-04	-3.0637E-04	1.6000E-03	9.6000E-04	-5.0000E-04
		Strain energy			Strain energy	
		3.20376E-03			3.28032E-03	

Table 4.2: Eigenvalues of the membrane element enclosed by nodes 3, 4 and 6

Element	1 7	2 8	3 9	4	5	6
ACST	6.5869E+03 8.9613E-13	4.0721E+03 -4.2283E-13	5.2744E+02 -1.3098E-14	4.4248E+02	1.8641E+00	8.7888E-02
PBCT	6.5876E+03 8.8380E-13	4.0737E+03 2.5063E-13	5.2742E+02 7.6827E-15	4.4245E+02	3.0000E+00	8.0625E-02

4.6.2 Pure bending of a simply supported beam

A simply supported beam subjected to a unit pure bending load is analysed next. Properties of the membrane element describing the beam in its loading plane are $E = 100.0$, $\nu = 0.0$ and $t = 1.0$. Two different finite element meshes are considered, one being regular (at least two element sides are mutually orthogonal, and parallel to the beam edges), and the other quite distorted, as shown in Fig. 4.4. The exact solution in point A is $u_A = -0.3$, $v_A = 1.5$ and $\theta_{z_A} = 0.0$.

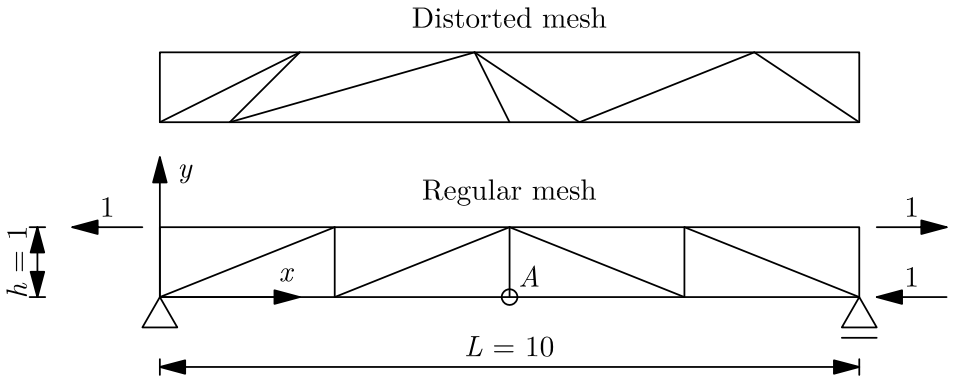

Figure 4.4: A simply supported beam model under pure bending

Table 4.3 shows that the PBCT element is capable of reproducing the exact response for this problem[4], regardless of the finite element mesh. Moreover, this is also the case for any value of Poisson's ratio ranging from -1.0 to 0.5. However, if the beam edges do not coincide with the coordinate axes x and y, the PBCT element would not yield the exact results.

Regarding the beam problem itself, the results from the CST element show how demanding it is to represent a pure bending state on such coarse meshes (Fig. 4.4). With that in mind, decent performance of the ACST element can be observed, which is better than the one from Ref. [28] and almost as good as the one from Ref. [26].

[4]Not only in the point A, but in every point inside the beam domain.

Table 4.3: Results for the simply supported beam subjected to the pure bending load in the point A

Regular mesh						
	CST	Allman [26]	Allman [28]	ACST	PBCT	Exact
u_A	-0.02497	-0.13627	-0.05130	-0.09091	-0.30000	-0.3
v_A	0.12245	0.67677	0.25670	0.44919	1.50000	1.5
θ_{z_A}			0.00000	0.00000	0.00000	0.0
Distorted mesh						
	CST	Allman [26]	Allman [28]	ACST	PBCT	Exact
u_A	-0.01765	-0.10216	-0.03819	-0.09540	-0.30000	-0.3
v_A	0.05587	0.55261	0.17470	0.36774	1.50000	1.5
θ_{z_A}			0.00288	0.00177	0.00000	0.0

4.6.3 Pure bending of a cantilever beam

An additional pure bending problem is analysed here for the purpose of the PBCT element verification. This time a cantilever beam under a unit pure bending load is considered in multiple configurations depending on the angle α, as shown in Fig. 4.5. The element properties are $E = 150.0$, $\nu = 0.0$ and $t = 1.0$. The exact transverse displacement in point A is 1.0.

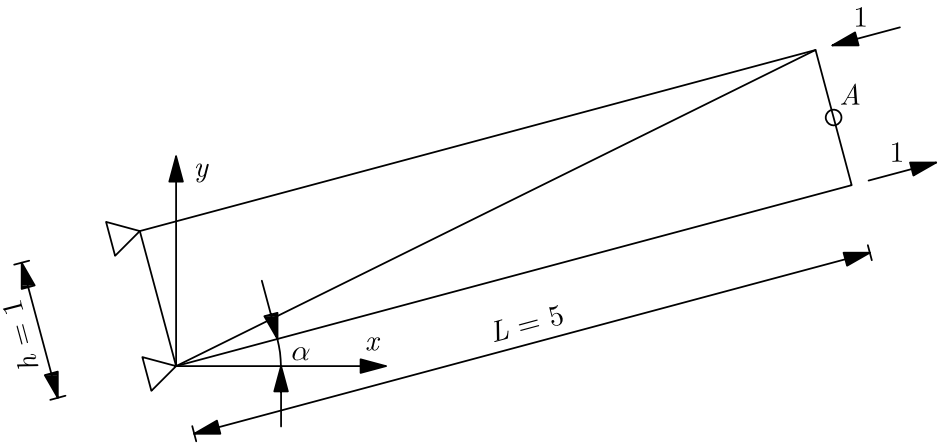

Figure 4.5: A cantilever beam model under pure bending rotated by α

Fig. 4.6 shows that the PBCT element, unlike the other elements, yields different results with respect to α. If the beam edges coincide with the coordinate axes x and y, the PBCT element yields exact results, and as the beam rotates from that position, the error in the result increases up to its maximum value at $\alpha = \pi/4$. The maximum error value is similar to the error values of other elements. Unfortunately, the behaviour of the PBCT element in this numerical example indicates that the element formulation is not invariant, i.e., it depends on how the model is defined with respect to the coordinate axes.

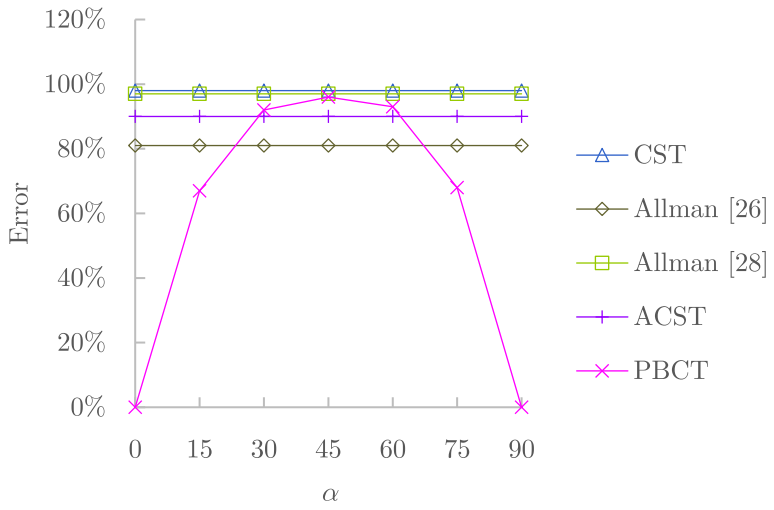

Figure 4.6: Error in the transverse displacement in point A

4.6.4 Timoshenko cantilever beam

Timoshenko cantilever beam is the next beam problem analysed here, with the element properties being $E = 30000.0$, $\nu = 0.25$ and $t = 1.0$. The beam is loaded at its end by a parabolically distributed shear force $P = 40$. Like in the previous numerical example, both regular and distorted meshes are considered, as shown in Fig. 4.7.

This beam problem was first described in Ref. [10], for which an analytical solution exist and can be given in terms of displacements as

$$u = \frac{P}{24\,E\,I}\left[12\,(x-2\,L)\,x-(2+\nu)(4\,y^2-h^2)\right]y$$

and (4.39)

$$v = \frac{P}{24\,E\,I}\left[-4\,(x-3\,L)\,x^2+(4+5\,\nu)\,h^2\,x-12\,(x-L)\,\nu\,y^2\right],$$

where

$$I = \frac{t\,h^3}{12}\,. \tag{4.40}$$

The rotational field follows as

$$\theta_z = \frac{1}{2}\left(\frac{\partial v}{\partial x}-\frac{\partial u}{\partial y}\right) = \frac{P}{24\,E\,I}\left[-12\,(x-2\,L)\,x+12\,y^2+(1+2\,\nu)\,h^2\right]. \tag{4.41}$$

Boundary conditions are for the clamped beam end defined as prescribed displacements, which are obtained from these equations (rotations are not prescribed, but kept free). Analogously, exact solution in the point A can be obtained as $u_A = 0.0$, $v_A = 0.355\dot{3}$ and $\theta_{z_A} = 0.01075$.

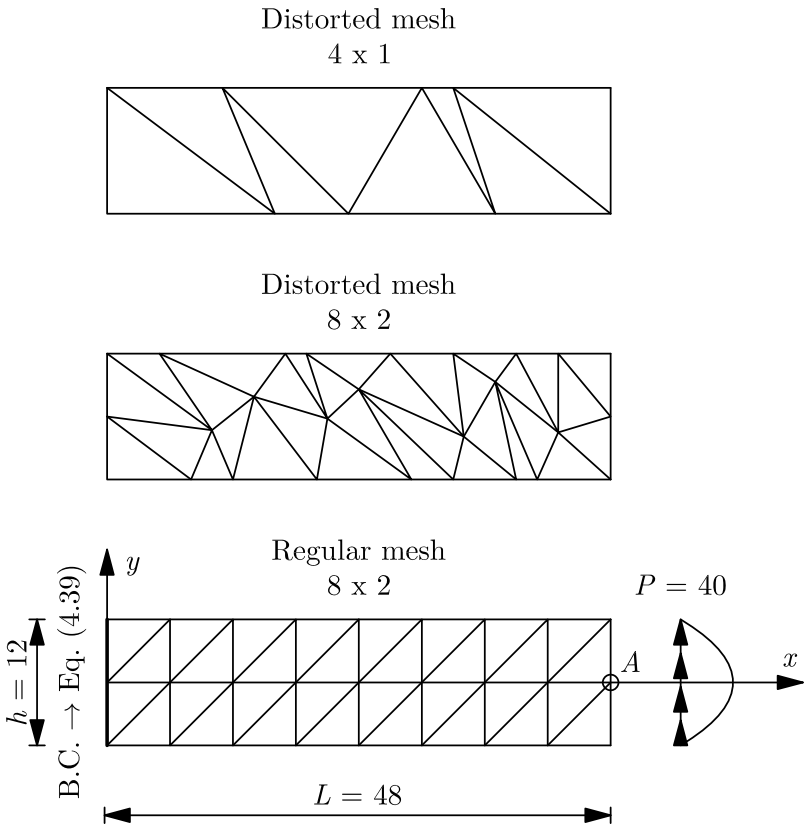

Figure 4.7: Timoshenko cantilever beam model

The results shown numerically in Tables 4.4 and 4.5, and graphically in Fig. 4.8 point out the exceptional performance of the PBCT element. The ACST element performs well, almost identically to the element presented in Ref. [26], and better than the one presented in Ref. [28]. Additionally, mesh distortions are not considerably affecting the elements in terms of performance, but the PBCT element is proving to be the most resistant to it.

Table 4.4: Vertical displacement v_A of the Timoshenko cantilever beam

Regular meshes					
Mesh	CST	Allman [26]	Allman [28]	ACST	PBCT
4 x 1	0.09265	0.27282	0.16801	0.26963	0.35133
8 x 2	0.19932	0.34007	0.27781	0.33395	0.36349
16 x 4	0.29550	0.35466	0.33219	0.34927	0.35741
32 x 8	0.33804	0.35608	0.34929	0.35373	0.35579
64 x 16	0.35083	0.35577	0.35382	0.35492	0.35543
Exact			$0.35\dot{5}\dot{3}$		
Distorted meshes					
Mesh	CST	Allman [26]	Allman [28]	ACST	PBCT
4 x 1	0.08149	0.24312	0.14777	0.24527	0.34847
8 x 2	0.18972	0.31884	0.25721	0.30924	0.35803
Exact			$0.35\dot{5}\dot{3}$		

Table 4.5: Rotation θ_{z_A} of the Timoshenko cantilever beam

Regular meshes			
Mesh	Allman [28]	ACST	PBCT
4 x 1	0.005057	0.008188	0.010806
8 x 2	0.008381	0.010061	0.010971
16 x 4	0.010044	0.010552	0.010811
32 x 8	0.010567	0.010697	0.010763
64 x 16	0.010704	0.010736	0.010753
Exact		0.01075	
Distorted meshes			
Mesh	Allman [28]	ACST	PBCT
4 x 1	0.004541	0.007460	0.010802
8 x 2	0.007852	0.009297	0.010980
Exact		0.01075	

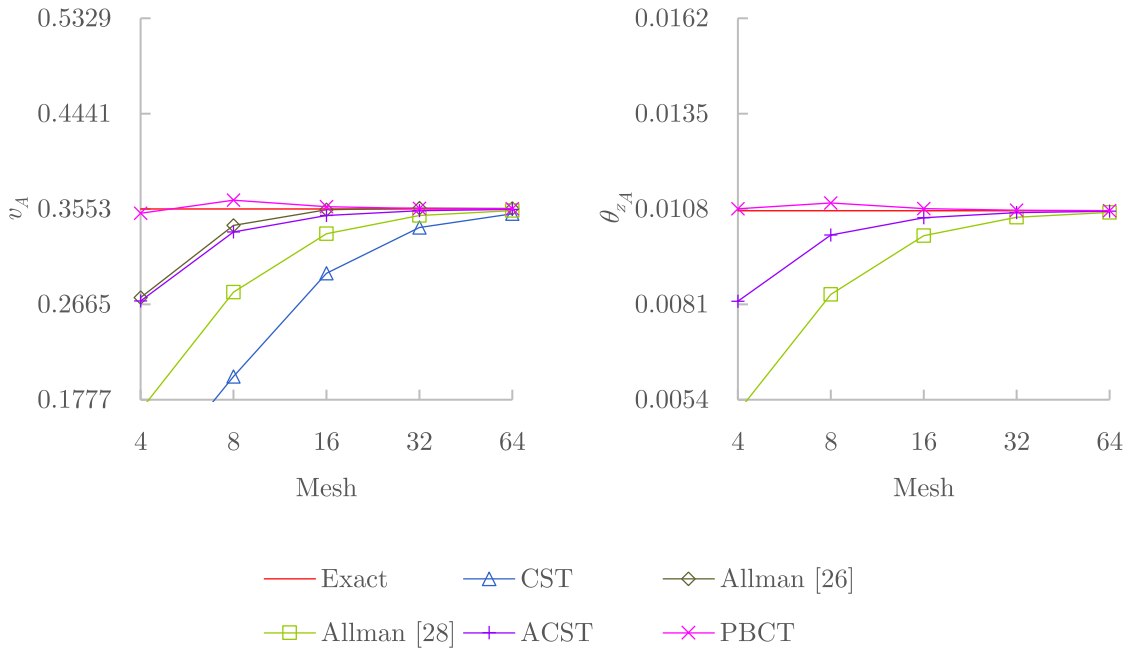

Figure 4.8: Vertical displacement v_A and rotation θ_{z_A} of the Timoshenko cantilever beam on regular meshes

4.6.5 Curved beam

The last beam problem analysed here is a curved cantilever beam loaded at its end by a uniformly distributed shear unit load, as shown in Fig. 4.9. The element properties are $E = 1.0\text{E}{+}07$, $\nu = 0.25$ and $t = 0.1$. This benchmark problem introduced in Ref. [47] is quite demanding for the finite element verification due to the slenderness and the curvature of the beam.

The element presented by Allman in Ref. [26] performs the best on this numerical example, followed by the here presented elements ACST and PBCT, as it can be observed in Tables 4.6 and 4.7 or in Fig. 4.10.

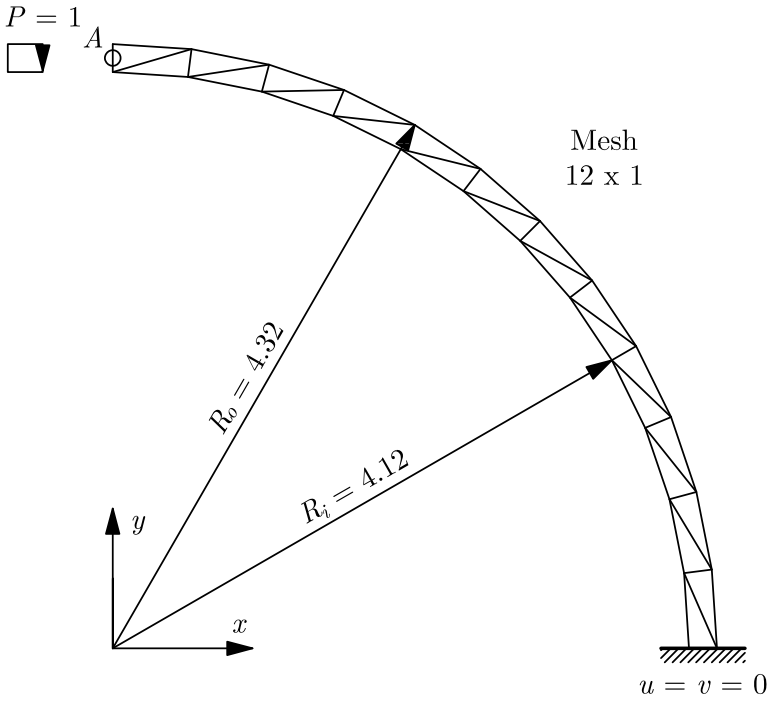

Figure 4.9: A curved beam model

Table 4.6: Vertical displacement v_A of the curved beam

Mesh	CST	Allman [26]	Allman [28]	ACST	PBCT
12 x 1	-0.007133	-0.040752	-0.012706	-0.021351	-0.039555
24 x 2	-0.023031	-0.068474	-0.035547	-0.048226	-0.054816
48 x 4	-0.051747	-0.082470	-0.064444	-0.072760	-0.070653
96 x 8	-0.075168	-0.086929	-0.080941	-0.083892	-0.081984
192 x 16	-0.084767	-0.088130	-0.086503	-0.087316	-0.086646
Ref. [47]			-0.08734		

Table 4.7: Rotation θ_{z_A} of the curved beam

Mesh	Allman [28]	ACST	PBCT
12 x 1	0.003842	0.006403	0.010946
24 x 2	0.010731	0.014528	0.015741
48 x 4	0.019446	0.021946	0.020902
96 x 8	0.024417	0.025306	0.024590
192 x 16	0.026091	0.026337	0.026096
Ref.		-	

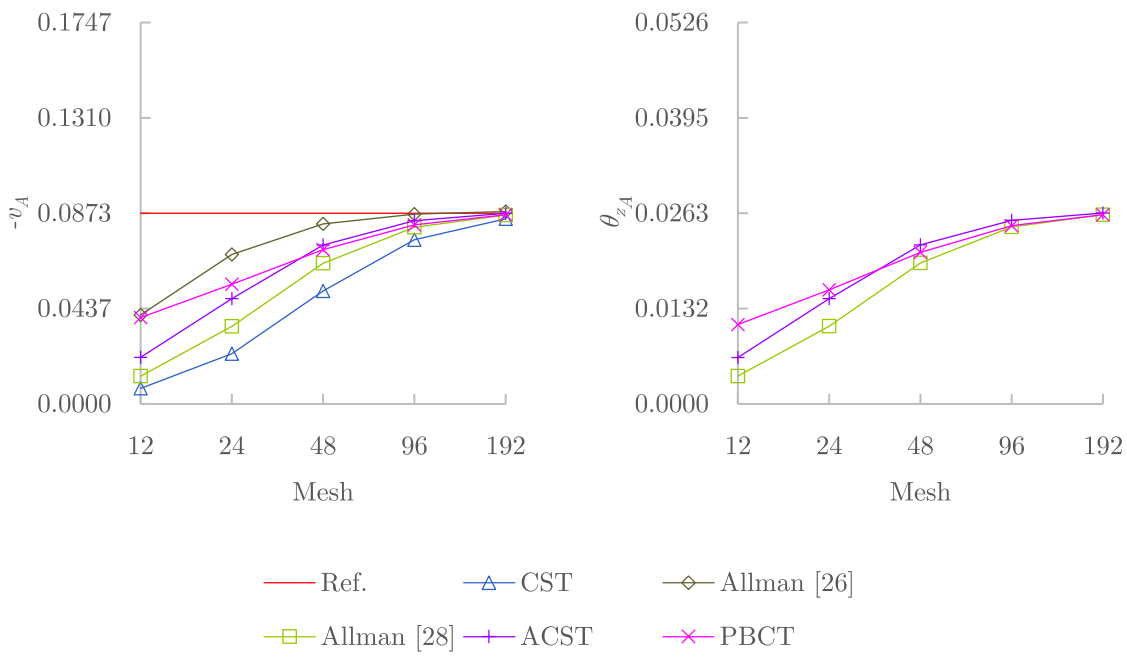

Figure 4.10: Vertical displacement $-v_A$ and rotation θ_{z_A} of the curved beam

4.6.6 Cook's problem

Cook's problem is a standard benchmark problem introduced by Cook in Ref. [48], and it is regularly used for testing new membrane finite elements. It can be described as a deep tapered cantilever beam subjected to a uniformly distributed shear unit load at its end, as shown in Fig. 4.11. The element properties are $E = 1.0$, $\nu = 1/3$ and $t = 1.0$.

Tables 4.8 and 4.8, and Fig. 4.12 show that the element presented by Allman in Ref. [26] is performing the best on this numerical example, and that the ACST element follows its performance closely. The PBCT element, however, does not seem to be particularly efficient on Cook's problem as its performance is slightly better than that of the CST element.

Table 4.8: Vertical displacement v_A of the Cook's problem

Mesh	CST	Allman [26]	Allman [28]	ACST	PBCT
2 x 2	11.993	20.084	16.127	18.651	14.826
4 x 4	18.284	22.708	20.915	21.893	19.538
8 x 8	22.022	23.611	23.007	23.250	22.331
16 x 16	23.412	23.872	23.683	23.734	23.460
32 x 32	23.815	23.941	23.882	23.891	23.816
Ref. [32]			23.96		

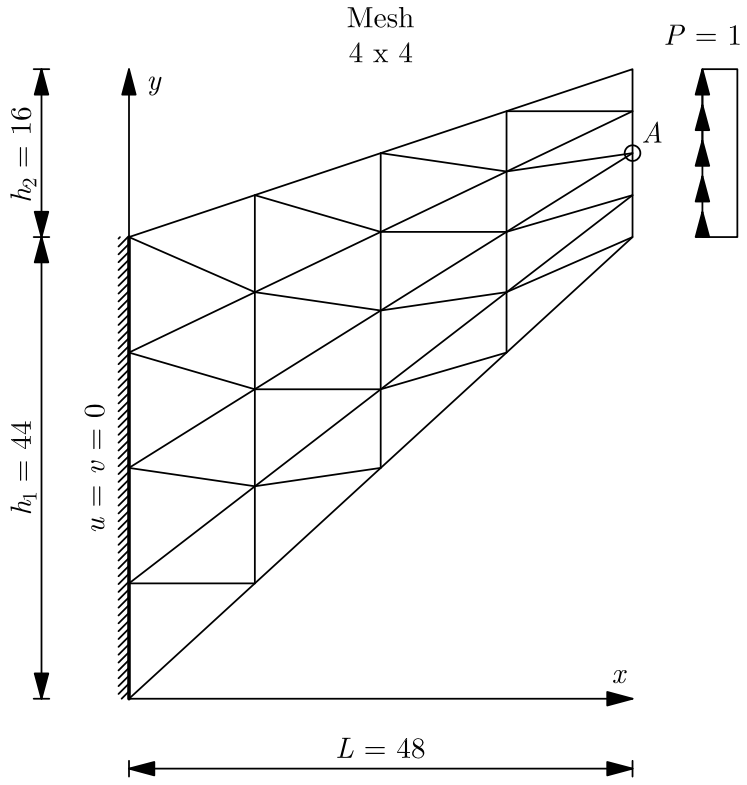

Figure 4.11: Model of Cook's problem

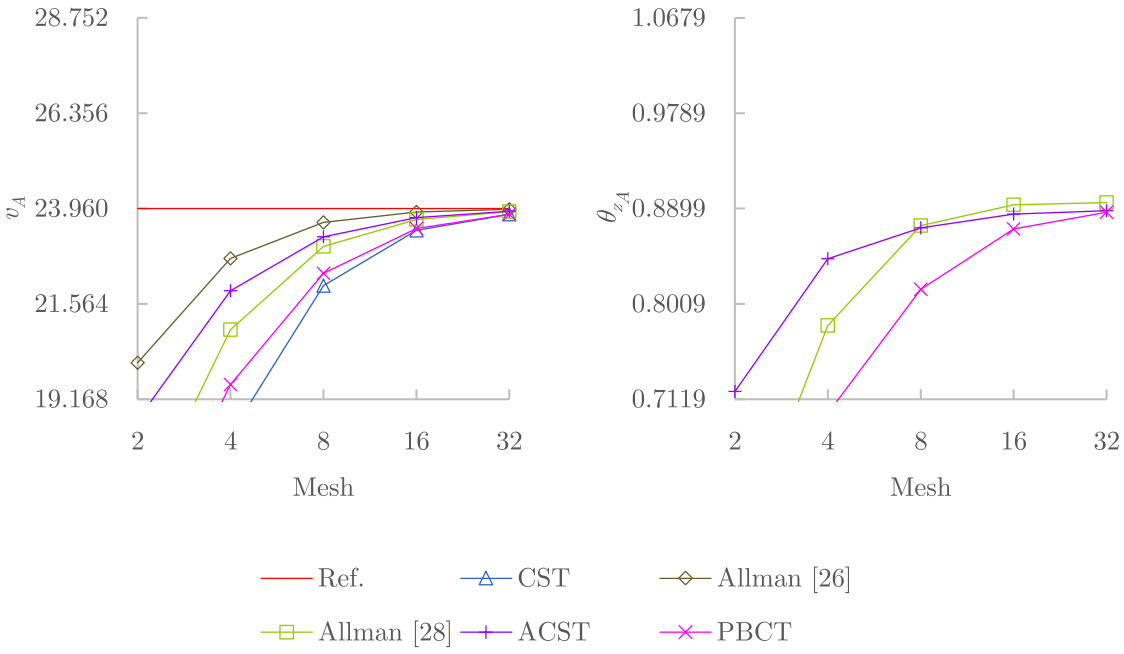

Figure 4.12: Vertical displacement v_A and rotation θ_{z_A} of the Cook's problem

Table 4.9: Rotation θ_{z_A} of the Cook's problem

Mesh	Allman [28]	ACST	PBCT
2 x 2	0.55646	0.71912	0.49434
4 x 4	0.78067	0.84299	0.69877
8 x 8	0.87389	0.87191	0.81456
16 x 16	0.89339	0.88471	0.87082
32 x 32	0.89545	0.88788	0.88646
Ref.		-	

4.7 Conclusions

Two new three-node membrane finite elements with true rotations named ACST and PBCT are presented. The ACST element is developed by assuming strains in the element centroid, while satisfying the classical theory of plane elasticity definition of rotation. These strains are derived from a high performing element presented by Allman in Ref. [26] and modified for better performance. The PBCT element is developed by pursuing an element capable of achieving the exact response for arbitrary pure bending problems. Though such element has not been found, the PBCT element partially fulfils this quest as it is capable of achieving the exact response for pure bending problems in which the principal axes of the problem solution coincide with the x and y axes, regardless of the finite element mesh and the Poisson's ratio.

The ACST element passes the patch test for the constant strain state regardless of the element size, so that the convergence towards a solution can be reliably expected in all cases. That is also the case with the PBCT element, which passes the constant strain patch test only when the size of the elements become infinitesimal, even though the element formulation itself is capable of providing the exact strains regardless of the element size. In addition, the presented elements have a correct rank, i.e., they are free of spurious zero-energy modes, which is something that has not proven to be easily achieved for membrane finite elements with rotational degrees of freedom.

A decent and consistent performance in all the analysed benchmark problems can be observed for the ACST element, with no noticeable weaknesses. It can also be observed that the ACST element has marginally lower performance than the element presented by Allman in Ref. [26]. However, it should be noted that that element has a spurious zero-energy mode and that its rotational degrees of freedom are not true rotations, which is something that contributes to its higher performance, but also limits its application. Moreover, the element presented later by Allman in Ref. [28], which is an upgrade of the element presented in Ref. [26] in terms of the displacement interpolation order (quadratic to cubic), has true rotations at the nodes and is

actually exhibiting lower performance overall (in respect to the ACST element as well). Due to the fact that the strains at the element nodes are for this element obtained the same as for the CST element, Allman regards this element as *the constant strain triangle with added drilling rotations*, rather than an upgraded element presented previously in Ref. [26].

As for the PBCT element, it shows remarkable performance in problems in which the principal axes of the problem solution coincide with the coordinate axes. However, in other cases its performance is not as good which is something that can be best seen in the *Pure bending of a cantilever beam* example (Subsection 4.6.3), which also indicates that the element formulation is, unfortunately, not invariant. This undesirable property makes the element inappropriate for general application, but it may still find its usage in specific problems due to its pure bending capabilities. Such problems may include certain (research) applications conducted by finite element specialists in which the principal axes of the problem solution are *a priori* known and the user would benefit from faster computation since dense finite element meshes would not be required.

With that, the ACST element, though not outstanding in its performance, is very much appropriate for practical application because it: has true rotations as rotational degrees of freedom, has a correct rank, is capable of passing the constant strain patch test regardless of the element size, is computationally inexpensive, has good and consistent performance in all cases. All this makes it a strong candidate for a default membrane finite element inside a finite element analysis software, as it checks all the necessary requirements.

The ACST element is considered later in Chapter 5 to make the in-plane membrane part in a flat shell finite element formulation, whereas the non-invariance problem of the PBCT element is to be investigated in the future.

Chapter 5

Flat shell finite elements

5.1 Introduction

Since shell structures are generally curved in shape, it is only natural to apply appropriate curved shell theories and employ curved shell finite elements in their analyses. To date, many shell theories have been proposed, but they all share difficulties in deriving governing equations and they all turn out to be rather complex. As a consequence, development of curved shell finite elements is no easy feat, and all the requirements such elements should satisfy are quite challenging to fulfil.

Conveniently, flat shell finite elements can adequately represent curved surfaces, provided that the finite element mesh is reasonably dense enough. This physical approximation becomes more and more accurate with the finite element mesh refinement (Fig. 5.1), and with that, it is expected that the convergence to the correct result shall occur. The experience in analysing numerous curved shell problems suggest that that is indeed the case [6].

Triangular flat shell finite elements are particularly convenient as they are geometrically very well suited to model shell structures of arbitrary shape, and unlike quadrilateral elements, they

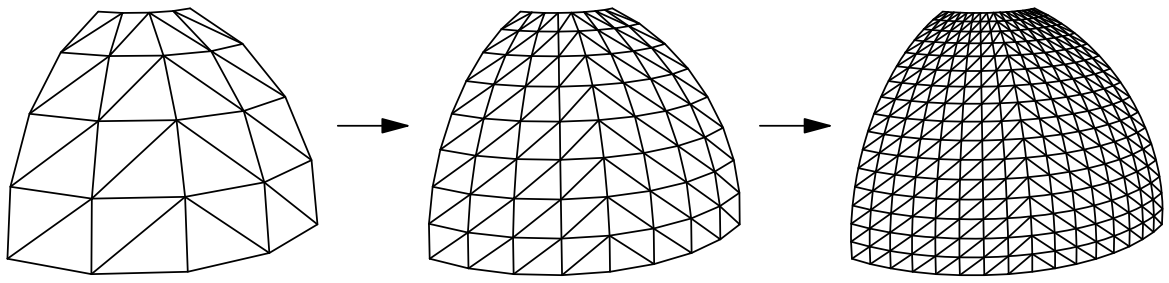

Figure 5.1: Mesh refinement of a hemisphere quadrant with a hole at the pole with triangular flat shell elements

can not be warped, nor suffer from potential warping issues, which makes them a popular choice. With the discretisation of a curved shell surface, straight finite element edges always make up for a flat triangular element, whereas a quadrilateral element may become warped, as shown in Fig. 5.2.

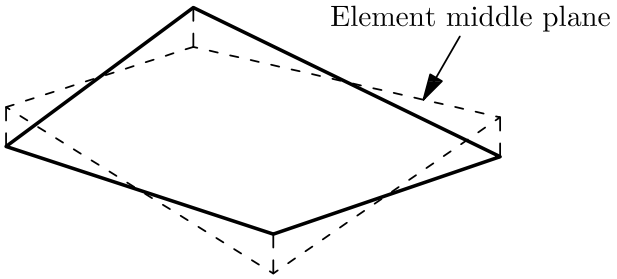

Figure 5.2: Warped quadrilateral element

Flat shell finite element formulation allows for the decoupling of in-plane and out-of-plane effects at the element level, i.e., in-plane membrane part and out-of-plane plate bending part can be taken as two mutually independent parts. Such approach is typical as it offers both simplicity and practicality. Additionally, there is a property of generality in the finite element formulation as no particular shell theory is imposed.

The commonly used three-node flat shell finite element is formed with the CST and the DKT elements making up for the in-plane and the out-of-plane part, respectively. However, such element has two deficiencies. First, it has five degrees of freedom in its local plane due to the absence of the drilling rotations in the CST element formulation, and second, it disregards the out-of-plane shear strains contribution, which follows from the DKT element concept.

The first deficiency results in the singularity of the global stiffness matrix if all the elements meeting at a node are coplanar. This problem is usually fixed by introducing an artificial drilling stiffness that satisfies the element equilibrium in a weak sense. However, this approach generally results in a stiffer response of the model due to the added stiffness that has no physical background. In addition, fully compatible connections at the nodes may not be always achievable. This would depend on the finite element type, position and orientation in space, e.g., the beam element end rotation at the node that corresponds to the missing or artificial drilling rotation of the shell element.

The second deficiency is typically not an issue since many shell structures are usually thin, in which the out-of-plane shear strains are significantly smaller than the bending ones, and mostly negligible. In any case, the fact that the application of such element is limited to thin shell cases

remains.

One of the main objectives of this thesis is to provide a three-node flat shell finite element free of these deficiencies, while being effective and robust so it could be reliably used in all cases. The sixth degree of freedom (the drilling rotation) is provided in a physically correct way by the ACST element, whereas the contribution of the out-of-plane shear strains is recognised by the T3-U3, T3-LSC and T3-LSI elements.

5.2 Stiffness matrix

Since a flat shell finite element can be arbitrarily positioned in space, transformation from the global to the local element system[1] is carried out first, as it would be impractical to form the element stiffness matrix in the global system directly. The flat shell finite element stiffness matrix is then formed by taking the stiffness matrix components of the out-of-plane plate bending and the in-plane membrane parts that are given in Eqs. (3.30) and (4.36) in the local system, and connecting them to the corresponding local unknown nodal degrees of freedom.

Local stiffness matrix for the element node i can be written as

$$\begin{bmatrix} \mathbf{K_m}^e_{\overline{u}_i,\overline{u}_i} & \mathbf{K_m}^e_{\overline{u}_i,\overline{v}_i} & 0 & 0 & 0 & \mathbf{K_m}^e_{\overline{u}_i,\overline{\theta_{z}}_i} \\ \mathbf{K_m}^e_{\overline{v}_i,\overline{u}_i} & \mathbf{K_m}^e_{\overline{v}_i,\overline{v}_i} & 0 & 0 & 0 & \mathbf{K_m}^e_{\overline{v}_i,\overline{\theta_{z}}_i} \\ 0 & 0 & \mathbf{K_p}^e_{\overline{w}_i,\overline{w}_i} & \mathbf{K_p}^e_{\overline{w}_i,\overline{\theta_{x}}_i} & \mathbf{K_p}^e_{\overline{w}_i,\overline{\theta_{y}}_i} & 0 \\ 0 & 0 & \mathbf{K_p}^e_{\overline{\theta_{x}}_i,\overline{w}_i} & \mathbf{K_p}^e_{\overline{\theta_{x}}_i,\overline{\theta_{x}}_i} & \mathbf{K_p}^e_{\overline{\theta_{x}}_i,\overline{\theta_{y}}_i} & 0 \\ 0 & 0 & \mathbf{K_p}^e_{\overline{\theta_{y}}_i,\overline{w}_i} & \mathbf{K_p}^e_{\overline{\theta_{y}}_i,\overline{\theta_{x}}_i} & \mathbf{K_p}^e_{\overline{\theta_{y}}_i,\overline{\theta_{y}}_i} & 0 \\ \mathbf{K_m}^e_{\overline{\theta_{z}}_i,\overline{u}_i} & \mathbf{K_m}^e_{\overline{\theta_{z}}_i,\overline{v}_i} & 0 & 0 & 0 & \mathbf{K_m}^e_{\overline{\theta_{z}}_i,\overline{\theta_{z}}_i} \end{bmatrix}, \tag{5.1}$$

in which the indices represent the corresponding local unknown degrees of freedom. The mutual independence of the in-plane and the out-of-plane effects in the local system can be clearly observed from the local stiffness matrix. Vector of local unknown degrees of freedom for the element node i can be written as

$$\left\{ \overline{u}_i \quad \overline{v}_i \quad \overline{w}_i \quad \overline{\theta_{x}}_i \quad \overline{\theta_{y}}_i \quad \overline{\theta_{z}}_i \right\}^{\mathrm{T}}. \tag{5.2}$$

After the formation of the local stiffness matrix, transformation of the same is carried out back to the global system.

[1] The local element system is defined within the plane of the element.

5.3 Numerical examples

In this section, combinations of the presented plate and membrane finite elements (with the exception of the PBCT element) are analysed on a variety of standard benchmark examples, and the results are compared to the commonly employed CST and DKT combination. Additionally, the CST element is joined with the presented plate elements, and the ACST element is joined with the DKT element. All numerical examples were performed in FEAP.

5.3.1 Spherical shell problem

First numerical example is a doubly-curved shell problem introduced in Ref. [47]. It is a hemisphere with a hole at the pole loaded by four concentrated forces alternating in sign at $\pi/2$ intervals on the equator. The element properties are $E = 6.825\text{E+}07$, $\nu = 0.3$, $k = 5/6$ and $t = 0.04$. Due to the orthogonal symmetry of the problem, only quarter of the hemisphere is analysed, as shown in Fig. 5.3.

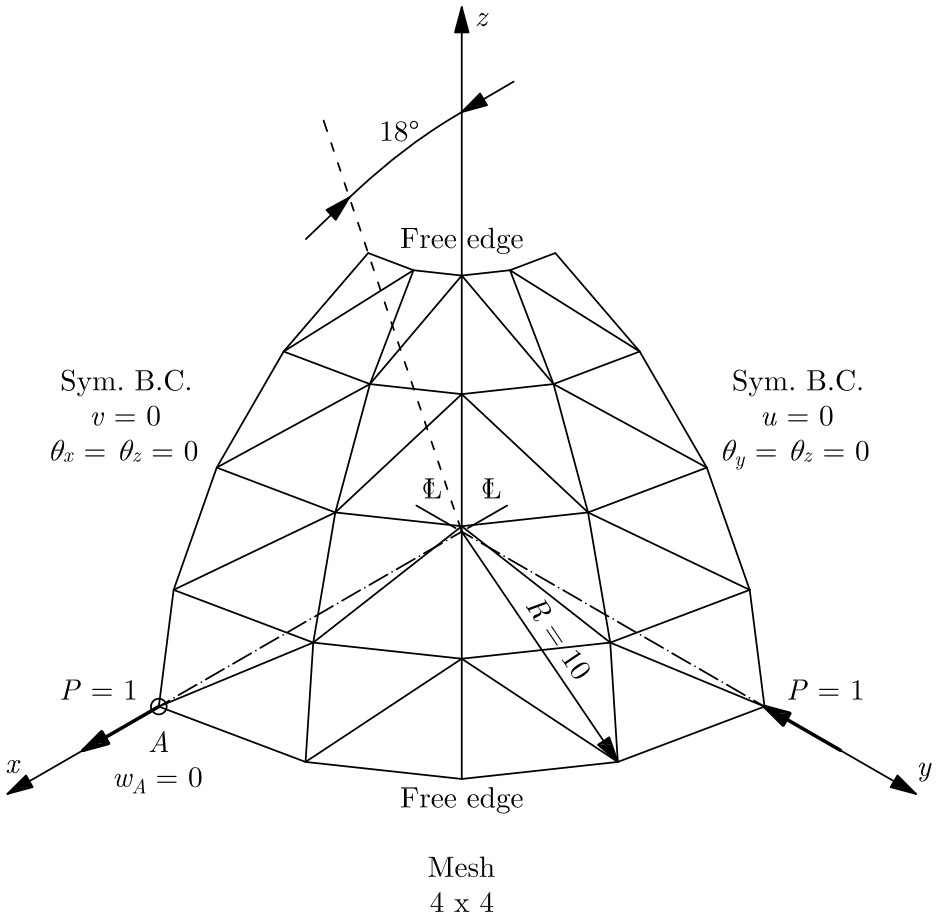

Figure 5.3: Spherical shell problem model

Table 5.1 and Fig. 5.4 indicate locking behaviour when the ACST element forms the membrane part, whereas no locking can be observed when the CST element is employed instead. With the finite element mesh refinement, the locking behaviour fades rapidly. A shell element performs much better when the assumed strain elements T3-LSC and T3-LSI are, instead of the displacement-based T3-U3 element, joined with the CST element. When joined with the ACST element, the difference is not so pronounced due to the locking of the membrane part. In addition, the CST + T3-LSC combination seems to converge to a slightly higher value than the other combinations.

Table 5.1: Horizontal displacement u_A of the spherical shell problem

Mesh	CST + DKT	CST + T3-U3	CST + T3-LSC	CST + T3-LSI
4 x 4	0.092519	0.051187	0.095273	0.096711
8 x 8	0.092699	0.082023	0.095080	0.095029
16 x 16	0.092364	0.090631	0.094338	0.093579
32 x 32	0.092795	0.092602	0.094514	0.093413
64 x 64	0.093263	0.093254	0.094819	0.093586
Mesh	ACST + DKT	ACST + T3-U3	ACST + T3-LSC	ACST + T3-LSI
4 x 4	0.004056	0.002799	0.004040	0.003985
8 x 8	0.027745	0.024197	0.027674	0.027841
16 x 16	0.078898	0.077216	0.078927	0.079538
32 x 32	0.092233	0.092037	0.092356	0.092678
64 x 64	0.093385	0.093367	0.093461	0.093625
Ref. [47]			0.094	

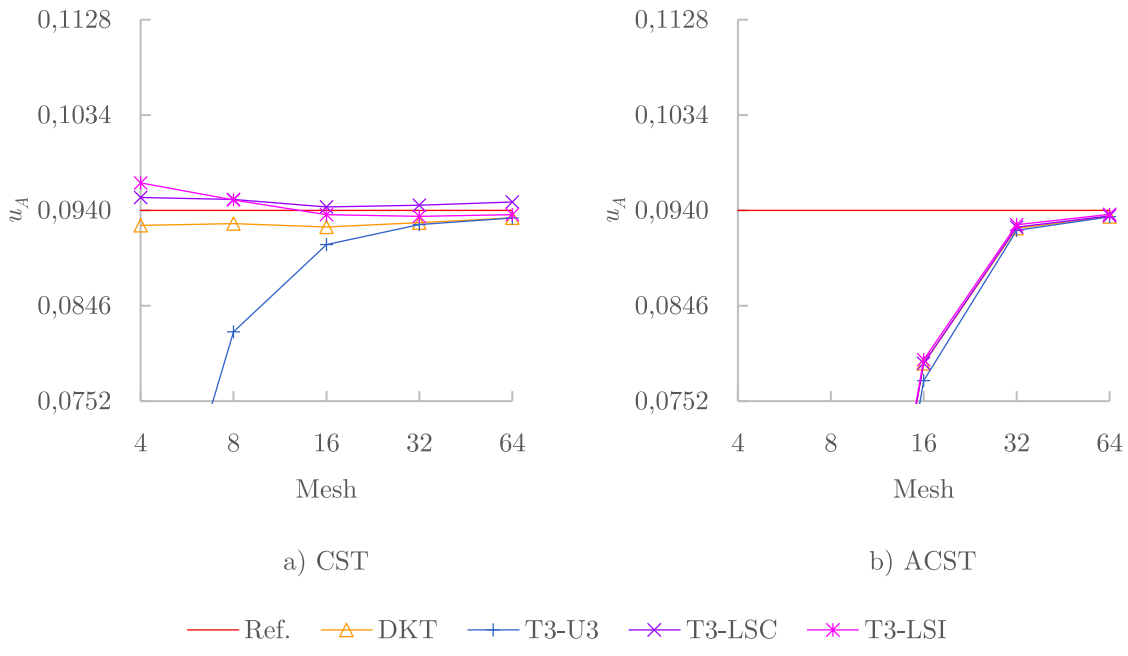

Figure 5.4: Horizontal displacement u_A of the spherical shell problem

5.3.2 Scordelis-Lo roof

Scordelis-Lo roof [49] is a classical benchmark problem analysed next. It is a singly-curved shell shaped as a barrel vault that is supported on rigid diaphragms at its transverse edges. The roof is loaded by its own weight, which translate to the loading intensity 90.0 per unit area in the $-z$ direction. The element properties are $E = 4.32\text{E+}08$, $\nu = 0.0$, $k = 5/6$ and $t = 0.25$. Due to the orthogonal symmetry of the problem, only quarter of the roof is analysed, as shown in Fig. 5.5.

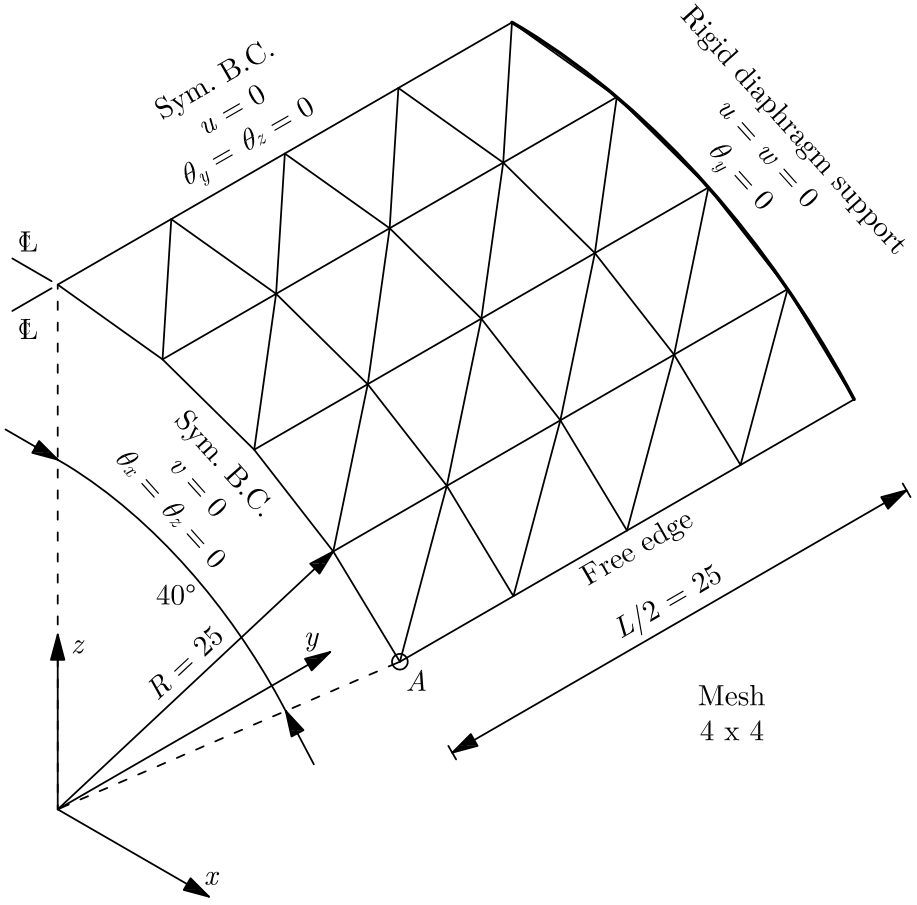

Figure 5.5: Scordelis-Lo roof model

The results shown in Table 5.2 and in Fig. 5.6 point out that the element combinations which include the out-of-plane shear strains contribution diverge from the correct solution with the finite element mesh refinement when the CST element makes up the membrane part. Conversely, with the ACST element making up the membrane part, this is no longer the case. Moreover, higher performance with strong convergence behaviour is observed regardless of the employed plate bending element.

Table 5.2: Vertical displacement w_A of the Scordelis-Lo roof

Mesh	CST + DKT	CST + T3-U3	CST + T3-LSC	CST + T3-LSI
4 x 4	-0.22215	-0.21476	-0.23425	-0.23101
8 x 8	-0.26421	-0.26294	-0.27973	-0.27740
16 x 16	-0.28956	-0.28934	-0.30908	-0.30647
32 x 32	-0.29764	-0.29830	-0.32208	-0.31970
64 x 64	-0.29980	-0.31157	-0.34111	-0.33798
Mesh	ACST + DKT	ACST + T3-U3	ACST + T3-LSC	ACST + T3-LSI
4 x 4	-0.30813	-0.29160	-0.30930	-0.31106
8 x 8	-0.30072	-0.29917	-0.30219	-0.30233
16 x 16	-0.30047	-0.30025	-0.30138	-0.30149
32 x 32	-0.30051	-0.30052	-0.30105	-0.30123
64 x 64	-0.30053	-0.30075	-0.30100	-0.30118
Ref. [47]		-0.3024		

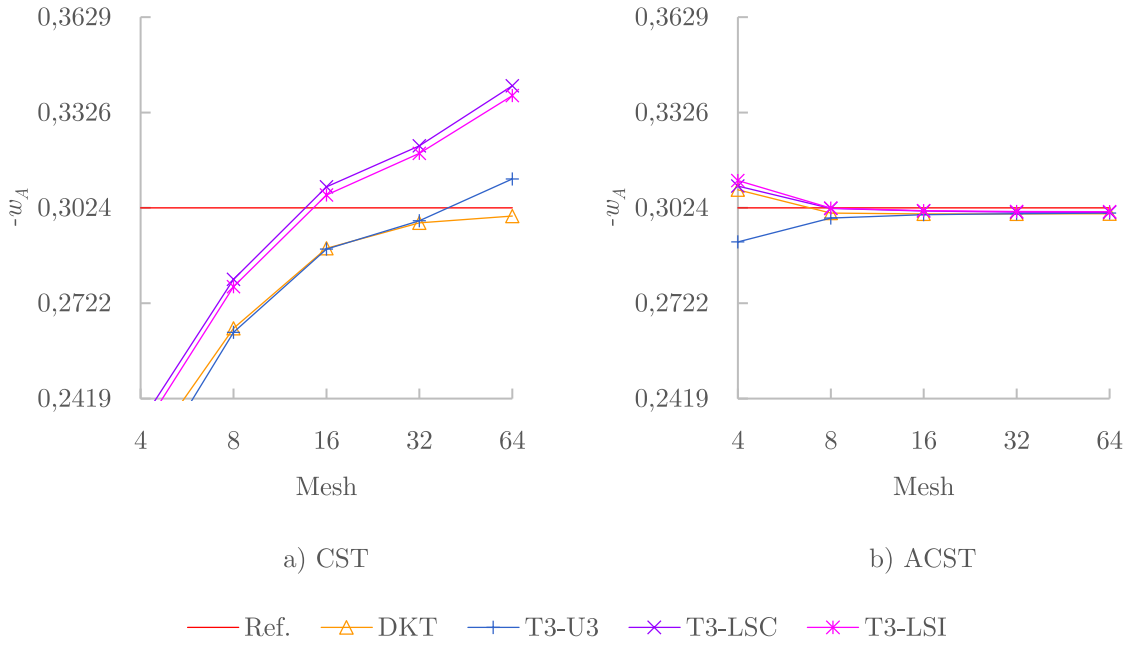

Figure 5.6: Vertical displacement $-w_A$ of the Scordelis-Lo roof

5.3.3 Pinched cylinder

A pinched cylinder with diaphragms at its ends is another frequently analysed shell problem. The cylinder is *pinched* with two opposing unit point loads acting on its mid section. The element properties are $E = 3.0\text{E}{+}06$, $\nu = 0.3$, $k = 5/6$ and $t = 3.0$. As the problem is characterised by a double symmetry, only one octant of the cylinder is analysed, as shown in Fig. 5.7.

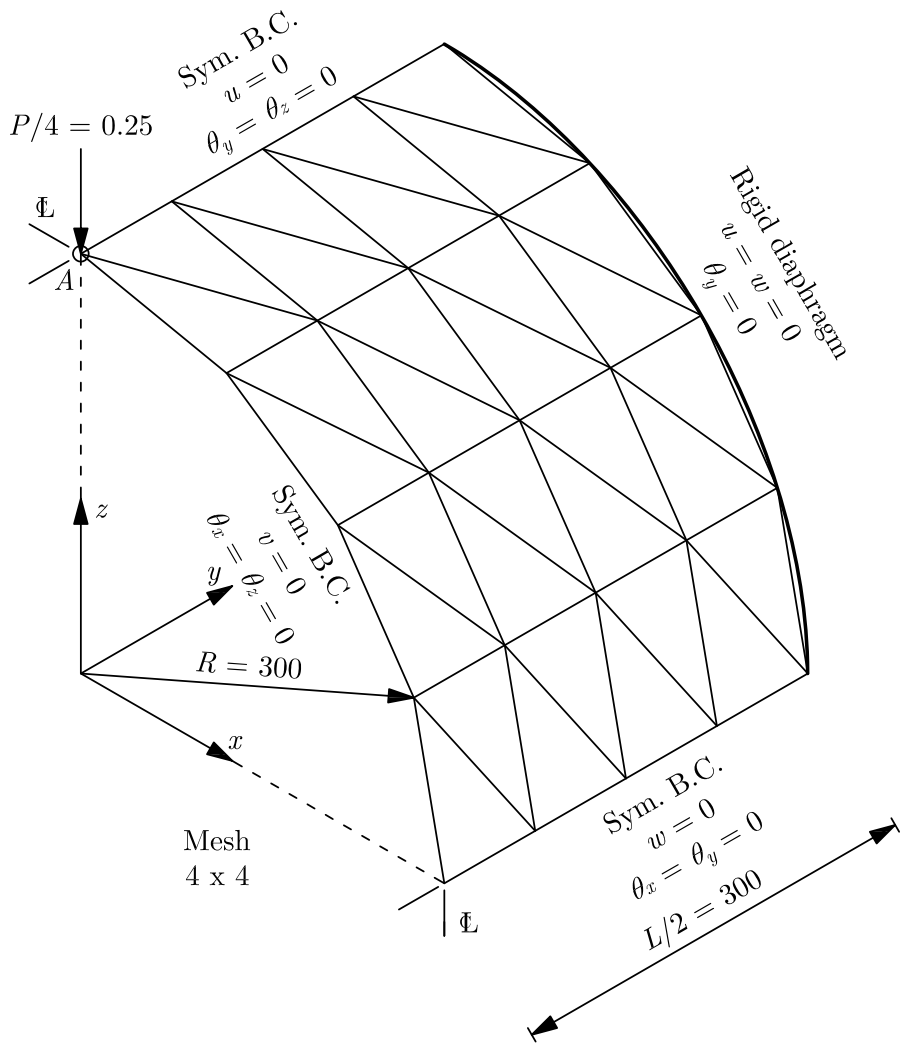

Figure 5.7: Pinched cylinder model

In this numerical example, very little difference can be discerned between the results obtained with either the CST or the ACST element forming the membrane part, and the performance of different element combinations is fairly similar, as shown in Table 5.3 and in Fig. 5.8. However, on very dense meshes[2] (not shown here) the combinations which include the out-of-plane shear strains contribution and the CST element start to diverge from the correct solution.

[2]More than 64 x 64.

Table 5.3: Vertical displacement w_A of the pinched cylinder

Mesh	CST + DKT	CST + T3-U3	CST + T3-LSC	CST + T3-LSI
4 x 4	-8.9853E-06	-5.5166E-06	-7.5855E-06	-8.2486E-06
8 x 8	-1.5751E-05	-1.2911E-05	-1.4356E-05	-1.4928E-05
16 x 16	-1.7776E-05	-1.6814E-05	-1.7210E-05	-1.7452E-05
32 x 32	-1.8174E-05	-1.8050E-05	-1.8082E-05	-1.8213E-05
64 x 64	-1.8259E-05	-1.8419E-05	-1.8401E-05	-1.8543E-05
Mesh	ACST + DKT	ACST + T3-U3	ACST + T3-LSC	ACST + T3-LSI
4 x 4	-1.0268E-05	-5.0144E-06	-8.3661E-06	-9.2006E-06
8 x 8	-1.5777E-05	-1.2733E-05	-1.4307E-05	-1.4971E-05
16 x 16	-1.7785E-05	-1.6819E-05	-1.7176E-05	-1.7439E-05
32 x 32	-1.8188E-05	-1.8059E-05	-1.8052E-05	-1.8148E-05
64 x 64	-1.8263E-05	-1.8353E-05	-1.8310E-05	-1.8366E-05
Ref. [27]	-1.8248E-05			

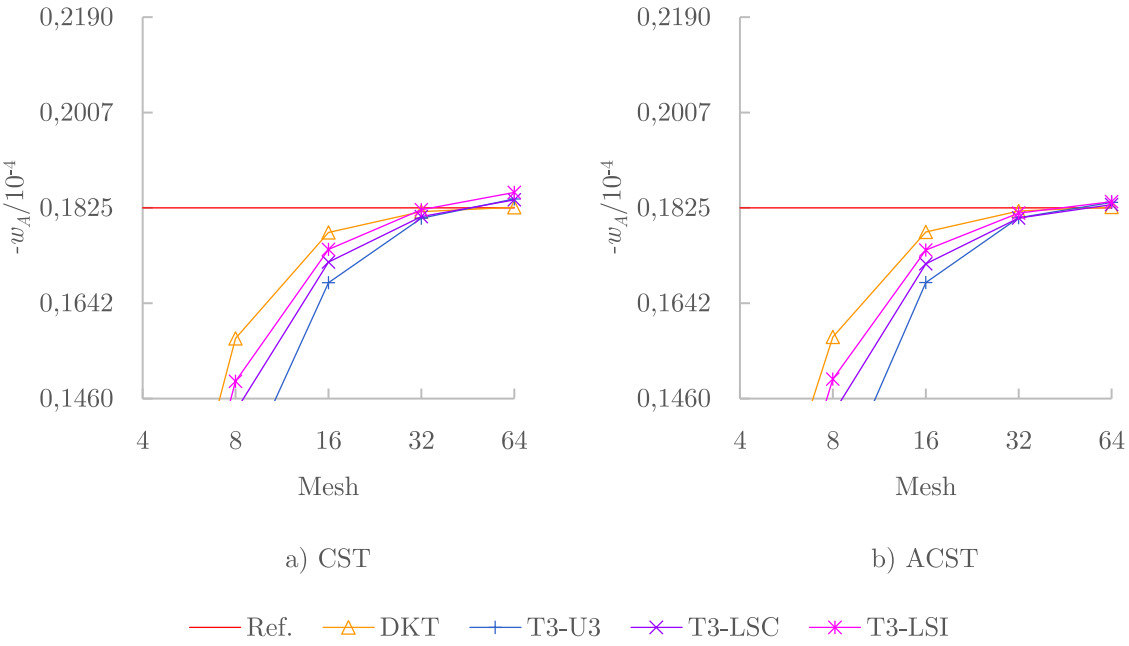

Figure 5.8: Vertical displacement $-w_A/10^{-4}$ of the pinched cylinder

5.3.4 Twisted beam

The next numerical example is a twisted cantilever beam introduced in Ref. [47]. The beam is longitudinally straight with a linearly varying twist angle in the transverse direction with respect to the beam axis that goes from the clamped end to the free end of the beam, making up for the total twist angle of $\pi/2$. Two load cases are considered in this numerical example, both being uniformly distributed shear unit loads at the free end of the beam, where the first one is in the in-plane direction, and the second one is in the out-of-plane direction of the beam model edge, as shown in Fig. 5.9. The element properties are $E = 2.9\text{E}{+}07$, $\nu = 0.22$, $k = 5/6$ and $t = 0.32$.

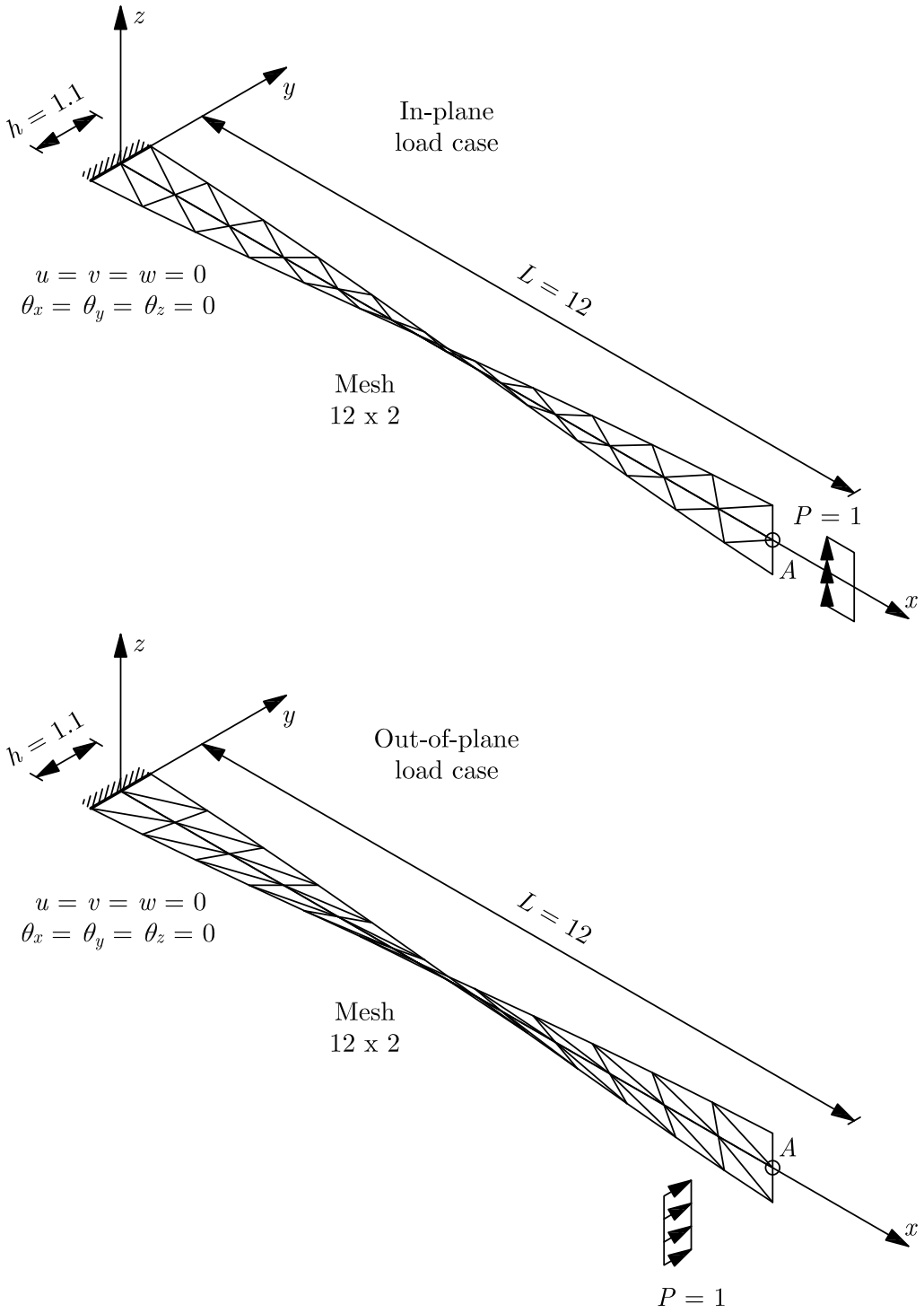

Figure 5.9: Twisted beam models

Similarly to the last two numerical examples, the results shown in Tables 5.4-5.5 and in Figs. 5.10-5.11 also point out that the element combinations which include the out-of-plane shear strains contribution do not converge to the correct solution when joined with the CST element. However, in this numerical example the divergence occurs more rapidly as the model gets more and more refined. Again, with the ACST element forming the membrane part of the shell formulation, convergence to the correct solution is observed for all combinations. In that case, the difference in the performance between these combinations is almost negligible, which indicates the dominance of the membrane part in this problem.

Table 5.4: Vertical displacement w_A of the twisted beam for the in-plane load case

Mesh	CST + DKT	CST + T3-U3	CST + T3-LSC	CST + T3-LSI
6 x 1	0.0053366	0.0053313	0.0056618	0.0060853
12 x 2	0.0053273	0.0053936	0.0058156	0.0063805
24 x 4	0.0053670	0.0060378	0.0066195	0.0073411
48 x 8	0.0053893	0.0098441	0.0105660	0.0113400
96 x 16	0.0053967	0.0249670	0.0258660	0.0263250
Mesh	ACST + DKT	ACST + T3-U3	ACST + T3-LSC	ACST + T3-LSI
6 x 1	0.0047936	0.0047463	0.0047919	0.0047692
12 x 2	0.0053384	0.0053369	0.0053452	0.0053388
24 x 4	0.0053906	0.0053976	0.0053977	0.0053987
48 x 8	0.0053974	0.0054098	0.0054084	0.0054105
96 x 16	0.0053989	0.0054142	0.0054134	0.0054144
Ref. [47]	0.005424			

Table 5.5: Horizontal displacement v_A of the twisted beam for the out-of-plane load case

Mesh	CST + DKT	CST + T3-U3	CST + T3-LSC	CST + T3-LSI
6 x 1	0.0013383	0.0013327	0.0014307	0.0015762
12 x 2	0.0014651	0.0014836	0.0015942	0.0017599
24 x 4	0.0016208	0.0018014	0.0019461	0.0021504
48 x 8	0.0017092	0.0029232	0.0030821	0.0033360
96 x 16	0.0017391	0.0074801	0.0076478	0.0079002
Mesh	ACST + DKT	ACST + T3-U3	ACST + T3-LSC	ACST + T3-LSI
6 x 1	0.0014289	0.0014079	0.0014222	0.0014198
12 x 2	0.0016602	0.0016596	0.0016587	0.0016613
24 x 4	0.0017251	0.0017268	0.0017252	0.0017269
48 x 8	0.0017434	0.0017455	0.0017445	0.0017454
96 x 16	0.0017483	0.0017506	0.0017502	0.0017505
Ref. [47]	0.001754			

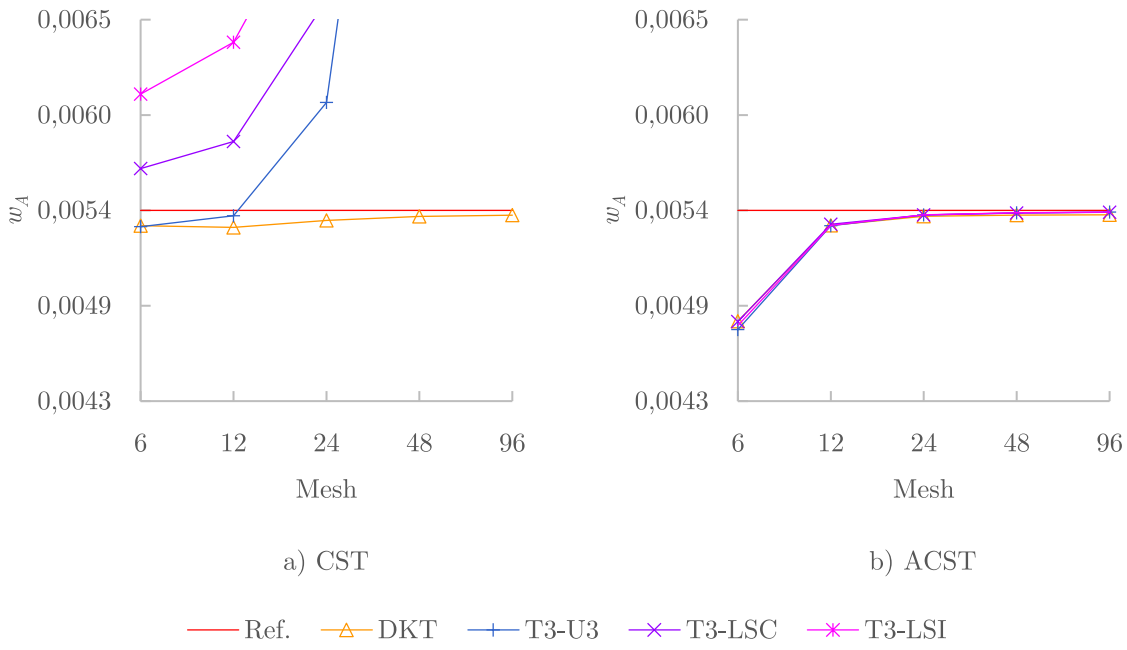

Figure 5.10: Vertical displacement w_A of the twisted beam for the in-plane load case

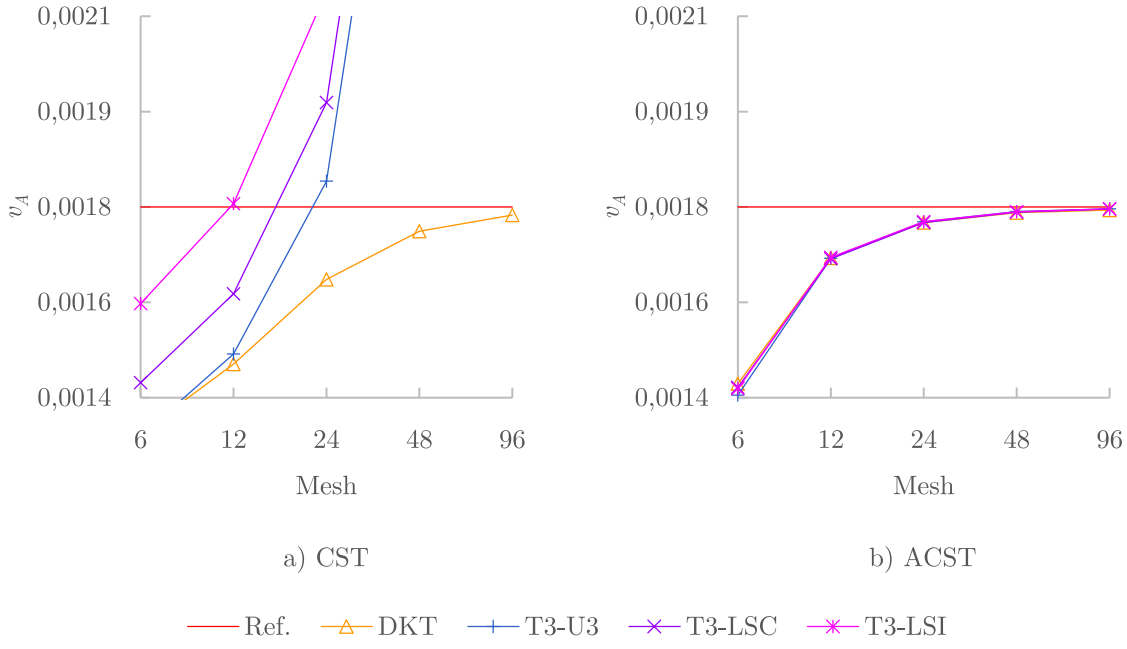

Figure 5.11: Horizontal displacement v_A of the twisted beam for the out-of-plane load case

5.3.5 Raasch challenge

Raasch challenge [50] or Raasch's hook is the last numerical example analysed here, and it is the most recently proposed one. It is a curved cantilever beam whose shape resembles a hook, and it is loaded by an in-plane uniformly distributed shear unit load at its free end, as shown in Fig. 5.12. The element properties are $E = 3300.0$, $\nu = 0.35$, $k = 5/6$ and $t = 2.0$.

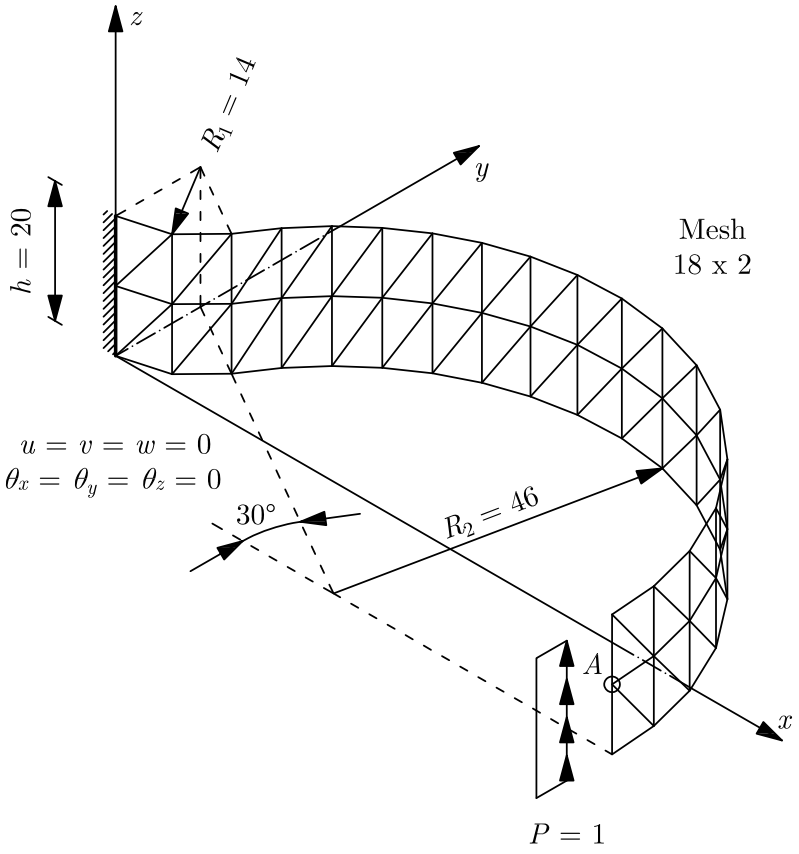

Figure 5.12: Raasch's hook model

Unlike the previous numerical examples, in this one the out-of-plane shear strains are not negligible, as it can be deduced from Table 5.6 and Fig. 5.13. Again, the element combinations which include the out-of-plane shear strains contribution rapidly diverge from the correct solution with the mesh refinement of the model when joined with the CST element. As it is the case with all previous numerical examples, all element combinations that include the ACST element are convergent.

Table 5.6: Vertical displacement w_A of the Raasch's hook

Mesh	CST + DKT	CST + T3-U3	CST + T3-LSC	CST + T3-LSI
9 x 1	4.2448	3.9630	4.4969	4.6830
18 x 2	4.5665	4.5416	4.8125	5.2933
36 x 4	4.6724	4.8218	5.2440	5.8664
72 x 8	4.7024	6.1880	6.9333	7.6586
144 x 16	4.7105	12.954	13.853	14.567
Mesh	ACST + DKT	ACST + T3-U3	ACST + T3-LSC	ACST + T3-LSI
9 x 1	4.2115	3.9377	4.4127	4.3636
18 x 2	4.5642	4.5467	4.6790	4.7224
36 x 4	4.6722	4.7166	4.7893	4.8369
72 x 8	4.7027	4.8369	4.8833	4.9080
144 x 16	4.7106	4.9476	4.9668	4.9746
Ref. [50]		4.9352		

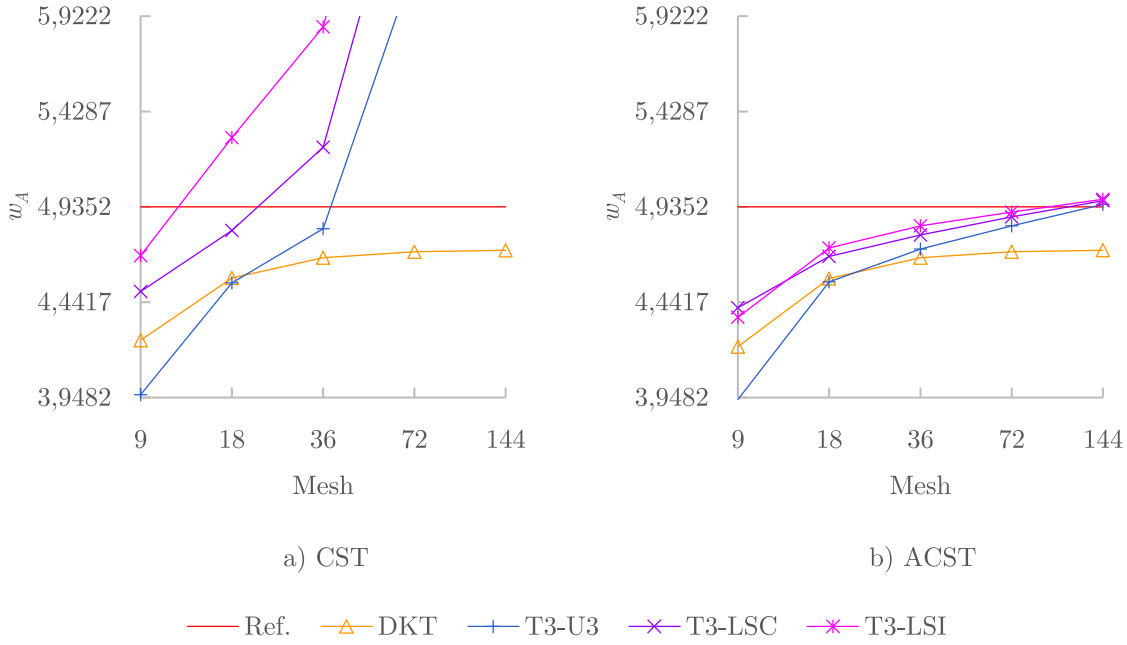

Figure 5.13: Vertical displacement w_A of the Raasch's hook

5.4 Conclusions

Various combinations of the in-plane membrane part and the out-of-plane plate bending part of the shell finite element formulation have been subjected to the benchmark problems. The commonly employed CST + DKT combination, which exhibits good convergence properties and performance overall, is used for comparative purposes with respect to the newly presented ones. Its deficiencies are not actually showing in these problems as the problems themselves do not provoke the same, nor are meant to do so.

The first deficiency, which is linked to the missing (or artificial) drilling degree of freedom, can be fixed by employing the ACST element instead, which has a theoretically correct imple-

mentation of the same. This eliminates the need for the introduction of some artificial stiffness into the element formulation.

As for the second deficiency, a plate bending element which recognises the out-of-plane shear strains contribution is to be used instead of the DKT element. However, in that case, the CST element should not make up the membrane part of the shell finite element formulation any more.

The benchmark problems have shown that such combinations do not converge to the correct solution, and in some problems, the divergence is substantial, as shown in the *Twisted beam* (Subsection 5.3.4) and in the *Raasch challenge* (Subsection 5.3.5). Interestingly, the only exception is the *Spherical shell problem* (Subsection 5.3.1).

Conversely, the combinations that include the presented finite elements converge to the correct solution with the finite element mesh refinement of the model in all tested benchmark problems. The main difference in performance between these combinations is in the plate bending element, as the ACST element is the only proposed element used for the in-plane membrane part of the shell finite element formulation.

Similarly to the results of the plate benchmark problems shown in Section 3.5, the combinations that include the T3-LSI element seem to be the most efficient. However, they are quickly followed by those that include the T3-LSC and the T3-U3 element, respectively.

The only drawback with the combinations that include the presented finite elements is a peculiar locking behaviour that manifests in the *Spherical shell problem* on coarse meshes, and which appears to be linked exclusively with the ACST element. Such locking behaviour in flat shell finite elements with drilling degrees of freedom has been reported before [12]. However, this locking fades quickly with the finite element mesh refinement of the model.

The presented shell combinations with respect to the CST + DKT combination perform similarly and have a comparable computational efficiency. However, the important fact here is that they are free of the deficiencies that encompass the regularly employed CST + DKT combination.

Even though some locking behaviour is observed in the *Spherical shell problem* when the mesh is coarse, the same example has quite significant bending strains with respect to the membrane ones, which is not common to the real life shell structures.

In conclusion, of all the proposed combinations, the ACST + T3-LSI combination stands out as *the best* option, and can be reliably used for the analysis of general shell structures.

Chapter 6

Conclusions

This doctoral thesis consist of three main parts: Mindlin plate finite elements (Chapter 3), Membrane finite elements with rotational degrees of freedom (Chapter 4) and Flat shell finite elements (Chapter 5). Each of these three parts have their dedicated conclusions (Sections 3.6, 4.7 and 5.4), and the reader is encouraged to revisit them for more detail and completeness before continuing here.

In the first part, Mindlin plate finite elements, three new elements T3-U3, T3-LSC and T3-LSI are presented. They are all based on the two-node Timoshenko beam finite element with problem-dependent cubic linked interpolation. This beam element is free of shear locking and is capable of returning the exact results for certain load cases. The T3-U3 element is developed by following a classical finite element displacement-based procedure, whereas the T3-LSC and T3-LSI elements are developed by following the assumed strain method.

The presented Mindlin plate elements pass the patch test for the constant bending state, with the T3-U3 and T3-LSI elements capable of passing it regardless of the finite element size. The criterion of passing the patch test ensures convergence to the correct solution with the finite element mesh refinement, and the analysed plate benchmark problems indicate that that is indeed the case.

However, the displacement based T3-U3 element exhibits shear locking behaviour on certain (very) thin plate examples when the mesh is coarse, while the assumed strain T3-LSC and T3-LSI elements are completely free of it. They are also less demanding than the T3-U3 element from a computational point of view. Additionally, the T3-LSC element does not always yield accurate moments when the plate is (very) thin. Other than that, these elements have no additional deficiencies.

As for the performance, the benchmark problems indicate that the presented elements are effective and comparable to other high performing elements from the literature. The T3-LSI element with its higher performance stands out in particular. Moreover, it has not shown any weaknesses in the benchmark problems. With that, it is very much suitable for the practical application.

In the second part of the thesis, membrane finite elements with rotational degrees of freedom, two new elements ACST and PBCT are presented. These two elements are developed in such a way that the rotational degrees of freedom are the true nodal rotations. This is achieved by having the displacement fields interpolations satisfy the classical theory of plane elasticity definition of rotation, which in turn ensures that the finite element analysis always yields true nodal rotations.

Having the true rotations as the rotational degrees of freedom has some important benefits and advantages, viz. moment loads are permitted, fully compatible connections with other types of finite elements are secured in all cases and a global stiffness matrix singularity is always avoided. For plane elasticity problems, only the first one is relevant, whereas for the general shell problems in which these rotational degrees of freedom are the drilling rotations, all three are very important.

The ACST element is developed by assuming strains in the element centroid, whereas the PBCT element is developed by pursuing an element capable of achieving the exact response for arbitrary pure bending problems. Both elements pass the patch test for the constant strain state, with the ACST element capable of passing it regardless of the finite element size. The analysed benchmark problems show that the presented elements converge to the correct solution, which is expected since they pass the patch test. Additionally, they are free of spurious zero-energy modes.

A decent and consistent performance in all the analysed membrane benchmark problems can be observed for the ACST element, for both displacement and rotation values, and with no noticeable weaknesses. With all the good properties and no deficiencies, the ACST element proves to be perfectly suitable for the practical application.

As for the PBCT element, it exhibits remarkable performance in problems in which the principal axes of the problem solution coincide with the coordinate axes, and if such problems are in the pure bending state, the PBCT element is capable of achieving the exact response, regardless of the finite element mesh and the Poisson's ratio. However, during the numerical investigation,

it was found that the PBCT element is, unfortunately, not invariant. This undesirable property is to be more thoroughly investigated in the future.

In the final part of this thesis, flat shell finite elements, various combinations of the the in-plane membrane part and the out-of-plane plate bending part of the shell finite element formulation have been subjected to the benchmark problems. These combinations include the presented membrane and Mindlin plate finite elements, in addition to the CST element and the DKT element.

The combinations that include the CST element and the presented Mindlin plate elements are dismissed as they diverge from the correct solution with the finite element mesh refinement in most cases. However, all the combinations that include the presented ACST element are convergent in all analysed shell benchmark problems, including the combinations with the presented Mindlin plate elements.

The presented combinations are also free of the deficiencies that encompass the regularly employed CST + DKT combination, viz. the missing (or artificial) drilling degree of freedom and the dismissal of the out-of-plane shear strains contribution. This important fact makes them very much suitable for the practical application.

However, certain locking behaviour emerged in one of the analysed benchmark problems, which is linked to the in-plane membrane part. Notwithstanding, the locking fades away rapidly with the finite element mesh refinement of the model. Future work may include more thorough investigation regarding this issue.

The performance and computational efficiency of the presented finite element combinations is comparable to that of the commonly used CST + DKT combination, with the ACST + T3-LSI combination standing out as *the best* option, since it exhibits slightly higher performance. Additionally, these two elements individually have not shown any weaknesses in their respective problems.

To conclude, the ACST + T3-LSI combination that forms the three-node flat shell finite element formulation is proposed for the analysis of general shell structures. It drilling rotations are true rotations and it recognises the out-of-plane shear strains contribution. Additionally, it has shown good convergence properties and efficiency. Ultimately, it is highly suitable for the practical application.

With that, the main objective of this thesis has been fulfilled. New and effective three-node flat shell finite element for the analysis of general 3D shell structures has been presented and

validated for the practical application. This has also been done for (very thin to thick) plate bending problems and plane elasticity (membrane) problems individually, as the contributions of these two mutually independent parts form the out-of-plane and the in-plane part of the flat shell finite element formulation. The concept of decoupling these two parts at the element level has been reconfirmed as a valid procedure, as convergence to the correct solution with the finite element mesh refinement of the curved shell surfaces is observed for the proposed flat shell finite element in all tested benchmark problems.

The linked interpolation approach and the assumed strain method that are utilised here in the development of the new finite elements are still proving to be effective methods. It has been shown that even though these methods are not very recent, possibilities for the development of original and high performing finite elements still remain. Additionally, the inclusion of true rotations as the drilling degrees of freedom in the membrane finite element formulation has yet again shown its advantages, but more importantly, in the case of flat shell finite elements which recognise the shear strains contribution, it has proven to be essential for the convergence to the correct solution.

Bibliography

[1] T. J. R. Hughes, T. E. Tezduyar, Finite Elements Based Upon Mindlin Plate Theory With Particular Reference to the Four-Node Bilinear Isoparametric Element, Journal of Applied Mechanics (3) 587–596. doi:10.1115/1.3157679.

[2] R. H. Macneal, Derivation of element stiffness matrices by assumed strain distributions, Nuclear Engineering and Design (1) 3–12. doi:10.1016/0029-5493(82)90262-X.

[3] X. Zhongnian, A simple and efficient triangular finite element for plate bending, Acta Mechanica Sinica (2) 185–192. doi:10.1007/BF02485859.

[4] O. C. Zienkiewicz, Z. Xu, L. F. Zeng, A. Samuelsson, N.-E. Wiberg, Linked interpolation for Reissner-Mindlin plate elements: Part I—A simple quadrilateral, International Journal for Numerical Methods in Engineering (18) 3043–3056. doi:10.1002/nme.1620361802.

[5] R. L. Taylor, F. Auricchio, Linked interpolation for Reissner-Mindlin plate elements: Part II—A simple triangle, International Journal for Numerical Methods in Engineering (18) 3057–3066. doi:10.1002/nme.1620361803.

[6] O. C. Zienkiewicz, R. L. Taylor, J. Z. Zhu, The Finite Element Method: Its Basis and Fundamentals, 7th Edition, Elsevier, 2013.

[7] K. J. Bathe, Finite Element Procedures, 2nd Edition, Klaus-Jürgen Bathe, Watertown, MA, USA, 2014.

[8] T. J. R. Hughes, The Finite Element Method: Linear Static and Dynamic Finite Element Analysis, Dover Publications, Mineola, NY, USA, 2000.

[9] J. N. Reddy, Theory and Analysis of Elastic Plates and Shells, 2nd Edition, CRC Press, Boca Raton, FL, USA, 2006.

[10] S. Timoshenko, J. N. Goodier, Theory of elasticity, 2nd Edition, McGraw-Hill Book Company, Inc., New York, NY, USA, 1951.

[11] E. Oñate, Structural Analysis with the Finite Element Method. Linear Statics. Volume 1. Basis and Solids, Springer, 2009.

[12] E. Oñate, Structural Analysis with the Finite Element Method. Linear Statics. Volume 2. Beams, Plates and Shells, Springer, 2013.

[13] R. Szilard, Theories and Applications of Plate Analysis: Classical, Numerical and Engineering Methods, John Wiley and Sons, Inc., Hoboken, NJ, USA, 2004.

[14] S. Cen, Y. Shang, Developments of Mindlin-Reissner Plate Elements, Mathematical Problems in Engineering 1–12doi:10.1155/2015/456740.

[15] O. C. Zienkiewicz, R. L. Taylor, J. M. Too, Reduced integration technique in general analysis of plates and shells, International Journal for Numerical Methods in Engineering 3 (2) (1971) 275–290. doi:10.1002/nme.1620030211.

[16] J.-L. Batoz, K.-J. Bathe, L.-W. Ho, A study of three-node triangular plate bending elements, International Journal for Numerical Methods in Engineering (12) 1771–1812. doi:10.1002/nme.1620151205.

[17] K.-U. Bletzinger, M. Bischoff, E. Ramm, A unified approach for shear-locking-free triangular and rectangular shell finite elements, Computers and Structures (3) 321–334. doi:10.1016/S0045-7949(99)00140-6.

[18] D. Ribarić, G. Jelenić, Higher-order linked interpolation in quadrilateral thick plate finite elements, Finite Elements in Analysis and Design (2012). doi:10.1016/j.finel.2011.10.003.

[19] D. Ribarić, G. Jelenić, Higher-order linked interpolation in triangular thick plate finite elements, Engineering Computations (1) 69–109. doi:10.1108/EC-03-2012-0056.

[20] F. Auricchio, R. Taylor, A triangular thick plate finite element with an exact thin limit, Finite Elements in Analysis and Design (1-2) 57–68. doi:10.1016/0168-874X(94)00057-M.

[21] A. K. Soh, Z. F. Long, S. Cen, A new nine DOF triangular element for analysis of thick and thin plates, Computational Mechanics (5) 408–417. doi:10.1007/s004660050461.

[22] C. Wanji, Y. K. Cheung, Refined 9-Dof triangular Mindlin plate elements, International Journal for Numerical Methods in Engineering (11) 1259–1281. doi:10.1002/nme.196.

[23] J.-B. Huang, S. Cen, Y. Shang, C.-F. Li, A New Triangular Hybrid Displacement Function Element for Static and Free Vibration Analyses of Mindlin-Reissner Plate, Latin American Journal of Solids and Structures (5) 765–804. doi:10.1590/1679-78253036.

[24] M. J. Turner, R. W. Clough, H. C. Martin, L. J. Topp, Stiffness and Deflection Analysis of Complex Structures, Journal of the Aeronautical Sciences (9) 805–823. doi:10.2514/8.3664.

[25] P. Bergan, C. Felippa, A triangular membrane element with rotational degrees of freedom, Computer Methods in Applied Mechanics and Engineering (1) 25–69. doi:10.1016/0045-7825(85)90113-6.

[26] D. J. Allman, A compatible triangular element including vertex rotations for plane elasticity analysis, Computers and Structures 19 (1-2) (1984) 1–8. doi:10.1016/0045-7949(84)90197-4.

[27] N. Carpenter, H. Stolarski, T. Belytschko, A flat triangular shell element with improved membrane interpolation, Communications in Applied Numerical Methods (4) 161–168. doi:10.1002/cnm.1630010405.

[28] D. J. Allman, Evaluation of the constant strain triangle with drilling rotations, International Journal for Numerical Methods in Engineering (1988). doi:10.1002/nme.1620261205.

[29] D. Boutagouga, A Review on Membrane Finite Elements with Drilling Degree of Freedom, Archives of Computational Methods in Engineering (4) 3049–3065. doi:10.1007/s11831-020-09489-z.

[30] E. Wilson, R. Taylor, W. Doherty, J. Ghaboussi, Incompatible Displacement Models, in: Numerical and Computer Methods in Structural Mechanics, Elsevier, pp. 43–57. doi:10.1016/B978-0-12-253250-4.50008-7.

[31] A. Sabir, Strain-based finite elements for the analysis of cylinders with holes and normally intersecting cylinders, Nuclear Engineering and Design (2) 111–120. doi:10.1016/0029-5493(83)90128-0.

[32] L. Yuqiu, X. Yin, Generalized conforming triangular membrane element with vertex rigid rotational freedoms, Finite Elements in Analysis and Design (4) 259–271. doi:10.1016/0168-874X(94)90002-7.

[33] S. Cen, M.-J. Zhou, X.-R. Fu, A 4-node hybrid stress-function (HS-F) plane element with drilling degrees of freedom less sensitive to severe mesh distortions, Computers and Structures (5-6) 517–528. doi:10.1016/j.compstruc.2010.12.010.

[34] A. Ibrahimbegovic, R. L. Taylor, E. L. Wilson, A robust quadrilateral membrane finite element with drilling degrees of freedom, International Journal for Numerical Methods in Engineering (3) 445–457. doi:10.1002/nme.1620300305.

[35] C. A. Felippa, A study of optimal membrane triangles with drilling freedoms, Computer Methods in Applied Mechanics and Engineering (16-18) 2125–2168. doi:10.1016/S0045-7825(03)00253-6.

[36] M. Huang, Z. Zhao, C. Shen, An effective planar triangular element with drilling rotation, Finite Elements in Analysis and Design (11) 1031–1036. doi:10.1016/j.finel.2010.07.019.

[37] Y. Shang, S. Cen, Z.-H. Qian, C. Li, High-performance unsymmetric 3-node triangular membrane element with drilling DOFs can correctly undertake in-plane moments, Engineering Computations (7) 2543–2556. doi:10.1108/EC-04-2018-0200.

[38] D. Ribaric, Problem-dependent cubic linked interpolation for Mindlin plate four-node quadrilateral finite elements, Structural Engineering and Mechanics (6) 1071–1094. doi:10.12989/sem.2016.59.6.1071.

[39] E. Papa Dukić, G. Jelenić, Exact solution of 3D Timoshenko beam problem: problem-dependent formulation, Archive of Applied Mechanics (3) 375–384. doi:10.1007/s00419-013-0805-y.

[40] A.-K. Soh, S. Cen, Y.-Q. Long, Z.-F. Long, A new twelve DOF quadrilateral element for analysis of thick and thin plates, European Journal of Mechanics - A/Solids (2) 299–326. doi:10.1016/S0997-7538(00)01129-3.

[41] C. Wanji, Y. K. Cheung, Refined quadrilateral element based on Mindlin/Reissner plate theory, International Journal for Numerical Methods in Engineering (1-3) 605–627. doi:10.1002/(SICI)1097-0207(20000110/30)47:1/3<605::AID-NME785>3.0.CO;2-E.

[42] S. Cen, Y. Shang, C.-F. Li, H.-G. Li, Hybrid displacement function element method: a simple hybrid-Trefftz stress element method for analysis of Mindlin-Reissner plate, International Journal for Numerical Methods in Engineering (3) 203–234. doi:10.1002/nme.4632.

[43] R. L. Taylor, Finite Element Analysis Program (FEAP).

[44] W. Chen, J. Wang, J. Zhao, Functions for patch test in finite element analysis of the Mindlin plate and the thin cylindrical shell, Science in China Series G: Physics, Mechanics and Astronomy (5) 762–767. doi:10.1007/s11433-009-0097-y.

[45] A. Razzaque, Program for triangular bending elements with derivative smoothing, International Journal for Numerical Methods in Engineering (1973). doi:10.1002/nme.1620060305.

[46] L. S. D. Morley, Skew Plates and Structures, The Macmillan Company, New York, NY, USA, 1963.

[47] R. H. Macneal, R. L. Harder, A proposed standard set of problems to test finite element accuracy, Finite Elements in Analysis and Design (1) 3–20. doi:10.1016/0168-874X(85)90003-4.

[48] R. D. Cook, Improved Two-Dimensional Finite Element, Journal of the Structural Division (9) 1851–1863. doi:10.1061/JSDEAG.0003877.

[49] A. C. Scordelis, K. S. Lo, Computer Analysis of Cylindrical Shells, ACI Journal Proceedings (5) 539–562. doi:10.14359/7796.

[50] N. F. Knight, Raasch challenge for shell elements, AIAA Journal (2) 375–381. doi:10.2514/3.13513.

List of Figures

List of Tables